FACULTY OF TECHNOLOGY

Formation of V-bearing iron oxide in the Mustavaara deposit, northern Finland: evidence from in-situ trace elements and Sr isotope composition of plagioclase

Brandon Datar

Supervisor(s): Tuomo Karinen, Shenghong Yang, Marko Moilanen

Master's Programme in Geosciences
Master’s thesis
May 2020

ABSTRACT

FOR THESIS University of Oulu Faculty of Technology

Degree Programme (Bachelor's Thesis, Master's Thesis)	Major Subject (Licentiate Thesis)
Master's Programme in Geosciences	
Author	**Thesis Supervisor**
Datar, Brandon	Karinen, T. (Senior Scientist at GTK), Yang, S.H. (Professor), Moilanen, M. (Doctoral student)

Title of Thesis

Formation of V-bearing iron oxide in the Mustavaara deposit, northern Finland: evidence from in-situ trace elements and Sr isotope composition of plagioclase

Major Subject	Type of Thesis	Submission Date	Number of Pages
Geosciences	Master's Thesis	May 2020	57 p., 3 App

Abstract

Finland has been a historically significant producer of vanadium. The Mustavaara Fe-Ti-V deposit in Lapland had a decade-long history of mining from 1976 to 1985. The deposit is hosted in magnetite gabbro within the upper zone of the Koillismaa layered intrusion. The deposit is divided into four ore layers (Disseminated, Upper, Middle, and Lower ore layers). Each ore layer differs in modal abundance of oxide grains, as well as in V-content of oxides. The highest oxide abundances are found in the Lower ore layer, at 20-35 wt. % ilmenomagnetite, while the highest V contents of ilmenomagnetite are found in the Upper and Lower ore layers, at 1.7 wt. % V_2O_3.

In this study, the systematic analysis of plagioclase grains was conducted from the footwall, to the magnetite gabbro, to the hanging wall units using an in-situ approach via LA-MC-ICP-MS. The samples from the studied rock units display constant initial $^{87}Sr/^{86}Sr$ (2.44 Ga) of about 0.7030. The initial $^{87}Sr/^{86}Sr$ ratio is similar to the coeval siliceous high-magnesium basalt (SHMB) series mafic dykes in the Fennoscandian shield, as well as to some other co-genetic mineralized intrusions in the Tornio-Näränkävaara belt. This indicates that the parental magma of Mustavaara belongs to the SHMB series magma, and that this type of magma is capable of producing an Fe-Ti-V deposit, in addition to known Cr and PGE mineralization.

In-situ trace element concentrations of plagioclase have been analyzed using LA-HR-ICP-MS, to constrain the magma evolution history and ore-formation mechanisms of the iron oxide deposit. A previous study found that the anorthite content decreases from the footwall of the magnetite gabbro unit upwards, and from the hanging wall downward, and suggested that the magnetite gabbro unit may represent the most involved magma. From this study, the highly incompatible elements (e.g., LREE) in plagioclase show a mirror trend with the anorthite content, confirming the double fractionation trend revealed by major elements. In addition, this study confirms that the Upper ore layer (UOL) may represent the most evolved portion of the magma. V and Ti show a similar distribution pattern to anorthite, reaching their lowest concentrations at the UOL, indicating that their bulk partition coefficients are greater than 1. Additionally, traverse analyses of plagioclase from rim to core to rim have been conducted. The results show that highly incompatible element concentrations increase from core to rim, whereas Ti and V concentrations decrease from core to rim. Based on these observations, together with the euhedral texture of magnetite in oxide-poor samples, it is suggested that magnetite and plagioclase and clinopyroxene may have co-precipitated from magma. Some enrichment of oxide due to gravity settling may have formed the magnetite gabbro unit in Mustavaara.

Additional Information

Table of Contents

1.0 Introduction

Vanadium is an economically important metal, in high demand from the steel industry. The most important ore mineral of V is magnetite, mined from the upper part of mafic layered intrusions. The origin of V-bearing magnetite in mafic layered intrusions has been extensively studied. However, the ore formation processes remain controversial.

The Mustavaara Fe-Ti-V deposit is a historically significant deposit located in southeastern Lapland, in northern Finland. The deposit was mined from 1976 to 1985, extracting 13.45 Mt of ore over its operational history (Karinen et al., 2015). The deposit was mined as an open pit. The host rock is a magnetite gabbro located within the larger Porttivaara block, named for a local hill (Juopperi, 1977), within the larger Koillismaa intrusion.

The trace element content and strontium isotope composition of plagioclase grains are analyzed. There are two goals of this process: to determine whether the Mustavaara deposit occurs within a closed (single-pulse), or open (multiple-pulse) magmatic system, and to test the hypothesis by Karinen (2010) that the magnetite gabbro host of the deposit can be considered a sandwich horizon, using strontium isotope and trace element data, respectively. The measurements are taken from various depths along a single borehole from the deposit. At certain depths, trace elements are taken along spot traverses through various grains to measure variations between the rims and cores of these grains. All data is also compared with depth.

1.1 Layered intrusions, distribution, processes, and mineralizations

Layered intrusions are an important igneous bodies, which are formed in large mafic-ultramafic magma chambers. Among igneous rocks, layering is particularly common in gabbroic intrusive bodies, as well as syenitic intrusive bodies; layering is commonly observed in mafic intrusions (Naslund & McBirney, 1996). It has been claimed that layered intrusions“are the repositories of crystals fractionated from magma.” (Scoates & Wall, 2015). As such, these intrusions are of particular importance in the present understanding of the evolution of mafic magmas, as noted by Scoates & Wall (2015). Layered intrusions are also economically significant as hosts of Cr, platinum group element (PGE), and V deposits (Cawthorn et al., 2005). Layered intrusions have a global distribution, occurring on every continent.

The layering of intrusions often occurs in the form of changes in mineralogy or mode of minerals, mineral chemistry, or grain size. The layering is believed to form from a crystal mush

that crystallizes and differentiates, with the crystallization occurring inwards towards the still-molten center of the magma chamber (Naslund & McBirney, 1996). It has been noted that "no single process can explain all types of igneous layering." (Naslund & McBirney, 1996). As such, it can be inferred that there may be multiple processes that can result in the formation of layered intrusions. The most important igneous processes include gravity settling, compaction, magma replenishment and magmatic deformation.

Layered intrusions are composed of cumulate rocks, and formed primarily during the Archean and Proterozoic eons, as noted by Scoates & Wall (2015). Cumulate rocks, or cumulates, are "igneous rocks characterized by a cumulus framework of touching mineral crystals or grains that were evidently formed and concentrated primarily through fractional crystallization." (Irvine, 1982). It is proposed by Irvine (1982) that cumulate rocks may have formed due to crystal settling in some, but not necessarily all, examples. The basic components of cumulates include cumulus crystals and postcumulus material (including intercumulus crystals), and the postcumulus material is suggested by Irvine (1982) to have crystallized from trapped interstitial liquid in the cumulus framework.

There are several well-known layered intrusions worldwide. These include the Skaergaard intrusion in Greenland, the Bushveld Igneous Complex in South Africa, the Great Dyke in Zimbabwe, the Panzhihua intrusion in China, the Muskox and Kiglapait intrusions in Canada, the Stillwater and Duluth complexes in the USA, the Jimberlana intrusion in Australia, and the intrusions of the Tornio-Näränkävaara belt in Fennoscandia.

Layered intrusions undergo fractional crystallization, with more mafic composition occurring with increasing depth, and more evolved, iron-rich composition occurring towards the top of the intrusive body (Cawthorn et al., 2005). This is because ultramafic minerals crystallize first, as shown in Bowen's reaction series. Furthermore, Irvine (1982) notes that denser or coarser-grained minerals are often present at the bottom of layered intrusions, and that this may be basic evidence of gravity sorting of crystals.

With regard to the tectonic settings of layered intrusions, it is noted by O'Driscoll & VanTongeren (2017) that many large layered intrusions, including the Bushveld and Skaergaard intrusions, are associated with anorogenic conditions within large igneous provinces. Furthermore, it has been suggested that there may be "a large number of mafic plutonic bodies deep in the continental crust that never made it to the surface because of their high density." (Winter, 2010). These large bodies may have formed in aborted rift zones (Winter, 2010). As such, Winter (2010) notes that many such intrusions of interest are associated with flood basalts,

which would form in continental rifts likely associated with mantle plumes, which is the most common environment for the production of large amounts of basaltic magma.

The temporal distribution of layered intrusions is very broad, and it has been noted that there is no particularly discernable correlation between the occurrence of layered intrusions and any specific geological timeframe (O'Driscoll & VanTongeren, 2017). However, it has been noted by Winter (2010) that the larger layered mafic intrusions are most commonly Precambrian in age. Alternatively, Winter (2010) suggests that particularly dense layered mafic intrusions may exist too deep in the crust. As such, it can be plausibly speculated that at least some large, geologically younger mafic layered intrusions are simply undiscovered.

As noted by Naslund & McBirney (1996), the processes that cause the formation of layered intrusions are diverse, and not uniform. Furthermore, O'Driscoll & VanTongeren (2017) note that some features found in layered intrusions are difficult to explain, and that postcumulus processes may have affected these rocks. Bowen's Reaction Series is relevant to basaltic magma, though it is not accurate to claim that minerals simply form cumulates in still-forming layered intrusions after crystallizing and sinking through a crystal mush (Winter, 2010). However, there is textural evidence for magmatic differentiation due to gravity settling, such as in ultramafic rocks (Winter, 2010). This is somewhat consistent with the experimental observation that forsterite crystals can gradually sink through a melt of olivine and pyroxene (Bowen, 1915), as forsterite would crystallize before pyroxene. Similarly, it is suggested by Wager & Brown (1968) that olivine commonly sinks in sills, while quartz-bearing rocks do not show much evidence of crystal sinking. This would support the trend of layering occurring primarily in mafic and ultramafic rocks, at least for the examples in which crystal sinking is believed to have occurred.

Relevantly, it has been proposed that some layered intrusions "are reconstituted rocks generated by crystal sorting of slurries deposited on the sloping floor of subsiding magma chambers." (Maier et al., 2013). This would generally support the importance of gravity/density settling. However, it is noted by Wager & Brown (1968) that turbulence within a melt could disrupt the process of density sorting. More broadly, the processes that specifically cause the layering of such bodies are classified by Namur et al. (2015) as dynamic and non-dynamic layer-forming processes. The dynamic process of magma include magma injection, and the non-dynamic processes include changes in pressure within the magma chamber (Namur et al., 2015). With regards to the point in time at which a given layer-forming process may operate, it is further noted by Naslund & McBirney (1996) that some relevant processes may operate at multiple stages of the formation of a layered intrusion.

A notable phenomenon found in the Skaergaard intrusion is the occurrence of a Sandwich Horizon. This phenomenon in igneous rocks has been described as "the layered series meeting with the downward-growing upper border series at the level of a sandwich horizon" (Latypov & Egorova, 2012). This means that a sandwich horizon, such as the one in the Skaergaard intrusion, crystallizes after the underlying and overlying rocks. In the case of the Skaergaard intrusion, the rocks have been proposed by Irvine et al. (1998) to be pegmatitic cumulates with a granophyric postcumulus mesostasis. It is noted by Winter (2010) that the Sandwich Horizon of the Skaergaard intrusion is believed to have formed at least partially from immiscible liquids, as evidenced by quartz and feldspar grains being segregated. Winter (2010) further notes that this would occur during tholeiite differentiation of an Fe-rich magma. With regards to chemistry, it is stated by Stewart & DePaolo (1990) that the Sandwich Horizon has the highest Nd concentration in the stratigraphy of the Skaergaard intrusion due to the locally very high degree of fractionation of the parent melt. Furthermore, it has been observed that "the olivine is almost pure fayalite, and the pyroxene is almost devoid of magnesium, the plagioclase is mostly only a sodic andesine," (Wager & Brown, 1968) which indicates an extremely evolved melt composition.

Layered intrusions are economically important, particularly with regards to such commodities as V, PGEs, and Cr. One major example of an economically important source of several such commodities is the Bushveld complex in South Africa. The Bushveld complex is noted by Maier et al. (2013) to exhibit prominent layering of magnetite and chromite, which are generally continuous along strike, albeit with varying thicknesses. The host rocks are mafic in composition, with orthopyroxenites and harzburgites listed as the most common host rock types (Maier et al., 2013, and references therein).

Another well-known example of an economically important layered intrusion is the Stillwater complex in Montana. The Stillwater complex is an example of a layered intrusion containing chromitite hosted in ultramafic rocks (McCallum, 1996). Additionally, disseminated chromite as well as PGEs are present in a reef referred to as the J-M reef (McCallum, 1996). The reef is hosted in the Banded and Ultramafic zones of the intrusion, with the Banded zone hosting the majority of the economic mineralization (Conn, 1979). The unexposed portion of the Stillwater complex is believed, due to a positive gravity anomaly, to be as much as nine times the size of the exposed section (Winter, 2010). As such, it can be inferred that the area remains prospective for further exploration.

1.2 Fe-Ti-V Deposits

Fe-Ti, and Fe-Ti-V deposits have been documented worldwide, with anorthositic bodies serving as host rocks for such deposits of Proterozoic age (Gross, 1996; Herrington, 2011). Additionally, these commodities may occur at economic grades within a gabbroic layered intrusion, particularly in titaniferous magnetite (Gross, 1996). As described by Gross (1996), this titaniferous magnetite of Fe-Ti deposits may include ilmenite and titanomagnetite, in addition to the typical iron ore minerals magnetite and hematite, and these ore minerals tend to occur in disseminated form. These minerals can also occur in massive form, such as in the Bushveld complex. Other styles of mineralization in Fe-Ti deposits are described by Gross (1996), including mineralization as late-stage dykes, and in the adjacent skarn rocks. It has been suggested that in the case of anorthosite-hosted Fe-Ti deposits, for example, the oxides may be younger than their host rocks, such as in the Tellnes deposit in Norway (Duchesne et al., 1993, as cited in Gross, 1996). However, this may be disputed in the case of the Sybille deposit in Wyoming, due to results obtained by U-Pb dating showing the same age range of the ore minerals and their host rocks (Scoates and Chamberlain, 1993, as cited in Gross, 1996). As such, dating of the ore minerals and their respective host rocks would sometimes yield results supporting coeval oxide mineralization with the formation of the host rocks.

The Fe-Ti deposits in gabbroic and leucogabbroic intrusions are described more specifically as "containing layers of disseminated titaniferous magnetite which alternate with layers of feldspar and mafic silicate minerals." (Gross, 1996). In some cases, these ore-bearing layers may be laterally extensive, with some being up to several kilometers in length (Gross, 1996). Ilmenite is described by Gross (1996) as being present in the form of exsolution intergrowths in magnetite grains, and as independent grains. Gross (1996) describes the oxides as having an association with minerals such as plagioclase, and mafic minerals such as olivine and pyroxenes. This association between oxides and the silicate minerals plagioclase, olivine, and the pyroxenes is observed in deposits hosted by anorthositic and gabbroic bodies (Gross, 1996).

The formation of Fe-Ti oxides in cumulate rocks has occurred in the Skaergaard intrusion. This is associated with adcumulus growth, as described by Humphreys (2009). The gradually decreasing (rimward) An content is accompanied by an increase in TiO_2 content until reaching An_{55}, at which point TiO_2 content decreases due to saturation of the Fe-Ti oxide minerals (Humphreys, 2009). As such, this phenomenon is relevant in understanding the genesis of Fe-Ti deposits hosted by layered intrusions. It should be noted that zonation is influenced by factors such as the mobility of the intercumulus liquid, which, if in communication with the parent

magma, may result in adcumulate-style crystallization without producing zoned crystals, while an immobile liquid would crystallize in the orthocumulus style (Humphreys, 2009, and references therein). From this, it can be inferred that some Fe-Ti deposits may not exhibit this phenomenon. However, this would imply that observed rimward changes (or lack thereof) in TiO_2 content in cumulus plagioclase would indicate adcumulus or orthocumulus crystallization.

The co-occurrence of vanadium with iron and titanium is in V-bearing titanomagnetite (Bauer et al., 1996). Additionally, vanadium is described by Force (1991) as being a byproduct of titanium mining from orebodies in anorthosite-ferrodiorite host rocks. This is consistent with the assertion by Cawthorn et al. (2005) that vanadium occurs in large mafic igneous bodies. It is noted by Cawthorn et al. (2005) that vanadium behaves compatibly in magnetite, and that magma crystallizing after the V-bearing magnetite will be V-depleted due to the high partition coefficient. Furthermore, it has been observed that there is a "lack of evidence for magma addition relating to magnetite formation" (Cawthorn et al., 2005). As such, it can be inferred that vanadium deposits form in closed magmatic systems. It is also noted by Cawthorn et al. (2005) that the vanadium-bearing magnetite crystallizes relatively high in a layered intrusion. This may imply that vanadium deposits form relatively late in the formation of the intrusive host body.

The crystallization of Fe-Ti oxides in the Skaergaard intrusion is described by Humphreys (2009) as beginning with a low bulk partition coefficient of Ti ($D_{Ti}^{B} = 0.20$) before the melt became saturated by Fe-Ti oxides, at which point the bulk partition coefficient is high ($D_{Ti}^{B} = 3.17$). At this point, the Fe-Ti oxides crystallized simultaneously with clinopyroxene oikocrysts, and plagioclase overgrowth (Humphreys, 2009, and references therein).

It is noted by Reguir et al. (2008) that oxygen fugacity has a proportional relationship with Mn compatibility in magnetite, and an inverse relationship with V compatibility in magnetite. Reguir et al. (2008) also notes that temperature has a proportional relationship with V compatibility in magnetite. However, it has been asserted that there is "no systematic trend in average Mn content of iron oxides and the temperature of formation" (Dupuis & Beaudoin, 2011).

One particular hypothesis for the formation of Fe-Ti mineralization involves liquid immiscibility between two phases in a magma chamber, with one being oxide-rich, and the other being silicate-rich, as described by Lister (1966). The hypothesis states that the crystallization of a melt would cause the enrichment of Fe and Ti, eventually resulting in the separation of an Fe-Ti-rich magma from the silicate magma (Lister, 1966). This hypothesis is supported by the existence of silicate globules within oxide grains in the Duluth gabbro complex in North America (Lister, 1966 and references therein). The Fe-Ti rich phase would also have become enriched in oxygen due to the presence of water (Lister, 1966). Lister (1966) states that convection currents

would play a role in the physical motion of the still-crystallizing melt. Variations in the Cr, V, and Mg content of oxides are believed, in the case of the Duluth gabbro complex, to indicate different stages of crystallization of oxide minerals, with oxide grains containing less Cr, V, and Mg believed to have crystallized from more evolved magma (Lister, 1966). With regards to the identity of the oxide minerals in the Duluth complex, it has been observed that "Subhedral to anhedral grains of medium-grained magnetite and of ilmenite, which have sharp, gently curved mutual boundaries, are present, but the magnetite grains are actually an extremely fine intergrowth of magnetite and ulvöspinel" (Lister, 1966). This would have implications regarding the crystallization of the oxide phase. Additionally, it has been proposed that liquid immiscibility is responsible for the presence of an Si-rich layer overlying Fe-rich rocks in the Bushveld complex (VanTongeren & Mathez, 2012). It should be noted that this hypothesis is not accepted in all cases of Fe-Ti deposit formation, as the role of liquid immiscibility is rejected in the case of the Morin Complex in Canada by Emslie & Ermanovics (1975).

Another hypothesis for the formation of Fe-Ti mineralization is that the oxide ore minerals, along with apatite, settle at the bottom of a layer after crystallization (Emslie & Ermanovics, 1975). As further described by Emslie & Ermanovics (1975), this would cause the denser, oxide minerals to settle lower in the layer, with a decreasing apatite to oxide ratio with increasing depth. Emslie & Ermanovics (1975) assert that the mineralogical data from the Morin Complex are consistent with this hypothesis. Furthermore, Pang et al. (2007) assert that the oxide ore minerals of the Panzhihua intrusion in China also formed by gravitational settling and sorting of mineral crystals from their ferrogabbroic parent magma. Evidence for this phenomenon occurring during the crystallization of the magma include the observation that the stratigraphically lower part of the intrusion hosts a significant portion of the oxide crystals, and the observation that forsteritic cumulus olivine in the intrusion contains inclusions of Fe-Ti oxide minerals (Pang et al., 2009). As there are multiple examples of this occurrence, it can be inferred that other Fe-Ti deposits may have formed in such a manner. According to Pang et al. (2007), this process of formation would occur early in the crystallization of the melt, and the crystallization would occur under anhydrous and high pressure conditions. Pang et al. (2007) notes that the required parent melt chemistry is rarely found in basaltic magmas, and that the available data suggests that mildly oxidizing conditions would be present during crystallization. It may be noted that, at least in the case of the Panzhihua intrusion, multiple magma pulses are believed to have been introduced during the crystallization of the intrusion (Pang et al., 2009). This is due to an increase in anorthite content of plagioclase over two separate vertical intervals, and increases in the magnesium content of mafic minerals over one of these intervals (Pang et al., 2009). It is speculated that as "Fe-Ti

oxides are cumulus throughout the Panzhihua intrusion, these intervals record the recharge and mixing of more primitive (i.e. Fe-Ti-V-undepleted) magmas." (Pang et al., 2009). Additionally Pang et al. (2009) propose that cross-cutting of Fe-Ti oxide minerals in some mafic intrusion- and Proterozoic anorthosite complex-hosted deposits may have been caused by the collapse of stratiform oxide horizons into the still partially-molten magma underneath. This is the explanation proposed by Pang et al. (2009) for such a phenomenon in the Jianshan segment of the Panzhihua intrusion. This explanation may also account for some structural irregularity in other deposits, not necessarily predicted by the gravity settling model.

2.0 Geology Background

2.1 Regional Geology of Fennoscandia

The Fennoscandian shield comprises the bedrock of Norway, Sweden, Finland, and the Kola Peninsula in northwest Russia. The Archean Karelian and Kola cratons comprise much of the bedrock of Finland, with only a small portion of Finnish bedrock belonging to the Norbotten craton. The Karelian and Kola cratons are primarily composed of granitic rocks, with the notable presence of greenstone belts (such as the Central Lapland Greenstone Belt). After the Archean eon, the bedrock of Fennoscandia experienced multiple significant tectonic events including a rifting event between 2.5 and 1.9 Ga, as well as the Svecofennian, Sveconorwegian, and Caledonian orogenies. Much of the Fennoscandian shield is considered to be prospective for numerous ore deposit types, including Fe-Ti-V deposits, banded iron formations (BIFs), diamondiferous kimberlites, orogenic gold deposits, porphyry Cu-Au-(Mo), and Ni-Cu-PGE deposits. A map of Finnish ore deposits is given in Figure 2.

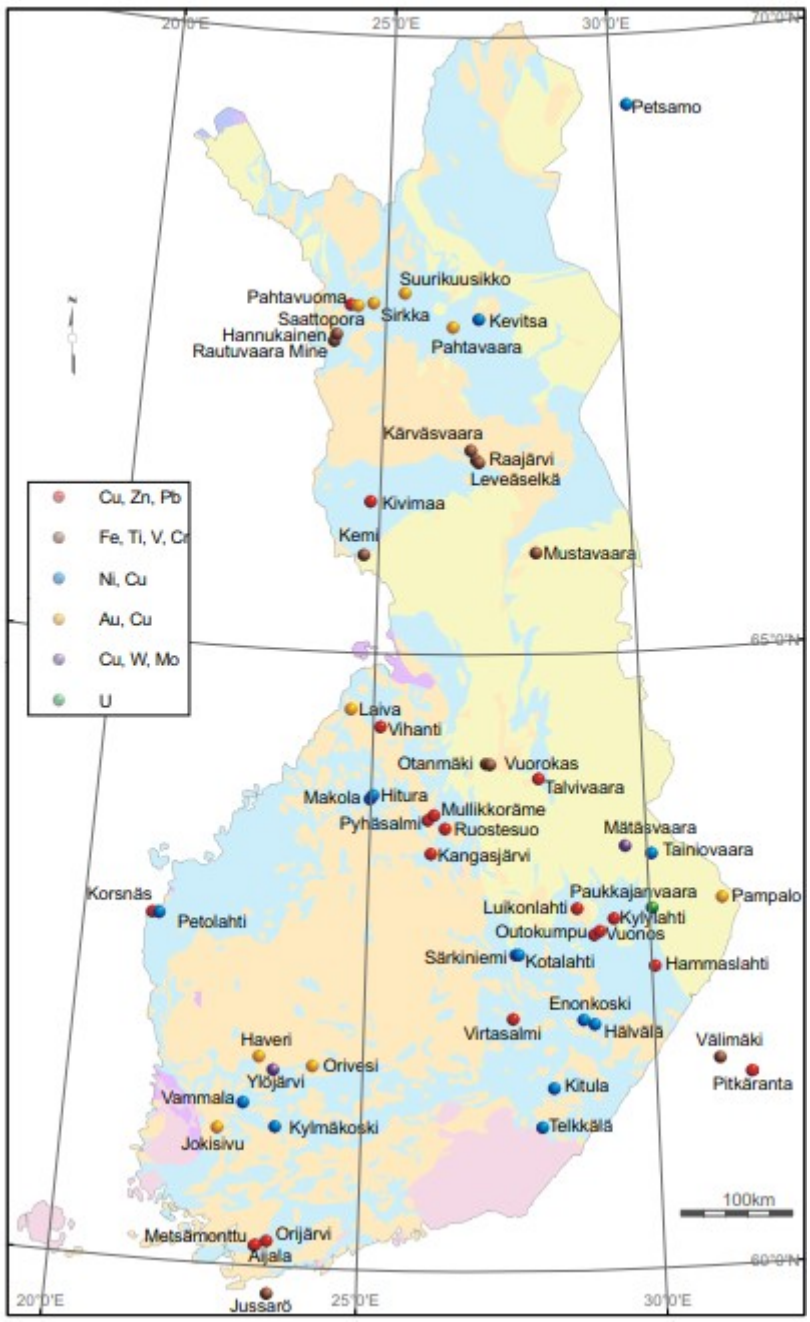

Figure 1: Map of Finnish ore deposits, from Haapala & Papunen (2015). Reprinted with permission from Elsevier, B.V.

Much of the bedrock of Fennoscandia is Precambrian in age. Hanski (2015) notes that the Fennoscandian and Ukrainian shields are collectively the oldest rocks cropping out in Europe. The age of the Archean basement of the Fennoscandian shield ranges from 3.5 to 2.5 Ga, and these rocks are covered by volcanic and sedimentary rocks with ages ranging from 2.5 to 1.9 Ga (Hanski, 2015). In addition, the 1.93-1.8 Ga Svecofennian orogenic belt is present, comprising (in addition to the Archean basement and its cover rocks) the third large-scale unit of the Fennoscandian shield (Hanski, 2015). With regards to economic geology, it has been noted that

"the metallogenic history of Finland corresponds well with the global pattern seen in Precambrian shields, but the degree of metal endowment is not necessarily similar to that of other shields." (Hanski, 2015). As such, the temporal distribution of some deposit types may be reflected in the Fennoscandian and other shields, but it can reasonably be assumed that the Fennoscandian shield is not equally prospective as others for at least some metals.

The Karelian and Kola cratons are divided by the Belomorian mobile belt and the Lapland granulite belt, with the Kola rocks cropping out in northeastern Finland (Hanski, 2015). In addition, the Kola rocks crop out in the Kola Peninsula in northwestern Russia. It may also be noted that the Lapland granulite belt, and the Belomorian mobile belt, are the metamorphosed remnants of the 1.93-1.91 Ga Lapland-Kola orogeny (Daly et al., 2006).

The Karelian craton contains multiple identified magmatic suites, including the tonalite-trondhjemite-granodiorite (TTG) suite, with an age range of 2.83-2.72 Ga, to the granodiorite-granite-monzogranite (GGM) suite, with an age range of 2.73-2.66 Ga (Hanski, 2015, and references therein). Other igneous or metaigneous rocks identified in the Karelian craton include trondhjemitic gneisses dated to ~3.5 Ga, sanukitoids dated to 2.74-2.72 Ga, and a quartz diorite-quartz monzodiorite (QQ) suite dated to ~2.70 Ga (Hanski, 2015, and references therein). In addition, the Fennoscandian shield includes multiple greenstone belts, including the roughly 2.4 – 1.9 Ga Central Lapland Greenstone Belt, and the Archean Kuhmo belt, which are composed of mafic to ultramafic igneous and metamorphic rocks.

2.2 2.44 Ga magmatism, layered intrusions, volcanic rocks, mafic dikes

As noted by Iljina & Hanski (2005), a portion of the Fennoscandian shield underwent a period of mafic magmatism. This magmatism is known as the Sumian magmatism, which occurred between ~2.50 and 2.44 Ga, in association with the break-up of the Precambrian supercontinent (Hanski, 2015, and references therein). This magmatism produced the Tornio-Näränkävaara belt, as well as several mafic dyke suites, and two granite suites (Luukas et al., 2017). Several volcanic rocks are also associated with the 2.44 Ga magmatism. It is also noted by Hanski (2015) that Sumian supracrustal rocks are abundant in the Salla belt in eastern Lapland, and that these rocks vary in composition from basaltic andesites to rhyolites.

The Tornio-Näränkävaara belt has a history of successful mineral exploration and exploitation, notably containing the Kemi chromite mine, and the Mustavaara Fe-Ti-V deposit, as well as PGE mineralization in the Penikat intrusion. Other known mineralization includes Cu-Ni-PGE mineralization in the Portimo complex (Iljina & Hanski, 2005, and references therein).

Figure 2: Geological map showing the 2.44-2.5 Ga layered intrusions the northeastern Fennoscandian Shield. From Iljina et al., 2015. Reprinted with permission from Elsevier, B.V.

The Tornio-Näränkävaara belt extends from Sweden in the west, to Russia in the east, and most of the belt is in Finland. The belt is described by Iljina & Hanski (2005) as almost following the Arctic Circle, though being discontinuous. It consists of multiple mafic intrusive bodies, as well as A-type granites, having intruded into a failed rift (Iljina & Hanski, 2005). Several major intrusions of the Tornio-Näränkävaara belt, such as the Kemi, Penikat, and Koillismaa intrusions, are displayed in Figure 3. It is noted by Iljina & Hanski (2005) that the mafic intrusions are bounded by older felsic gneisses to the south, and Paleoproterozoic volcano-

sedimentary rocks to the north. The mafic rocks are stated by Iljina & Hanski (2005) to be gabbroic in their composition, and there is known presence of serpentinized ultramafic rocks in the same intrusive belt.

Prior to the emplacement of the intrusions of the Koillismaa intrusive complex, extensive volcanism occurred in association with rifting (Iljina et al., 2001, and references therein). This rifting may have caused the formation of a still-preserved graben structure (Iljina et al., 2001). It is further noted by Iljina et al. (2001) that a mixture of volcanic and sedimentary material was also deposited into a younger basin after the emplacement of the Koillismaa intrusive complex, in the timeframe of 2.45 to 2.20 Ga.

Within the Tornio-Näränkävaara belt exists the Koillismaa-Näränkävaara intrusive complex. The Koillismaa-Näränkävaara intrusive complex is geographically extensive, measuring a total area of over 100 km in length (Alapieti, 1982). Alapieti (1982) states that the Koillismaa-Näränkävaara complex was formed 2.436 $\pm$ 5 Ga, as determined by U-Pb dating of zircon by Dr. O. Kouvo of the Geological Survey of Finland (GTK). Furthermore, it is suggested by Alapieti (1982) that the Koillismaa-Näränkävaara complex may have been formed from more than 2000km^3 of magma. The still-crystallizing magma is speculated to have been periodically mixed with undifferentiated magma, due to the low overall differentiation over the 3 km thickness of the section (Alapieti et al., 1979, and references therein).

The Koillismaa-Näränkävaara complex is subdivided into two intrusions linked by a gravity anomaly, which has been suggested to be a mostly-unexposed dike (Figure 3) (Alapieti, 1982). It is speculated that within the Tornio-Näränkävaara belt, "the individual intrusions were probably connected by dikes or intermediate magma chambers at the time of emplacement." (Iljina & Hanski, 2005). In addition, Alapieti (1982) speculates that the dike may actually be another layered intrusion. Geophysical data suggests that the dike is "at an average depth of about 1.4 km below the present erosional surface, and [that] the anomalous mass [is] about 3 km wide and very deep, going down almost vertically and becoming narrower at the same time" (Alapieti, 1982). As such, the study of this body is difficult, and would require extensive, deep drilling to verify much of the geophysical data.

The easternmost of the two bodies of the Koillismaa-Näränkävaara complex is the Näränkävaara intrusion, while the western body is left unnamed by Alapieti (1982), who describes the body as basic, and capped by granophyric rocks. The unnamed body is referred to by Karinen (2010) as the Koillismaa Intrusion. It is mentioned by Iljina et al. (2001) that the Näränkävaara intrusion is a part of the feeder of the Koillismaa Intrusion. It is also explained by Iljina et al. (2001) that at this time (2.45 Ga), the existing felsic volcanic rocks were altered to granophyric

rocks. It is noted by Iljina & Hanski (2005) that the Koillismaa intrusion has a tectonic contact in the west with a greenstone belt. The Koillismaa intrusion, is divided into seven blocks, and it is stated that they, "from south to north, are those of Pirivaara, Syöte, Porttivaara, Kuusijärvi, Lipeävaara, Kaukua and Murtolampi." (Alapieti, 1982). Alapieti (1982) further notes that these blocks have an overall synclinal form due to the change in attitude from the northerly-dipping blocks in the south, to the southerly- or southwesterly-dipping blocks in the north. According to Alapieti (1982), the exposed layering within the Näränkävaara intrusion is gently dipping, though magnetic data indicates unexposed steepening of the layering. A map of the Koillismaa-Näränkävaara complex is given in Figure 4.

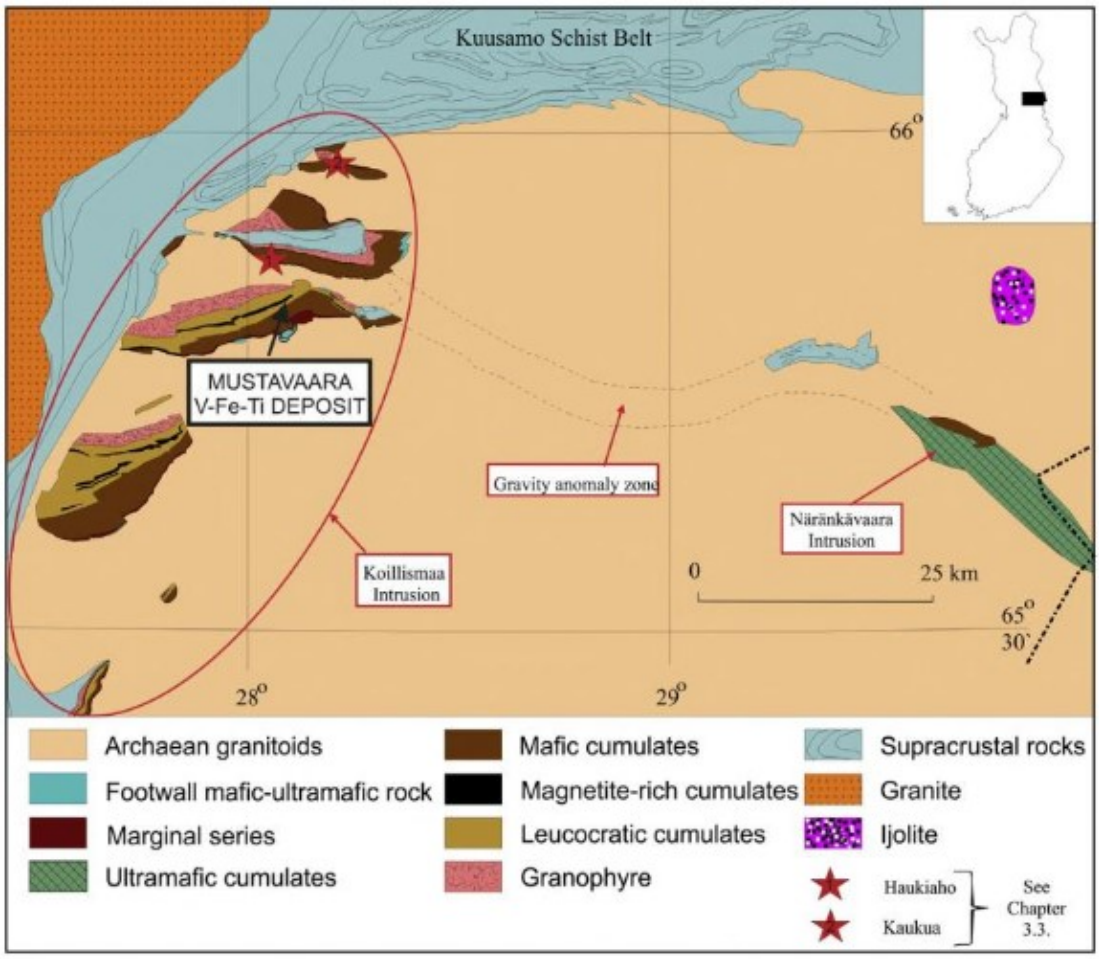

Figure 3: Regional map of the Koillismaa-Näränkävaara intrusion, from Karinen et al. (2015). Reprinted with permission from Elsevier, B.V.

The four southernmost blocks of the western intrusive body contain rocks that have been described as microgabbronorite xenoliths (Iljina & Hanski, 2005, and references therein). These xenoliths are noted by Iljina et al. (2001) to be associated with PGE mineralization. This

mineralization is described by Iljina et al. (2001) as reef-type, with the PGEs contained in unspecified sulfide minerals. Karinen (2010) notes that the PGE reef, known as the Rometölväs Reef, occurs at a stratigraphic discontinuity where primary orthopyroxene disappears and is replaced by clinopyroxene and pigeonite. The microgabbronorites are described as being fine-grained and equigranular, and lacking a cumulus texture (Iljina et al., 2001; Iljina & Hanski, 2005). In addition, these microgabbronorites have been interpreted as dykes rather than as xenoliths (Karinen, 2010, and references therein). It has been further noted that "Stratigraphically the [microgabbronorites are] located well below the magnetite gabbro, concordant to igneous layering." (Iljina et al., 2001). As such, these PGE-enriched rocks can be discussed separately from the Mustavaara Fe-Ti-V deposit.

2.3 Mustavaara Fe-Ti-V deposit, different blocks, stratigraphy, mineralization

The Mustavaara Fe-Ti-V deposit is located in the Porttivaara block, in the western portion of the Koillismaa intrusive complex (Figure 3) (Alapieti, 1982). The gabbroic nature of the host rock is consistent with other layered intrusions, as per the general description of layered intrusions given by Naslund & McBirney (1996). Furthermore, the age of the Peräpohja layered intrusion suite is consistent with the description of layered intrusions as commonly dating to the Proterozoic eon, as given by Scoates & Wall (2015).

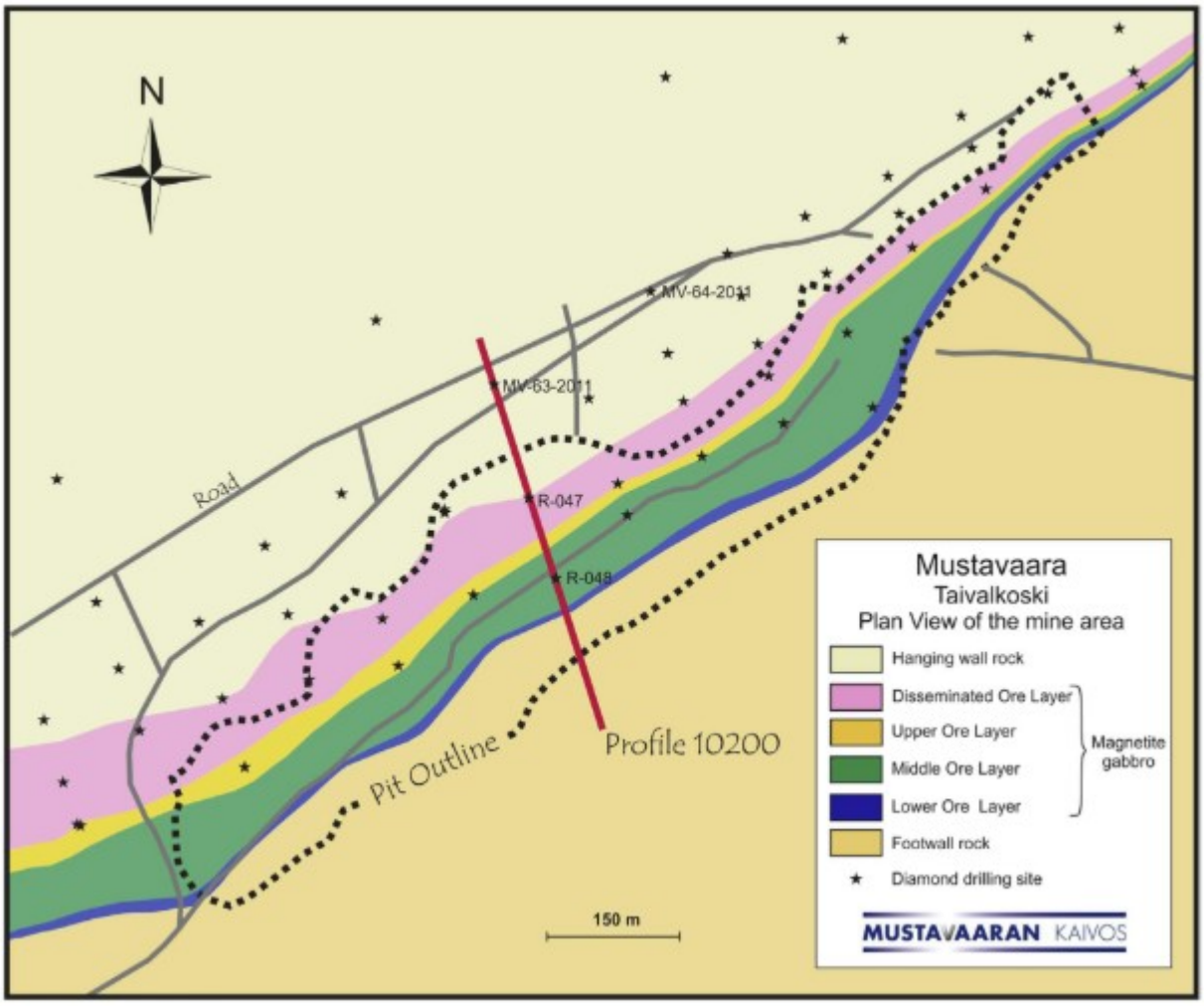

Figure 4: Map of Mustavaara Deposit Ore Layers, from Karinen et al. (2015). Reprinted with permission from Elsevier, B.V.

The Mustavaara deposit was discovered in 1967 after a decade of prospecting and exploration work, beginning with the observation of compass anomalies by a local forestry manager, Antti Oikarinen, in 1957 (Karinen et al., 2015, and references therein). His magnetite-bearing samples, as well as the availability of aeromagnetic data collected by GTK, led the Otanmäki Company to commence exploration that ultimately resulted in the discovery of the deposit (Karinen et al., 2015, and references therein). The mine was later developed by the Rautaruukki Steel Company before being closed due to low vanadium prices in 1985 (Karinen et al., 2015, and references therein).

The Mustavaara deposit is not the only example of a Fe-Ti-V deposit in the Fennoscandian shield, as the Otanmäki deposit of Finland, and the Smålands Taberg deposit of Sweden, are also known. Of these, Otanmäki is a particularly notable deposit with a history of mining during roughly the same timeframe as the production of the Mustavaara open-pit mine.

Efforts have been made towards reopening the Otanmäki and Mustavaara mines, particularly the Otanmäki mine. However, as of May in 2020, neither is in production.

The Mustavaara deposit is hosted in a magnetite gabbro in the Porttivaara block, and the vanadium is in ilmenomagnetite (Juopperi, 1977). Magnetite enrichment is also present in the Pirivaara, Syöte, and Kuusijärvi blocks of the western intrusive body (Iljina & Hanski, 2005). The magnetite gabbro is described by Karinen et al. (2015) as compositionally a plagioclase-augite-ilmenomagnetite adcumulate, texturally described as equigranular, and small- to medium-grained. As can be observed in thin section, the plagioclase grains are idiomorphic and show a preferential alignment defining igneous lamination. Measurements of plagioclase grains reveal a grain size range of 1-5 mm in length (Karinen et al., 2015). Optical microscopy also reveals sausseritization of plagioclase. Furthermore, the primary augite is extensively altered to uralite (Juopperi, 1977). According to Karinen et al. (2015), the ilmenomagnetite is generally interstitial, though there are also idiomorphic grains present in the deposit. The idiomorphic grains are particularly common in the disseminated ore layer (DOL) in the stratigraphically higher part of the host rock (Karinen et al., 2015). It should also be noted that semimassive to massive ore is present in a <0.5 m thick layer above the DOL, though this is only true in some drill cores (Karinen et al., 2015). Ilmenomagnetite is present in the Porttivaara block due to subsolidus oxidation of titanomagnetite, and the composition of the titanomagnetite has been calculated to have been (by weight percent) 42.0 Fe_2O_3, 44.0 FeO, and 14.0 TiO_2 (Karinen, 2010).

The deposit is specifically located in the lower part of the magnetite gabbro, with a total thickness of roughly 80 m, and a 40° northerly dip (Karinen et al., 2015). To the east of the existing open pit, the deposit thins to roughly 20 m in thickness where the dip steepens from 40° to 60° (Karinen et al., 2015). A geological map of the area, with the deposit marked, is given in Figure 4.

Variations in the ilmenomagnetite content of the magnetite gabbro cause the division of the deposit into the 5 m thick lower ore layer (LOL), the 15-50 m thick middle ore layer (MOL), the 10-40 m thick upper ore layer (UOL), and the DOL, as described by Karinen et al. (2015). Of these four ore layers, the LOL generally has the highest weight percent of ilmenomagnetite, at 20-35 wt %, followed by the UOL at 15-25 wt %, the MOL at 10-15 wt %, and the DOL at less than 10 wt % (Karinen et al., 2015). A map and cross section of the ore layers in the area of the existing open pit are given in Figure 4 and Figure 5, respectively. According to Karinen et al. (2015), the average ilmenomagnetite content by weight percent of the host rock within the defined deposit is 14.7, with an average V content of 0.88 wt. %. More specifically, the average V_2O_3 content of the magnetite grains is 1.7 wt. % in the UOL and the LOL, and 1.5 wt. % in the DOL

and the MOL (Karinen et al., 2015). These numbers pertain to concentrate compositions, as determined using the Dings Davis Tube (DDT) method. It is further noted by Karinen et al. (2015) that the average ilmenomagnetite content and V content of the ilmenomagnetite is 9.1 wt % and 0.77 wt %, respectively, in the host rock outside of the deposit.

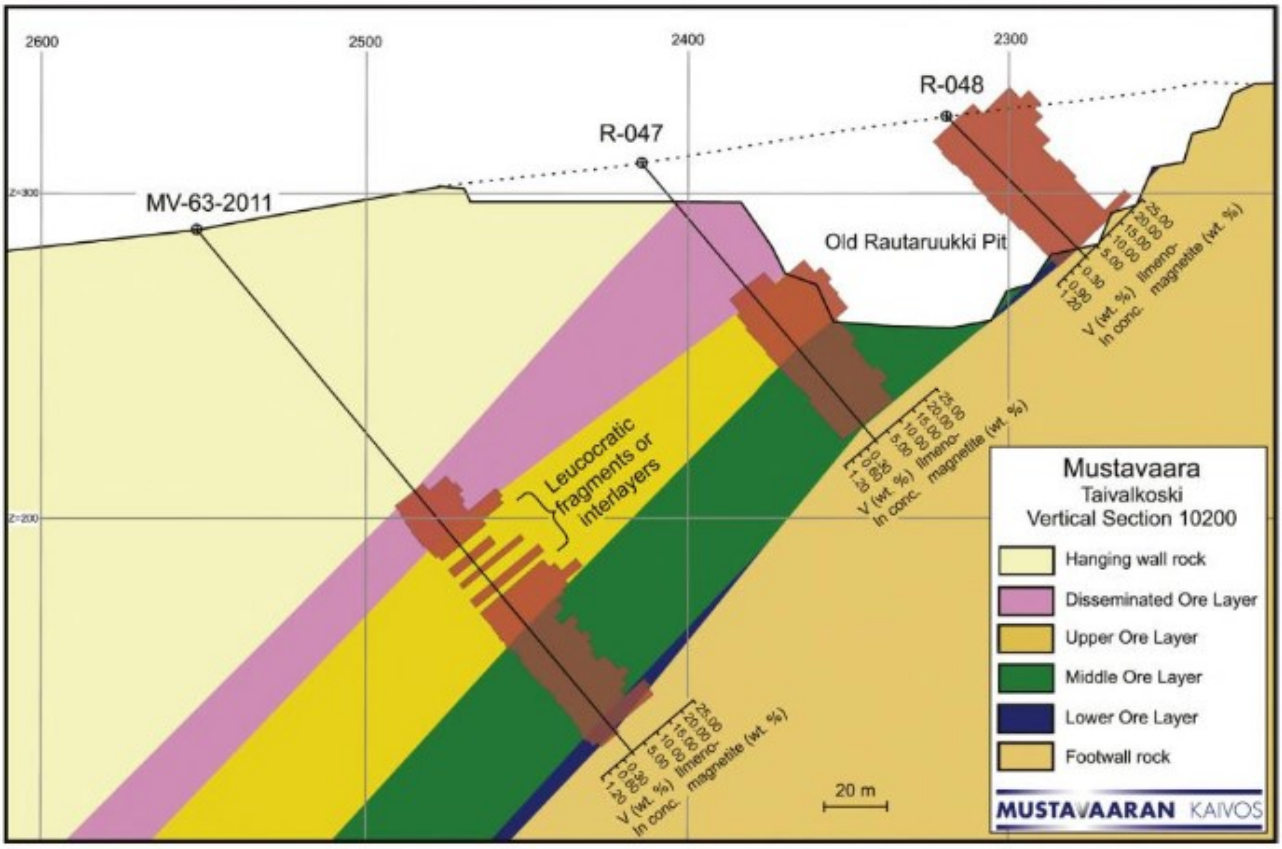

Figure 5: Cross-section of ore layers, from Karinen et al. (2015). Reprinted with permission from Elsevier, B.V.

The Mustavaara deposit is asserted by Karinen et al. (2015) to have been formed due to fractional crystallization. This is because the modal abundance of magnetite is within the known cotectic ratio, and the composition of plagioclase and primary augite are both consistent with this process (Karinen et al., 2015, and references therein). It should be noted that there is some variation in the V content of magnetite along the strike of the magnetite gabbro, with lower V contents occurring to the west of the deposit, possibly indicating that the magma in the area of the deposit was more evolved than in other parts of the intrusion, or that pressure conditions or oxygen content were different in other areas of the intrusive body (Karinen et al., 2015). It has been stated that, due to the sharp contact between the deposit and the footwall without evidence of oxide veins in the footwall, "it is likely that the Mustavaara ore was formed by relatively effective gravitative

concentration of oxide crystals, or by sorting of a magnetite slurry" (Karinen et al., 2015). The lack of oxide veins in the footwall is also specifically noted by Karinen et al. (2015) to be evidence against the earlier hypothesis of Juopperi (1977) that the Mustavaara deposit was formed by liquation, or liquid immiscibility. As such, the Mustavaara deposit may have formed in a manner somewhat consistent with the Fe-Ti mineralization model described by Emslie & Ermanovics (1975), albeit without the association with apatite. It should also be noted that a study has shown the presence of a V^{4+}/V^{3+} ratio of 0.18 in a magnetite sample from the Mustavaara deposit (Balan et al., 2006, as cited in Karinen et al., 2015), similar to the results from the Skaergaard intrusion, suggesting that the deposit was formed under oxygen fugacity of around the Ni-NiO buffer (Karinen et al., 2015).

3.0 Sampling, Petrography (mineralogy of samples)

Fourteen thin sections were provided by Dr. Tuomo Karinen of GTK. These thin sections were created by GTK in Kuopio, Finland, from various locations along a single borehole, labeled MV-64-2011, from the Mustavaara deposit.

The stratigraphy of the deposit along the borehole can be described as follows: the overburden is present from the surface to a depth of 12.50 m. The hanging wall is present from 12.50 m to 103.19 m. The DOL is present from 103.19 m to 115.04 m. The UOL is present from 115.04 m to 132.50 m. The MOL is present from 132.50 m to 159.75 m. The LOL is present from 159.75 m to 163.29 m. The footwall is present from 163.29 m to at least the bottom of the borehole at 179.30 m.

The thin sections are taken from depths ranging from 51.28 m to 177.70 m along the borehole. Each shows an adcumulate texture, with variable grain size that can generally be described as fine- to medium-grained. Modal abundances of plagioclase, oxides, and mafics and other minerals were obtained using the point counting method by Dr. Karinen. Igneous lamination is present to varying degrees, as evidenced by the alignment of the plagioclase grains. Alteration of the plagioclase grains, such as sausserite in the fractures, is variable, but present throughout the stratigraphy. The plagioclase is idiomorphic, and exhibits simple and lamellar twinning. Images and descriptions of representative thin sections from the hanging wall, footwall, and ore layers are given below. Images and descriptions of the other thin section are given in the appendices.

At 51.28 m, the hanging wall contains 65.9 vol% plagioclase, 5.0 vol% oxides, and 29.1 vol% mafics (altered clinopyroxene). The plagioclase can be described as euhedral, with grain size generally varying from 0.5 to 2 mm on the long axis (Figure 6). Twinning planes have variable sharpness (Figure 6). The plagioclase grains show moderate igneous lamination. The clinopyroxene grains have completely altered to green-colored amphibole with anhedral texture. These altered clinopyroxene grains are interstitial to the plagioclase grains. The oxide grains occur in disseminated form. The oxide grains can generally be described as euhedral, with some larger grains showing annealing texture. The oxide grain sizes generally vary from 0.1 to 0.5 mm in diameter. Images of the thin section from 51.28 m depth are given in Figure 6.

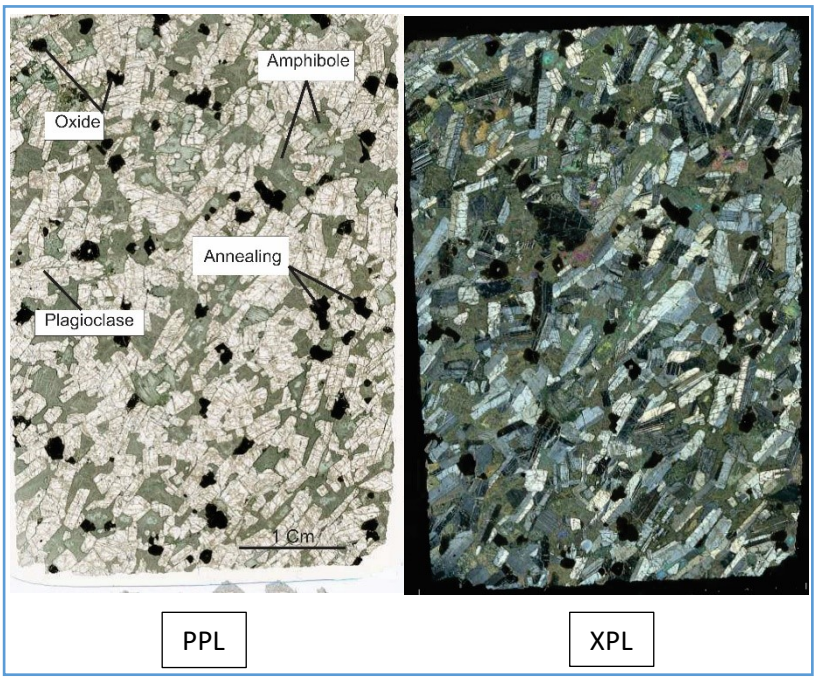

Figure 6: Microscope photos of thin section from depth 51.28 m (Hanging wall). PPL and XPL indicates plane polarized light and crossed polarized light, respectively. The width of each view is approximately 3 cm.

At 106.14 m, the DOL contains 48.5 vol% plagioclase, 11.3 vol% oxides, and 40.1 vol% amphibole (altered clinopyroxene). The plagioclase can generally be described as euhedral, with grain sizes generally varying from 0.3 to 0.8 mm on the long axis (Figure 7). The twinning planes have variable sharpness (Figure 7). The plagioclase shows moderate igneous lamination. The clinopyroxene grains have been altered to a green-colored amphibole with anhedral texture. The altered clinopyroxene grains are interstitial to the plagioclase grains. The oxide grains can generally be described as euhedral, with several larger grains showing annealing texture. The oxide grain size is generally 0.1 to 0.5 mm in diameter. Images of the thin section from 106.14 m depth are given in Figure 7.

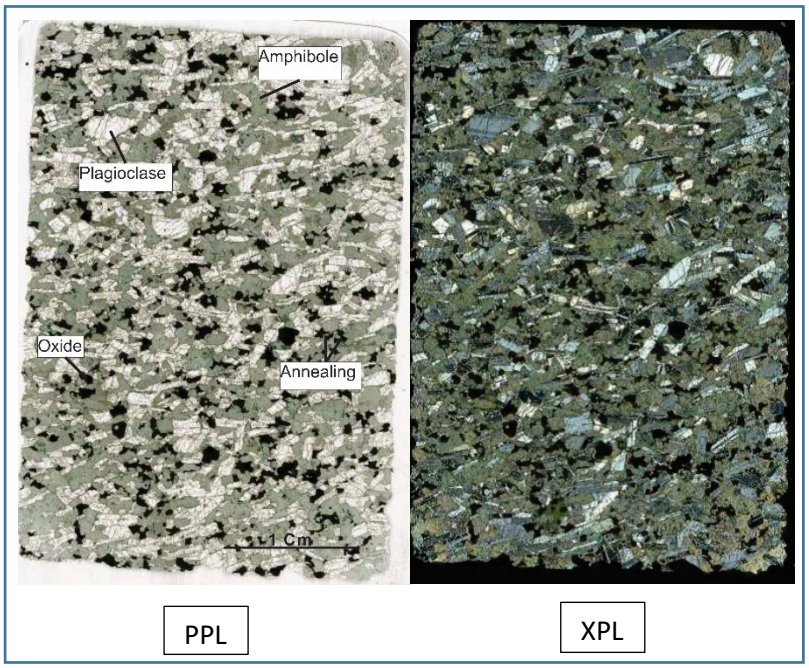

Figure 7: Microscope photo of thin section from depth 106.14 m (Disseminated ore layer). Note the oxide content is slightly higher than in the hanging wall. The width of each view is about 3 cm.

At 118.70 m, the UOL contains 54.6 vol% plagioclase, 21.2 vol% oxides, and 24.2 vol% amphibole (altered clinopyroxene). The plagioclase can be described as euhedral, with grain sizes generally varying from 0.5 to 1 mm along the long axis (Figure 8). Twinning planes have variable sharpness (Figure 8). The plagioclase shows weak lamination, which is sometimes difficult to identify due to extensive alteration. The clinopyroxene grains have been altered to a green-colored amphibole. The altered clinopyroxene is interstitial to the plagioclase grains. The oxide grains are euhedral and inequigranular, though some grains show anhedral texture after annealing. Oxide grain sizes generally ranging from 0.1 mm to around 1 mm in diameter. Images of the thin section from 118.70 m depth are given in Figure 8.

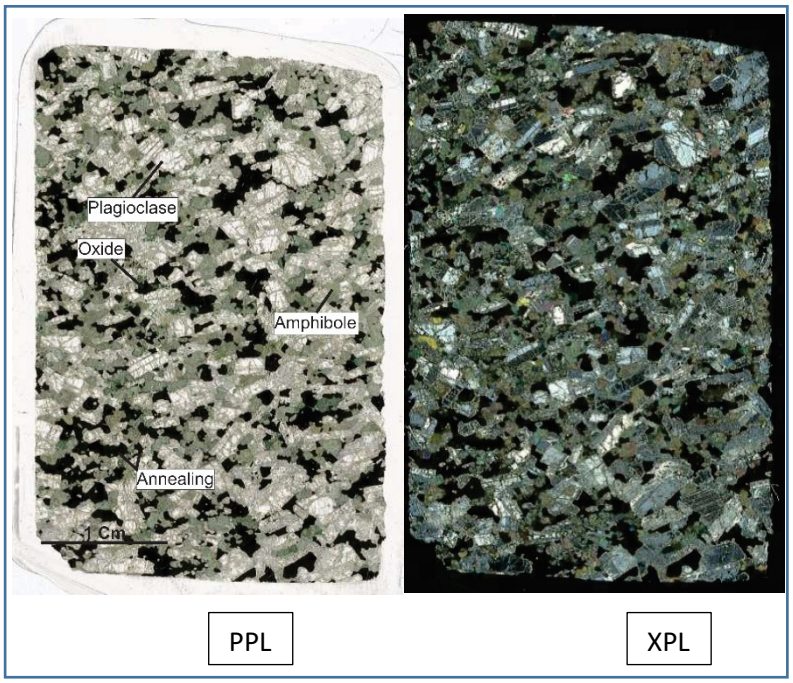

Figure 8: Microscope photo of thin section from depth 118.70 m (Upper ore layer). The width of each view is about 3 cm.

At 135.35 m, the MOL contains 52.7 vol% plagioclase, 14.6 vol% oxides, and 32.8 vol% amphibole (altered clinopyroxene). The plagioclase can generally be described as euhedral, and sub-equigranular to equigranular, with grain sizes generally varying from 0.6 to 0.8 mm, but sometimes difficult to estimate due to alteration (Figure 9). Simple twinning planes are dull, while lamellar twinning planes have variable sharpness (Figure 9). The plagioclase shows moderate igneous lamination. The clinopyroxene grains have been altered to a green-colored amphibole. The altered clinopyroxene is anhedral, and interstitial to the plagioclase grains. A minor amount of the oxide grains can be described as euhedral, while most grains show interstitial, anhedral texture after annealing. The oxide grain sizes are on the 1 mm scale in diameter. Images of the thin section from 135.35 m depth are given in Figure 9.

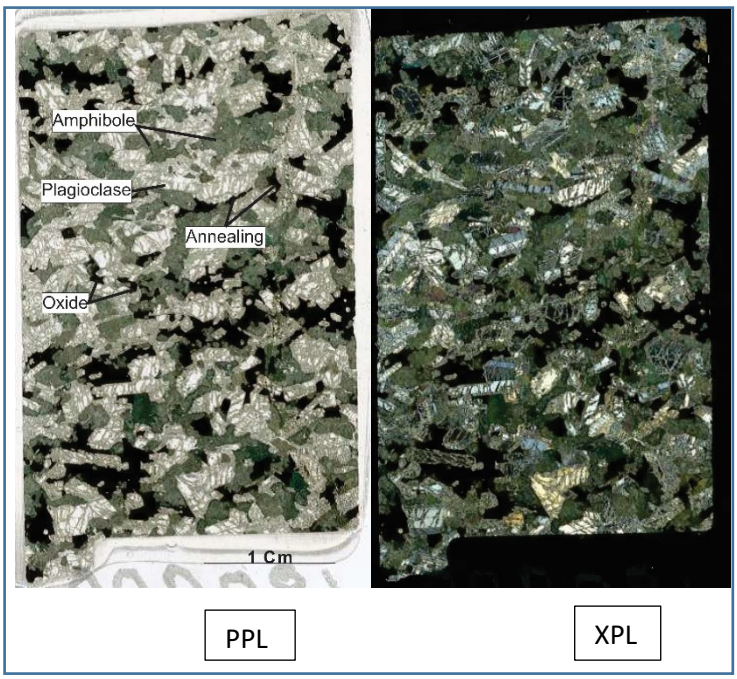

Figure 9: Microscope photo of thin section from depth 135.35 m (Middle ore layer). The width of each view is about 3 cm.

At 160.08 m, the LOL contains 46.7 vol% plagioclase, 40.5 vol% oxides, and 12.8 vol% amphibole (altered clinopyroxene). The plagioclase grains are euhedral, and grain sizes generally range from 0.6 to 0.8 mm, though abundant alteration makes an accurate estimation difficult (Figure 10). Twinning planes have variable sharpness (Figure 10). The clinopyroxene grains have been altered to a green-colored amphibole. The altered clinopyroxene is anhedral, and interstitial to the plagioclase grains. As the oxide abundance increases, almost all oxide grains show interstitial anhedral texture after annealing. The oxide grain sizes are on the 1 mm scale in diameter. Images of the thin section from 160.08 m depth are given in Figure 10.

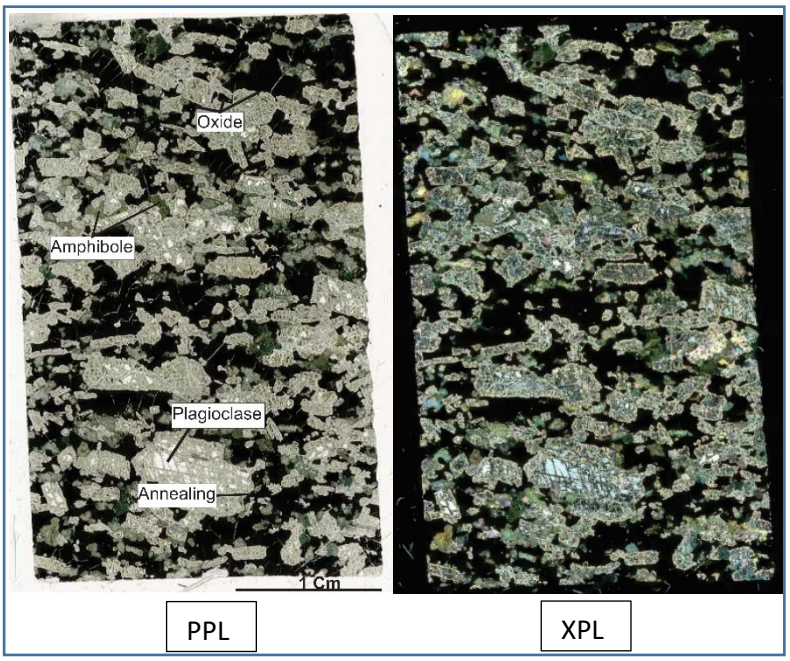

Figure 10: Microscope photo of thin section from depth 160.08 m (Lower ore layer). The width of each view is about 3 cm.

At 171.73 m, the footwall contains 74.1 vol% plagioclase, 3.7 vol% oxides, and 22.1 vol% amphibole (altered clinopyroxene). The plagioclase grains are euhedral, and grain sizes are generally 0.3 to 0.8 mm, but highly variable (Figure 11). Twinning planes have variable sharpness (Figure 11). The plagioclase shows igneous lamination. The clinopyroxene grains have been altered to a green-colored amphibole. The altered clinopyroxene is anhedral. The oxide grains are anhedral and interstitial to silicate minerals. The oxide abundance is rather low, with grain sizes varying, but generally 0.1 to 1 mm in diameter. Images of the thin section are given in Figure 11.

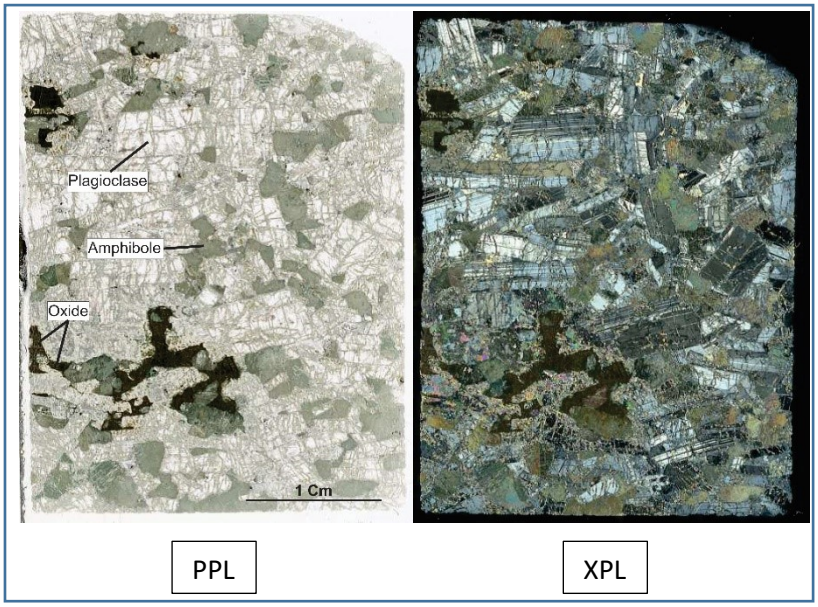

Figure 11: Microscope photo of thin section from depth 171.73 m (Footwall). The width of each view is about 3 cm.

An image of a plagioclase grain in the disseminated ore layer, with fractures containing sausseritization, is given in Figure 12.

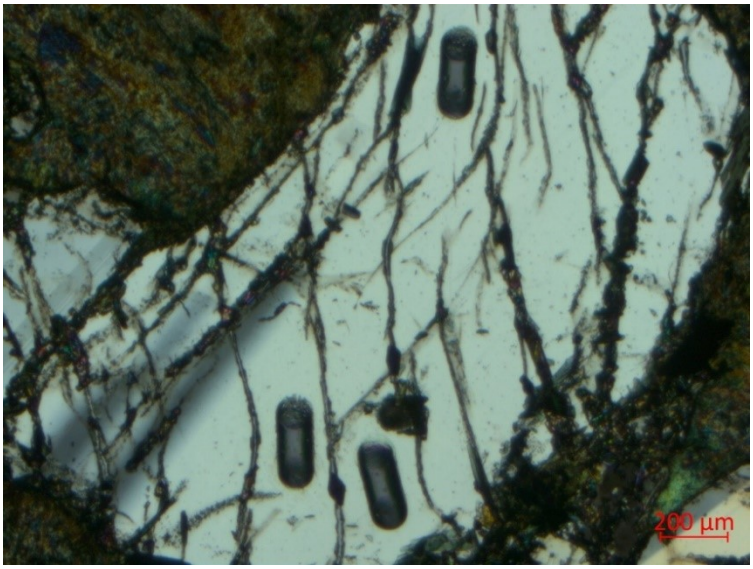

Figure 12: Plagioclase and augite grains from thin section 180193, taken from MV-64-2011 at a depth of 106.14 m. Note the alteration of the augite (top left), and the fracturing and alteration of the large plagioclase grain.

4.0 Research Method, EPMA, LA-HR-ICPMS, MC-ICP-MS

4.1 EPMA

Plagioclase grains from each of the 14 thin sections were analyzed at the Centre for Material Analysis at the University of Oulu. The analyses were accomplished using a Jeol JXA-8530F Plus field emission electron probe microanalyzer, and an older JXA-8200 microprobe. The analyses were performed under the following analytical conditions: a beam size of 10 μm, an accelerating voltage of 15 kV, and a current of 15 nA. The matrix correction, using the ZAF method, was applied to every one of the analyses.

The samples in this study are generally plagioclase-rich, and fresh plagioclase grains are typically easy to target for analysis. The traverse analyses of plagioclase grains are used to study the chemical zoning of plagioclase. Fresh domains of plagioclase grains were selected for analyses. In addition, some plagioclase grains were analyzed after LA-HR-ICPMS data was collected, to compensate for the lack of EPMA data in grains that were not initially planned. These newer spot analyses were chosen near the laser ablation spot.

4.2 LA-HR-ICPMS

Trace element concentrations of plagioclase from 14 thin sections were analyzed at the Geological Survey of Finland (GTK) in Espoo, using an AttoM Single Collector High Resolution Inductively Coupled Plasma Mass Spectrometry (HR-ICP-MS), which is coupled with Photon MachinesTM deep UV (193 nm wavelength) excimer laser system. Each spot analysis was conducted using 50 μm diameter beam size, a laser frequency of 10 Hz, a power of 4.68J/cm^2, and He-Ar carrier gas. Cores of plagioclase grains were selected for their lack of alteration, with a strong preference for locations from which EPMA data had already been taken. In addition, some spots were taken in an approximate “line” of spots traversing selected grains (spot traverse analyses). This was designed to observe the variations of trace element composition from core to rim of plagioclase grains. The gas background was collected for 20 s followed by 60 s of data acquisition. BHVO reference material was used for calibration and BCR as a monitor. The reduction of the data was computed using Glitter software, and using ^{29}Si as an internal standard. The results of the BCR standard measurements are similar to the reference values, and are presented in Table 4 in the appendices. The results of the samples are listed in Table 1.

4.3 LA-MC-ICP-MS

In situ Rb-Sr isotope composition analyses of plagioclase were performed by Laser Ablation MC-ICP-MS using a Nu Plasma HR multi-collector inductively coupled plasma mass spectrometer (MC-ICP-MS), and a Photon Machine Analyte G2 laser microprobe at GTK in Espoo. Samples, selected for their lack of alteration, were ablated in He gas (gas flows = 0.4 and 0.1 l/min) within a HelEx ablation cell (Müller et al., 2009). Every analysis taken from the thin sections was a line analysis, made in static ablation mode (^{84}Sr-Kr, ^{85}Rb, ^{86}Sr-Kr, ^{87}Rb-Sr, ^{88}Sr) using the following parameters: beam diameter: 110 μm, pulse frequency: 20 Hz, beam energy density: 3.0 J/cm^2. The MC-ICP-MS was equipped with 9 Faraday detectors and amplifiers with 1011 Ω resistors. The measured isotope ratios were corrected for instrument fractionation using an exponential law, and an ^{86}Sr/^{88}Sr value of 0.1194. The isobaric interference of ^{87}Rb on ^{87}Sr was monitored, and corrected using the ^{85}Rb ion signal and a value of 0.38571 for the ^{87}Rb/^{85}Rb ratio. The isobaric interference of ^{86}Kr on ^{86}Sr was corrected using a 30s background measurement, preceding each ablation. The average total Sr signal obtained for plagioclase samples was 0.25 V. Under these conditions, 120 s of ablation are required in order to obtain an internal precision of $\leqslant \pm$ 0.000020 (2s). The accuracy of the laser ablation protocol was periodically verified throughout the measurement process by analysis of an in-house plagioclase standard, obtained from a megacryst from the Cameroon line (sample Mir a, Rankenburg et al., 2004). The laser ablation parameters were quite similar between the samples and the standard measurements. The average ^{87}Sr/^{86}Sr value obtained for the plagioclase standard during the measurement process was 0.703062 ± 0.000060 (2s, n=23), while the solution value is 0.703057 ± 0.000007 (2s, average duplicated analysis by MC-ICP-MS on two separate grains). Throughout the measurements, the average ^{84}Sr/^{86}Sr was 0.05630 ± 0.00018 (2s, n=8), which is similar to the accepted values of ca. 0.056 ± 0.0001 (Thirlwall, 1991). The shift observed between the average measured and reference values has been applied to all of the samples. The standard BHVO-2G gave a value of 0.703462 +- 237 (1s, n=12) within error of the certified value (0.703476 +- 7, GEOREM database preferred value). The BHVO and plagioclase standard measurements for LA-MC-ICP-MS are given in Tables 5 and 6, respectively, in the appendices.

5.0 Results

5.1 Compositional variation along stratigraphy

Trace elements Ti, V, Mn, Ce, Eu, and An# were plotted against depth. For selected grains of samples from the hanging wall, magnetite gabbro, and footwall, traverse analyses of trace element concentration and An# have been plotted against the distance to the rim of each grain.

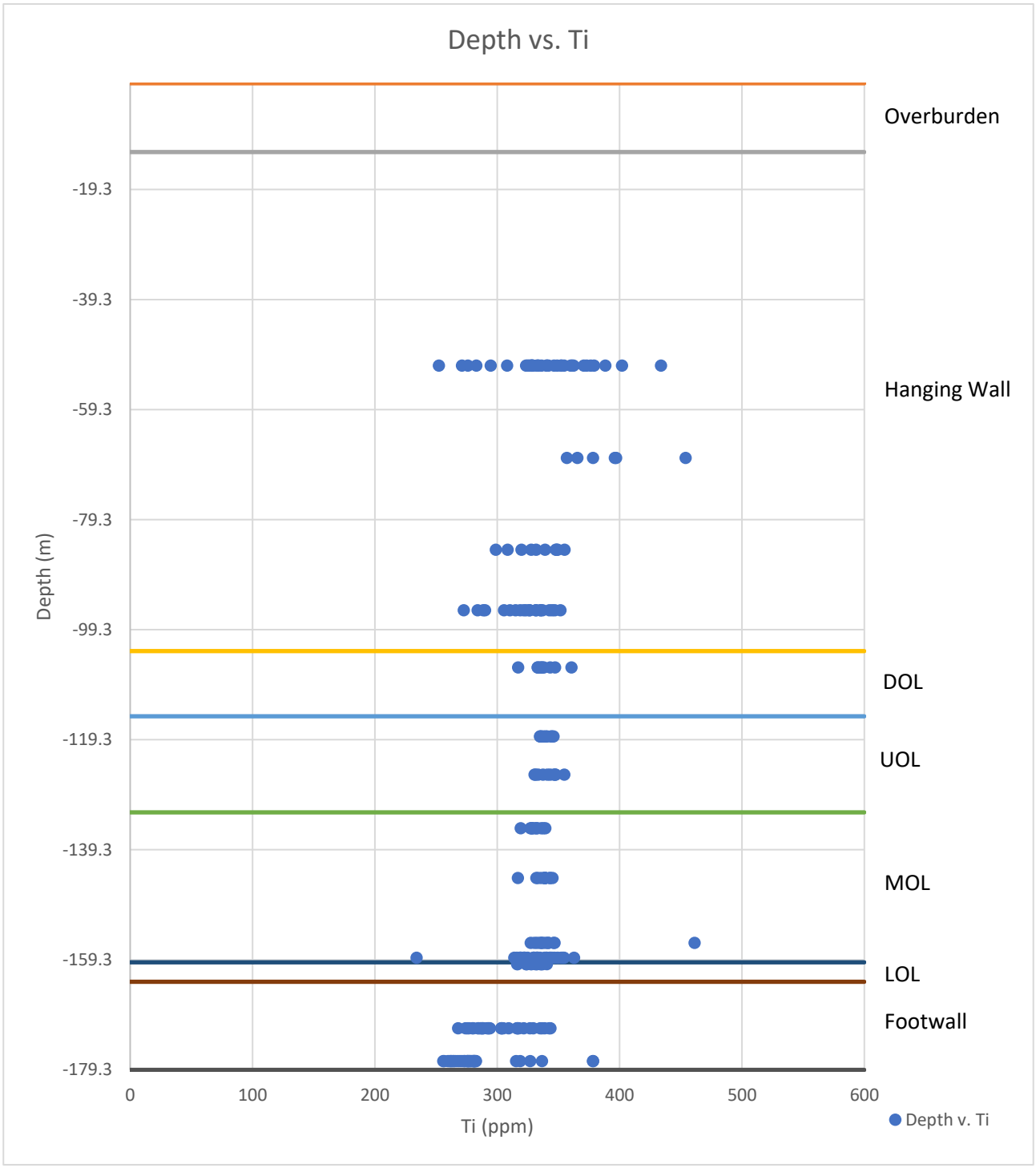

Figure 13: Depth vs. Ti of plagioclase from Mustavaara

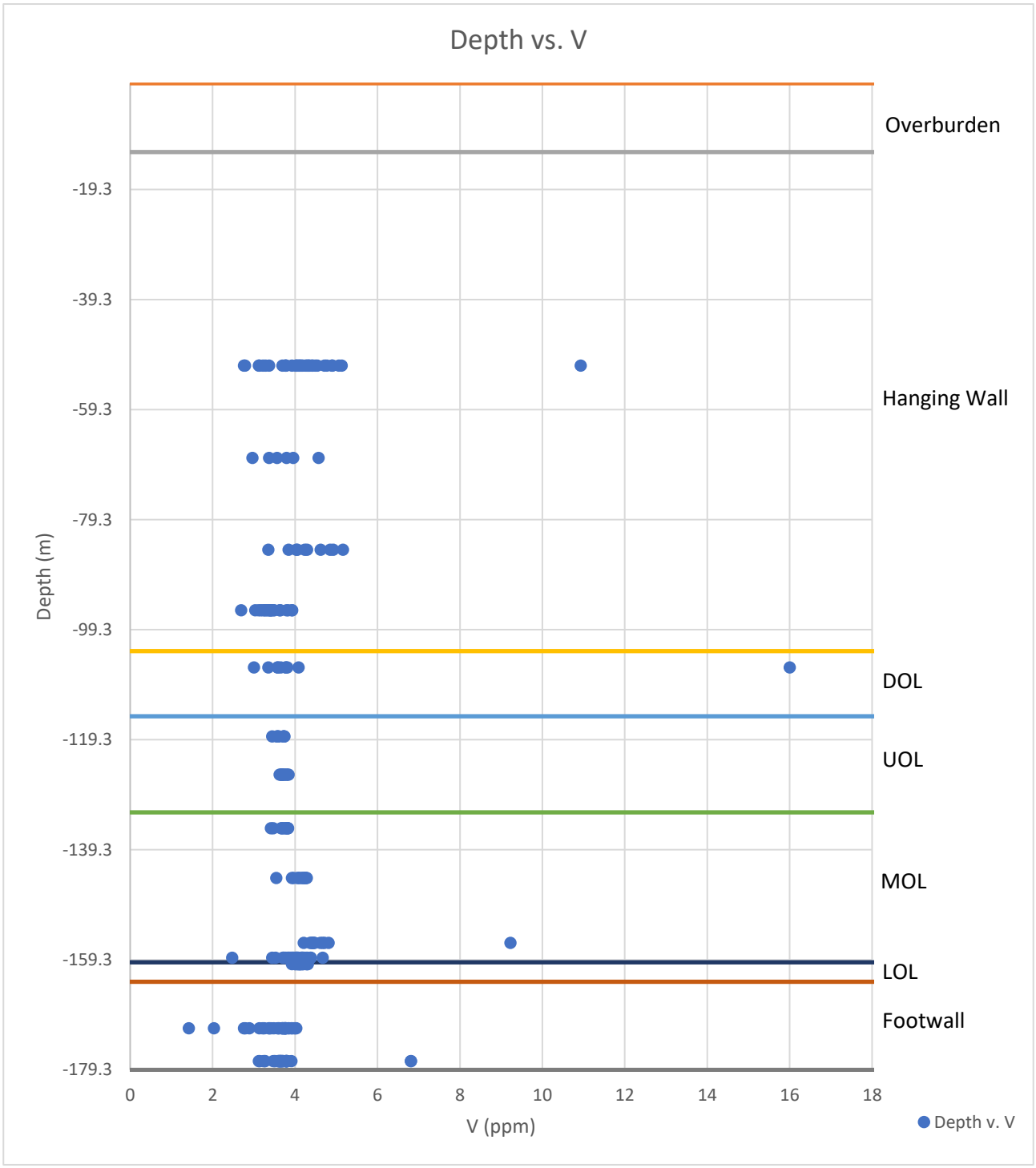

Figure 14: Depth vs. V of plagioclase from Mustavaara.

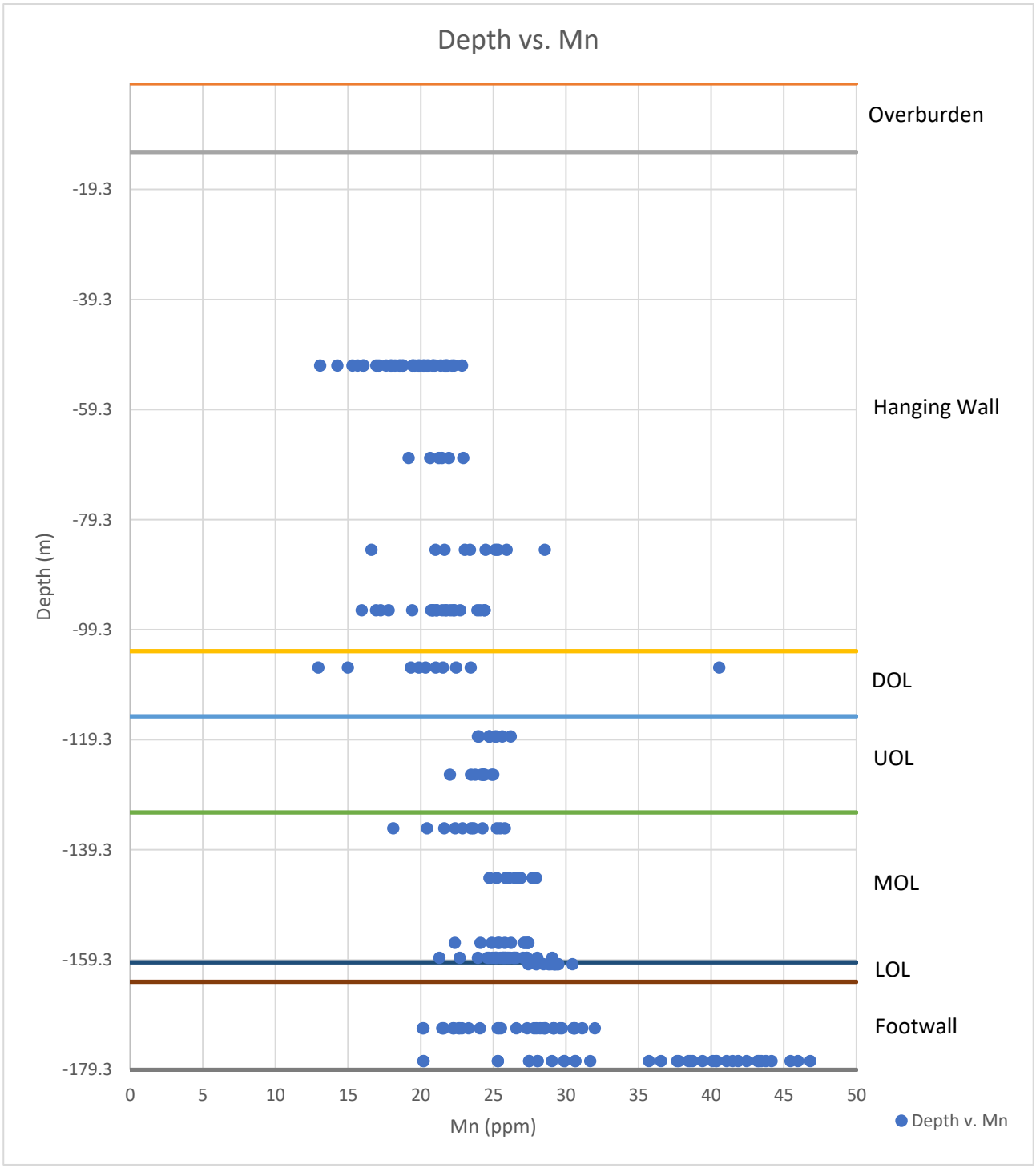

Figure 15: Depth vs. Mn of plagioclase from Mustavaara.

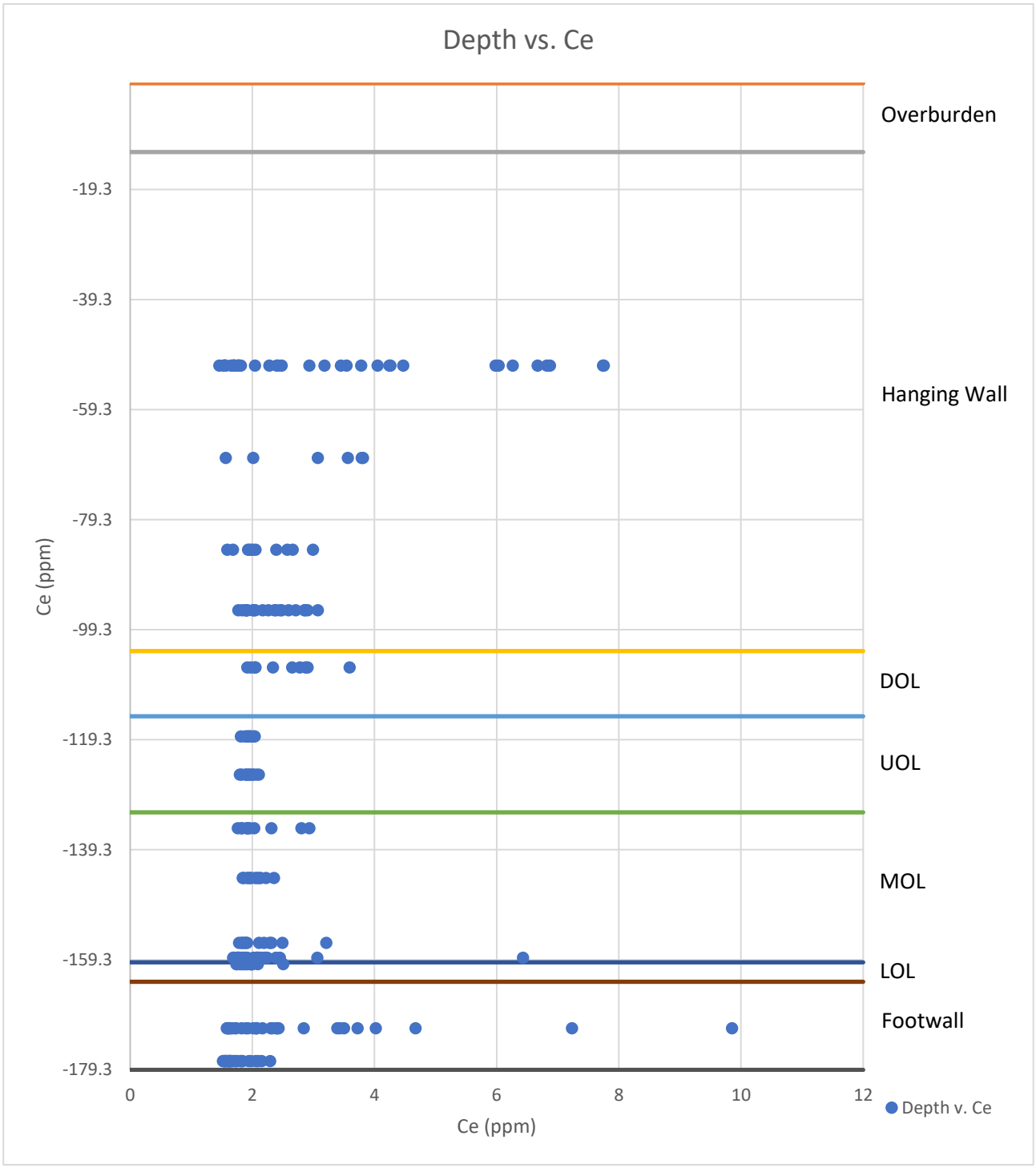

Figure 16: Depth vs. Ce of plagioclase from Mustavaara.

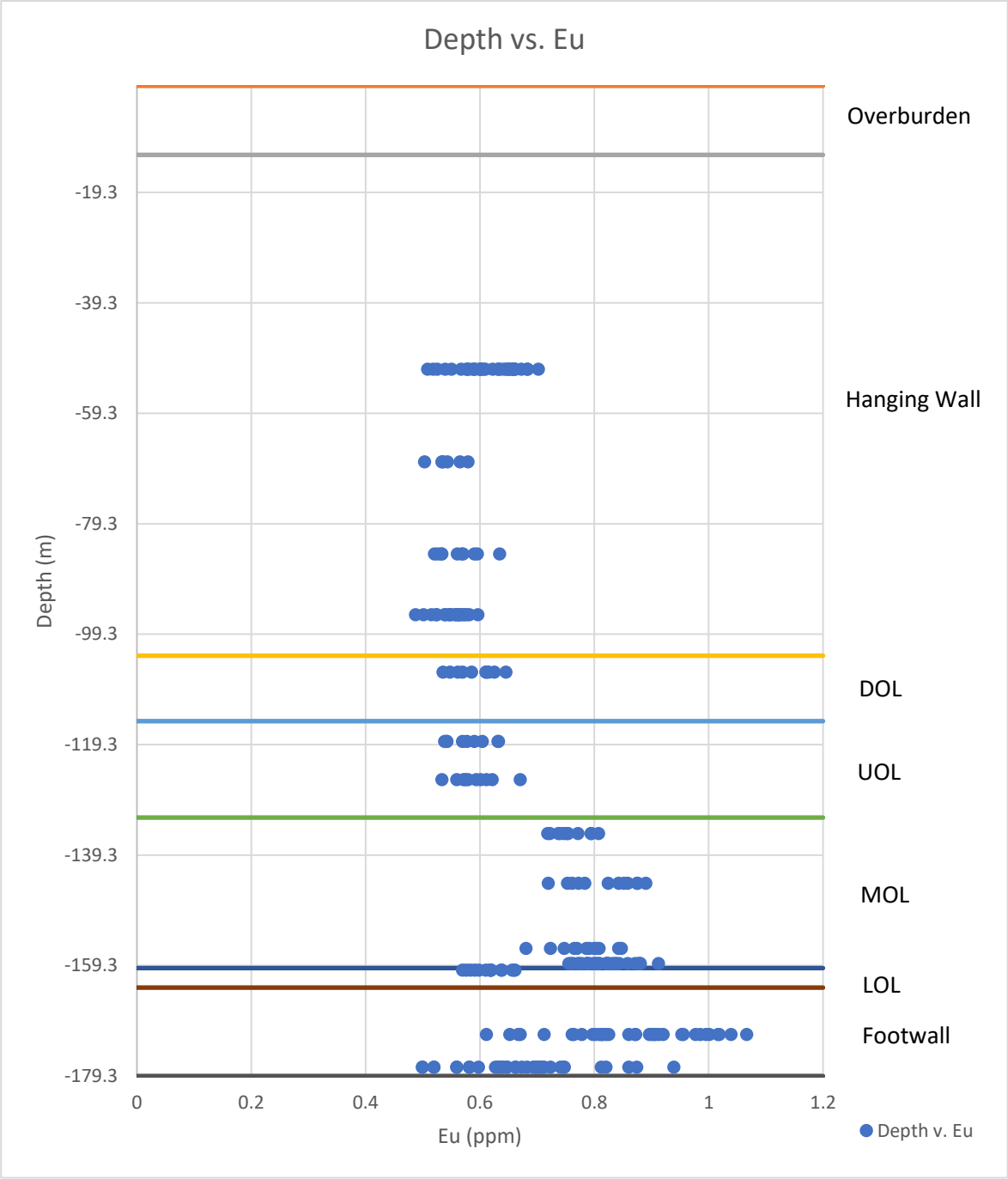

Figure 17: Depth vs. Eu of plagioclase from Mustavaara.

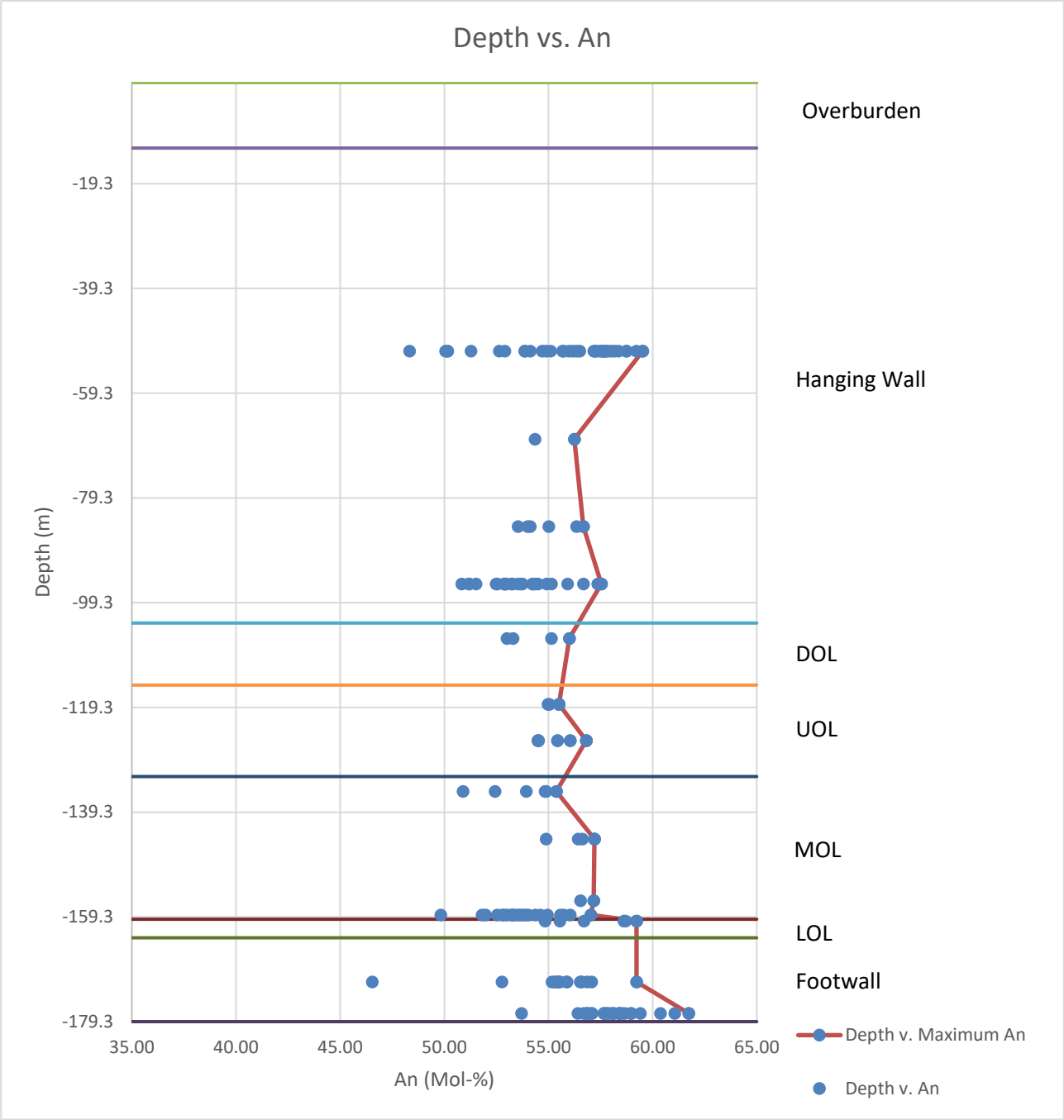

Figure 18: Depth vs. An of plagioclase from Mustavaara.

Each sample exhibits considerable variation of trace elements concentrations. This may partly due to the fractionation of trapped liquid, as evidenced by zoning of trace elements revealed by traverse analyses (i.e. Figure 20). It can be inferred that, for each sample, the highest content of compatible elements, and the lowest content of incompatible elements, may represent the primary mineral composition.

The Ti and V concentrations decrease from the hanging wall downwards, and from the footwall upwards, with low concentrations in the UOL at 119 m depth (Figures 13 and 14). There is a general increase in Mn concentrations from the hanging wall downwards, along with an outlying high concentration measured in the DOL (Figure 15). The Ce concentration increases from the hanging wall downwards, and from the footwall upwards (Figure 16). The Eu concentration also increases from the hanging wall downwards, and from the footwall upwards (Figure 17). Finally, the An decreases from the hanging wall downwards, and from the footwall upwards, with the lowest An occurring in the UOL and MOL (Figure 18). The trends of Ti and V correlate with the trend of An, while Ce shows the opposite trend.

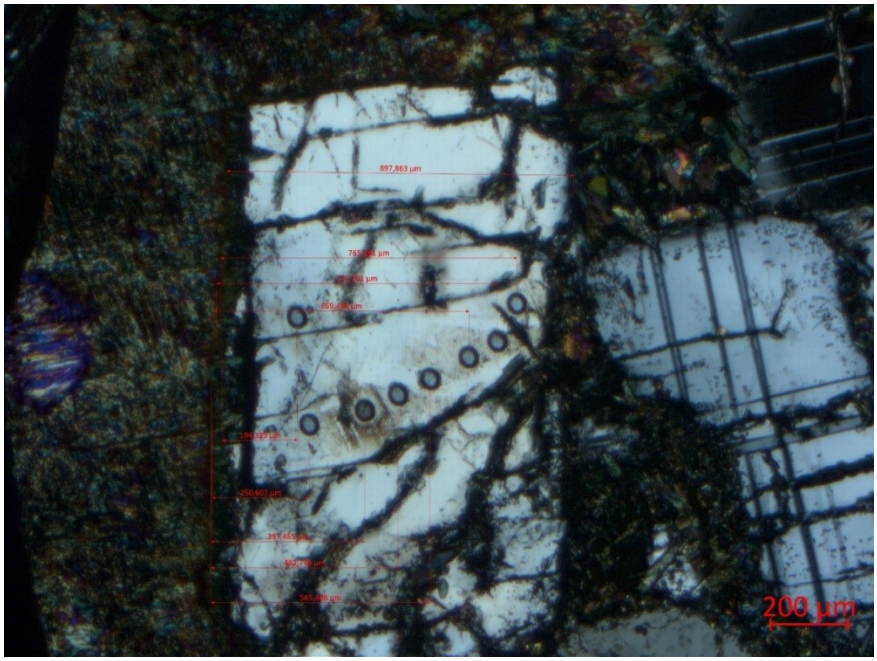

Figure 19: Thin Section 180185 Grain 1, Depth: -51.28 m, Spot traverse analyses in following image

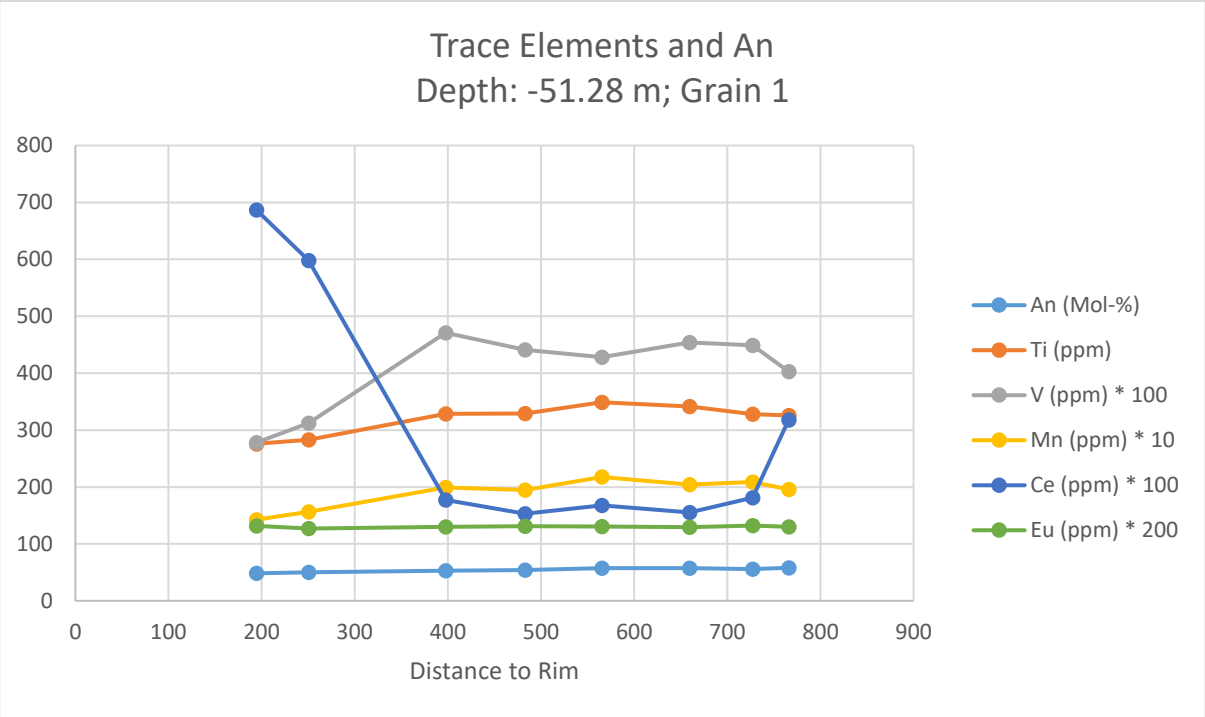

Figure 20: Spot traverse analysis, Depth: -51.28 m; Grain 1

The plotted data from a plagioclase grain in the hanging wall unit (depth: 51.28 m) shows a decreasing trend of Ti, V, and Mn from the core to the rim. The V data shows more prominent variation than that of Ti and Mn. The LREE data (i.e. Ce) shows a clear increasing trend from the core to the rim. The Eu and An data appear very consistent throughout the grain.

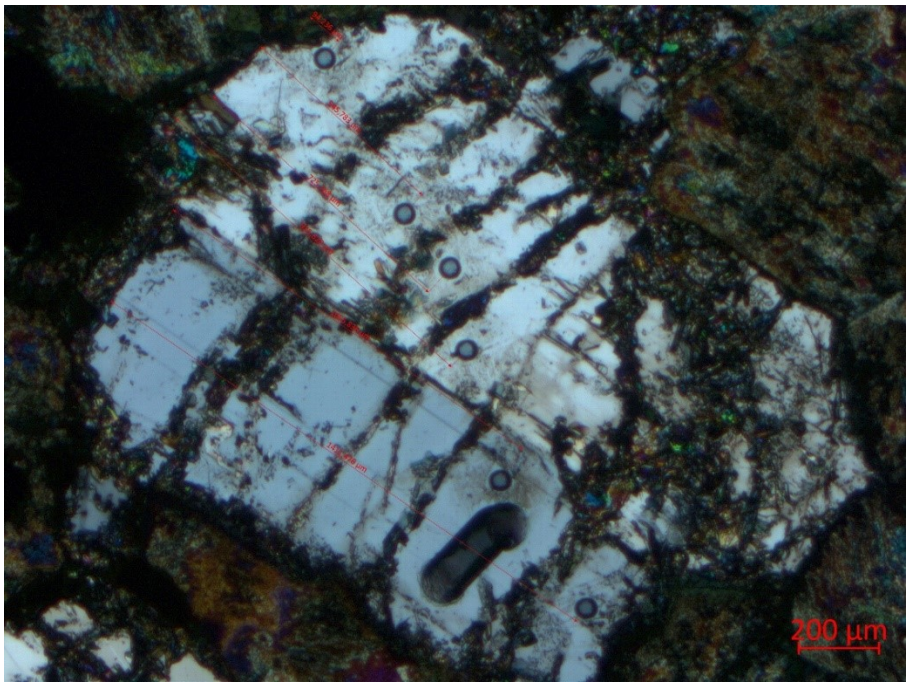

Figure 21: Thin Section 180192 Grain 2, Depth: -95.74 m, Spot traverse analyses in following image

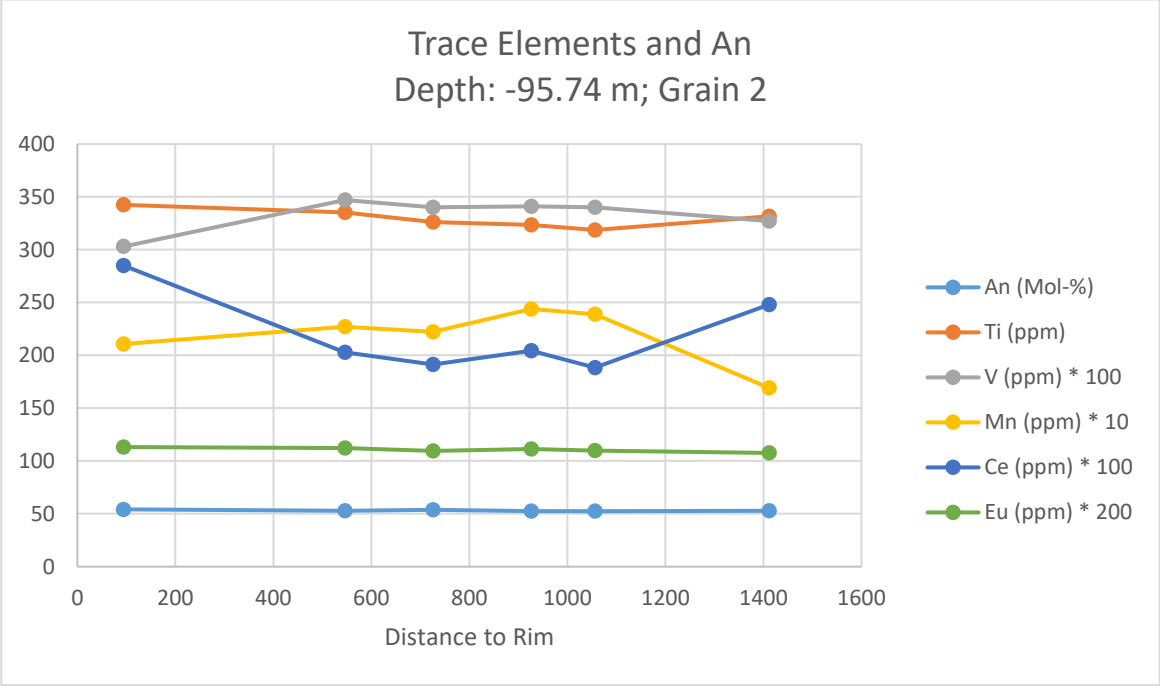

Figure 22: Spot traverse analysis, Depth: -95.74 m; Grain 2

Another plagioclase sample from the hanging wall unit (depth: 95.74 m) shows an increasing trend of Ti from the core to the rims. The V and Mn data both show a decreasing

trend from the core to the rims. The Ce data shows an increasing trend from the core to the rims. The Eu and An data show little variation.

Figure 23: Thin Section 180205 Grain 2, Depth: -158.90 m, Spot traverse analyses in following image

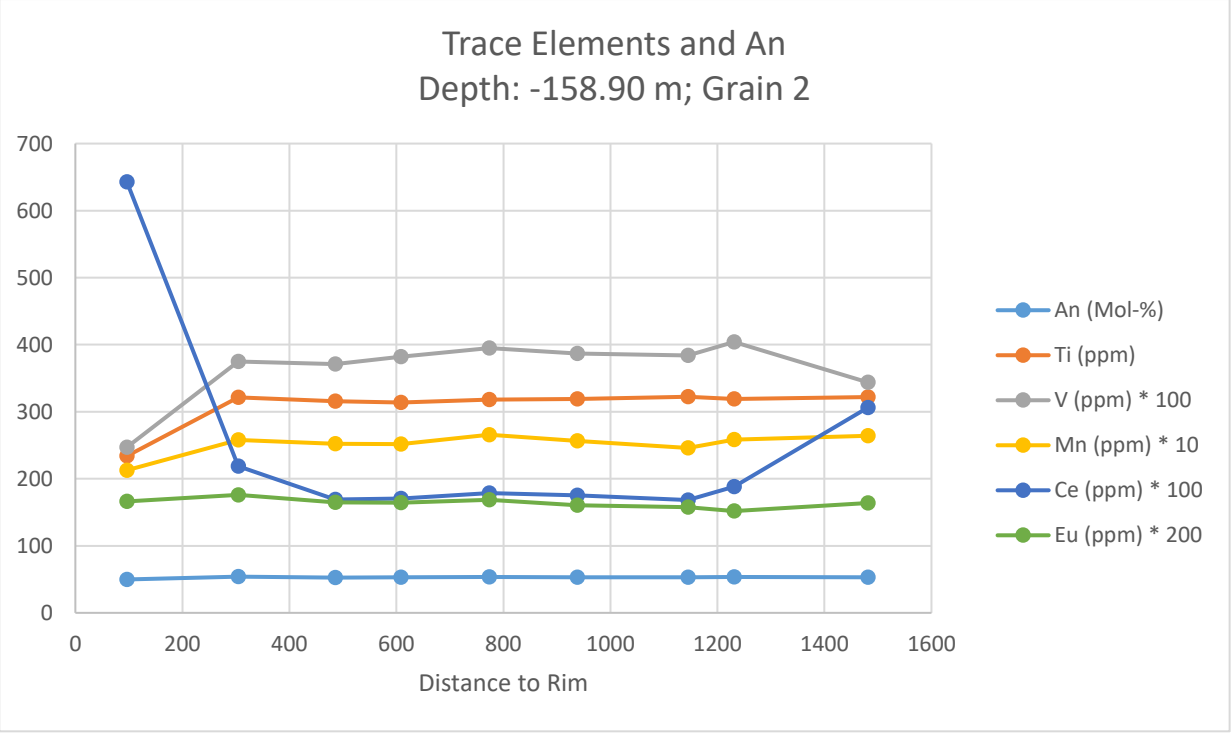

Figure 24: Spot traverse analysis, Depth: -158.90 m; Grain 2

A plagioclase sample from the MOL (depth: 158.90 m) shows a decreasing trend of Ti, V, and Mn from the core of the grain to the rims. This trend is particularly apparent in the V data. The Ce data shows an increasing trend from the core of the grain to the rims. The Eu and An data show little variation.

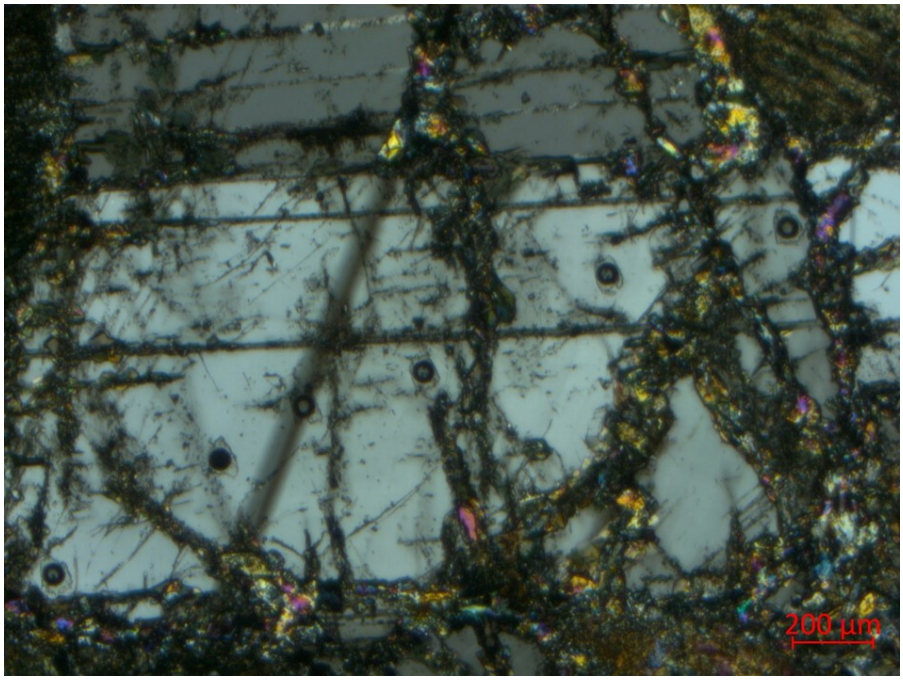

Figure 25: Thin Section 180210 Grain 2, Depth: -171.73 m, Spot traverse analyses in following image

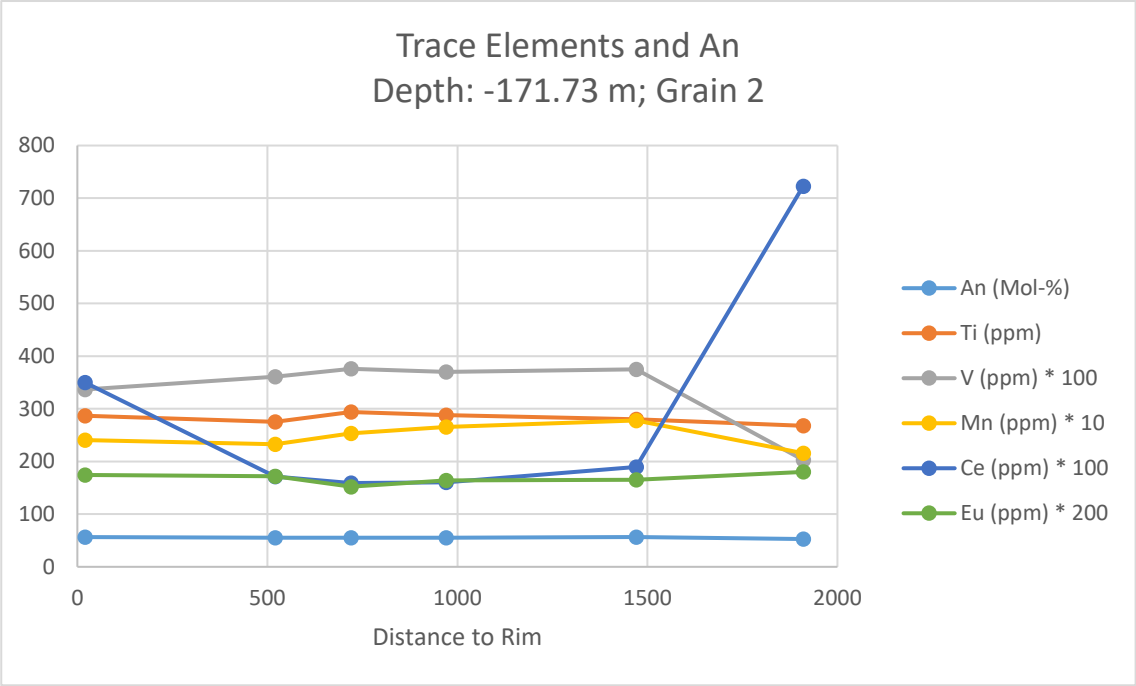

Figure 26: Spot traverse analysis, Depth: -171.73 m; Grain 2

A plagioclase sample from the footwall unit (depth: 171.73 m) shows a decreasing trend of Ti, V, and Mn from the core of the grain to the rims. This trend is more clear for V than for Ti or Mn. The Ce data shows an increasing trend from the core to the rims. The Eu and An data both show little variation.

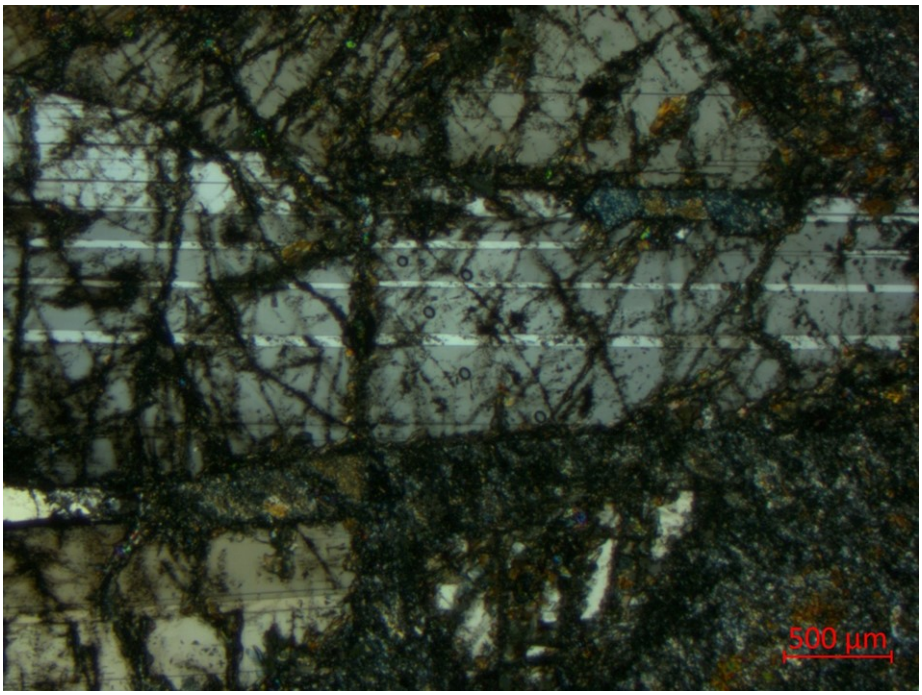

Figure 27: Thin Section 180211 Grain 3, Depth: -177.70 m, Spot traverse analyses in following image

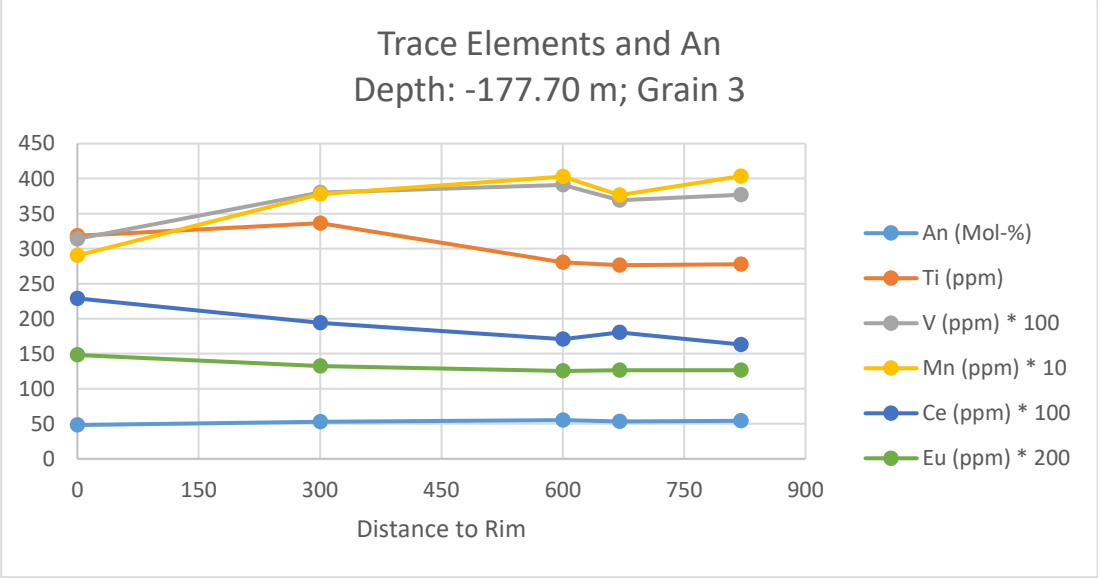

Figure 28: Spot traverse analysis, Depth: -177.70 m; Grain 3

Another plagioclase sample from the footwall unit (depth: 177.70 m) shows a decreasing trend of Ti, V, and Mn from the core to the rims. The Ti data shows a slightly different trend, due to the maximum Ti content occurring at a different point in the grain. The Ce data shows an increase from the core to one of the rims. The Eu data shows a similar (but less prominent) trend as the Ce data. The An data shows little variation.

Overall, most spot traverse analyses show that the rims of the plagioclase grains are depleted in Ti, V, and Mn, and enriched in Ce. The Eu and An data is generally consistent, with little variation.

The trace element data used to make plots is listed in Table 1. The results of moniter standard, which agree well with the reference values, is listed in Table 4 in the appendices.

Table 1: Trace element LA-HR-ICP-MS data

Sample	Ca	Ti	V	Mn	La	Ce	Pr	Nd	Sm	Sr	Eu	Distance
180185, Depth (51.28m), Hanging wall												
S1-1	71618.6	275.96	2.78	8.88	4.48	6.87	0.690	2.27	0.311	515.41	0.658	194.3
S1-2	73697.4	282.89	3.12	9.75	3.62	5.98	0.642	2.39	0.258	529.45	0.635	250.6
S1-3	79561.3	328.37	4.71	12.4	1.006	1.772	0.194	0.835	0.125	527.42	0.649	397.6
S1-4	78534.7	329.21	4.41	12.11	0.94	1.531	0.147	0.505	0.089	523.6	0.657	482.7
S1-5	84655.0	348.87	4.28	13.55	1.086	1.678	0.170	0.588	0.075	524.26	0.654	565.4
S1-6	83759.1	341.62	4.54	12.73	0.904	1.555	0.171	0.672	0.072	521.55	0.646	659.5
S1-7	86644.8	327.89	4.49	12.99	0.969	1.811	0.232	0.836	0.142	521.48	0.661	727.2
S1-8	87072.6	326.04	4.03	12.2	1.484	3.18	0.365	1.411	0.254	522.93	0.65	765.9
S2-1	77446.6	294.61	3.22	10.55	3.87	6.82	0.680	2.26	0.220	485.7	0.672	939.1
S2-2	82776.0	333.09	4.77	13.61	0.838	1.56	0.176	0.602	0.088	498.73	0.601	735.1
S2-3	79746.5	332.21	4.42	11.57	0.96	1.698	0.188	0.604	0.040	487.34	0.567	584.7
S2-4	75783.5	324.8	4.9	10	0.898	1.71	0.165	0.61	0.107	490.34	0.508	456.1
S2-5	79310.7	359.95	10.93	12.79	1.278	2.42	0.273	0.886	0.107	476.17	0.518	355.8
S2-6	82168.7	335.94	4.33	14.22	1.001	1.769	0.175	0.587	0.102	498.79	0.59	307.4
S2-7	79935.9	328.49	4.12	12.35	0.995	1.701	0.184	0.583	0.126	498.71	0.599	344.2
S2-8	79238.1	327.29	3.92	11.54	1.605	3.45	0.354	1.246	0.188	488.4	0.587	90.2
S3-1	68414.4	271	3.13	11.69	3.87	6.67	0.587	1.96	0.268	479.06	0.525	217.593
S3-2	80259.6	352.11	4.11	13.54	1.302	2.478	0.232	0.806	0.149	493.5	0.601	578.363
S3-3	73833.6	333.68	4.16	12.11	2.074	3.78	0.356	1.32	0.174	479.58	0.58	946.442
S3-4	81024.0	433.61	4.02	13.88	1.089	2.277	0.259	0.904	0.162	496.96	0.609	1587.874
S3-5	71780.9	323.37	3.37	11.16	3.66	6.03	0.527	1.436	0.162	483.28	0.622	1865.003
S3-6	68795.7	252.24	2.76	10.97	3.73	6.26	0.579	1.9	0.220	475.32	0.539	2203.792
S3-7	80969.1	352.08	4.08	13.79	0.952	1.77	0.197	0.628	0.098	490.12	0.576	2664.727
S3-8	80138.4	340.26	4.31	12.97	1.191	2.399	0.261	0.938	0.109	491.82	0.55	3232.499

Sample	Ca	Ti	V	Mn	La	Ce	Pr	Nd	Sm	Sr	Eu	Distance
180185, Depth (51.28m), Hanging wall (continued)												
S4	75087.6	362.23	4.05	15.29	0.886	1.651	0.178	0.659	0.129	508.83	0.606	N/A
S5	78630.0	340.36	3.69	20.17	2.47	4.26	0.422	1.381	0.135	509.22	0.601	N/A
S6	75558.0	376.26	3.78	18.75	1.146	2.04	0.224	0.75	0.152	513.9	0.682	N/A
S7	76914.8	346.39	5.06	16.03	1.545	2.93	0.281	1.001	0.122	516.22	0.642	N/A
S8	71425.2	307.86	3.77	13.07	4.79	7.75	0.761	2.2	0.260	516.69	0.631	N/A
S9	81796.7	360.89	3.76	21.37	2.168	4.47	0.479	1.672	0.244	525.44	0.658	N/A
S10	76407.5	370.55	4.9	17.98	1.901	4.05	0.430	1.528	0.310	519.61	0.661	N/A
S11	77120.3	388.25	4.25	20.23	1.859	3.54	0.408	1.29	0.163	530.75	0.683	N/A
S12	80454.2	379.02	4.35	21.64	2.3	4.24	0.422	1.454	0.180	541.17	0.702	N/A
S13	76579.7	354.5	4.18	20.96	0.883	1.459	0.155	0.558	0.118	535.38	0.632	N/A
S14	75667.7	401.78	5.13	18.23	0.852	1.54	0.166	0.662	0.096	528.39	0.591	N/A
S15	81363.1	372.94	3.28	17.11	4.54	7.74	0.704	2.38	0.248	521.68	0.578	N/A
180188, Depth (68.06m), Hanging wall												
S1	76516.3	378.15	3.95	21.94	2.18	3.79	0.350	1.111	0.125	551.83	0.565	N/A
S2	78696.7	396.93	3.37	21.25	1.627	3.07	0.314	1.059	0.105	536.87	0.533	N/A
S3	82980.5	453.85	3.56	20.65	1.848	3.56	0.376	1.072	0.151	538.88	0.543	N/A
S4	74332.5	365.28	3.79	19.16	2.32	3.81	0.374	1.133	0.193	530.05	0.579	N/A
S5	76457.6	395.95	4.57	22.92	1.077	2.01	0.203	0.756	0.117	528.47	0.503	N/A
S6	73315.6	356.86	2.96	21.46	0.929	1.563	0.169	0.473	0.061	516.89	0.535	N/A
180190, Depth (84.73m), Hanging wall												
S1	80238.6	354.96	4.03	28.54	0.854	1.588	0.179	0.623	0.077	591.28	0.52	N/A
S2	73825.1	319.61	4.92	25.12	1.553	2.66	0.259	0.927	0.113	577.5	0.595	N/A
S3	72989.3	308.34	4.85	21.63	1.33	2.39	0.229	0.831	0.118	596.7	0.59	N/A
S4	75267.2	331.66	3.35	23.03	1.108	1.93	0.172	0.717	0.090	584.72	0.533	N/A
S5	74633.5	298.67	3.84	25.9	1.17	2	0.206	0.784	0.096	584.06	0.568	N/A
S6	71518.6	347.71	4.62	16.6	1.801	2.99	0.269	0.898	0.152	577.86	0.526	N/A
S7	74886.8	338.96	4.05	24.46	1.015	1.68	0.191	0.654	0.122	580.8	0.56	N/A
S8	76693.2	348.37	4.23	25.31	1.086	1.96	0.209	0.704	0.104	584.1	0.532	N/A
S9	73157.8	327.63	4.29	21.01	1.153	2.05	0.225	0.573	0.139	581.7	0.57	N/A
S10	75333.2	349.29	5.16	23.38	1.492	2.57	0.263	0.872	0.120	576.84	0.634	N/A
180192, Depth (95.74m), Hanging wall												
S1-1	73732.4	326.33	3.16	13.14	1.673	2.59	0.256	0.788	0.104	544.04	0.501	132.4
S1-2	68998.7	288.53	3.64	9.92	1.161	2.003	0.202	0.638	0.099	523.61	0.487	375.1
S1-3	73402.2	272.57	3.42	13.9	1.387	2.451	0.248	0.812	0.095	533.09	0.577	499.3
S1-4	72029.1	305.45	3.79	13.37	1.419	2.386	0.220	0.822	0.118	537.86	0.573	666.3
S1-5	69630.8	283.91	3.93	10.73	1.278	2.169	0.207	0.751	0.102	538.2	0.524	790.4
S1-6	72749.8	289.83	3.92	12.97	1.093	1.896	0.191	0.675	0.091	535.35	0.523	943.7

Sample	Ca	Ti	V	Mn	La	Ce	Pr	Nd	Sm	Sr	Eu	Distance
180192, Depth (95.74m), Hanging wall (continued)												
S1-7	74112.2	314.81	3.49	13.73	1.061	1.77	0.211	0.667	0.093	548.34	0.561	1072.6
S2-1	76099.4	342.46	3.03	13.12	1.897	2.85	0.227	0.832	0.104	550.76	0.566	94.2
S2-2	72998.5	335.38	3.47	14.14	1.187	2.03	0.178	0.699	0.082	554.35	0.562	545.8
S2-3	73101.3	326.17	3.4	13.85	1.143	1.912	0.185	0.599	0.107	550.55	0.547	725.8
S2-4	74794.8	323.43	3.41	15.19	1.293	2.045	0.201	0.652	0.057	554.44	0.557	925.8
S2-5	74939.8	318.64	3.4	14.88	1.084	1.884	0.206	0.685	0.106	560.72	0.549	1055.8
S2-6	73521.5	331.73	3.27	10.54	1.65	2.48	0.235	0.755	0.127	561.21	0.538	1411.5
S3	73001.4	344.87	3.83	24.38	1.176	1.91	0.196	0.697	0.078	549.37	0.556	N/A
S4	67440.3	336.82	3.35	21.69	1.388	2.36	0.221	0.64	0.088	537.34	0.539	N/A
S5	74607.3	351.57	3.33	24.08	1.88	2.86	0.276	0.79	0.110	544.32	0.545	N/A
S6	72239.0	331.39	3.21	19.41	2.15	3.07	0.285	0.794	0.090	533.85	0.596	N/A
S7	75023.4	346.86	3.11	20.71	1.72	2.71	0.256	0.735	0.085	532.73	0.581	N/A
S8	74327.4	335.26	3.27	21.77	1.347	2.26	0.201	0.734	0.092	518.78	0.515	N/A
S9	73447.2	321.47	3.62	20.84	1.071	1.83	0.164	0.552	0.084	538.49	0.564	N/A
S10	67760.7	310.17	2.69	17.78	2.02	2.9	0.263	0.763	0.108	530.54	0.57	N/A
180193, Depth (106.14m), Disseminated ore layer												
S1	74464.4	332.89	3.81	23.43	1.18	1.916	0.171	0.636	0.119	548.2	0.611	N/A
S2	72031.3	347.17	3.78	19.32	1.397	2.337	0.229	0.698	0.094	547.36	0.547	N/A
S3	73496.5	343.16	3.65	21.52	1.266	1.973	0.194	0.609	0.081	546.26	0.585	N/A
S4	68851.8	317.04	4.08	12.95	1.883	2.9	0.285	0.877	0.092	535.38	0.535	N/A
S5	70472.5	333.14	3.77	14.98	1.998	2.87	0.270	0.844	0.122	547.09	0.569	N/A
S6	72979.5	337.94	3.35	20.32	1.859	2.776	0.264	0.86	0.096	553.24	0.615	N/A
S7	72847.3	335.06	3.57	22.43	1.278	2.037	0.194	0.659	0.077	552.19	0.625	N/A
S8	76777.3	360.49	3	19.86	2.314	3.59	0.303	0.926	0.091	555.63	0.61	N/A
S9	73058.8	335.74	3.58	21.04	1.697	2.652	0.238	0.771	0.056	541.46	0.645	N/A
S10	67630.4	336.8	16	40.54	1.274	2.05	0.173	0.784	0.082	546.8	0.561	N/A
180196, Depth (118.70m), Upper ore layer												
S1	73891.5	339.3	3.44	24	1.244	2.037	0.184	0.709	0.069	554.67	0.632	N/A
S2	73932.5	336.03	3.73	24.7	1.057	1.812	0.190	0.668	0.088	545.52	0.542	N/A
S3	75460.6	343.78	3.71	25.6	1.261	1.94	0.213	0.642	0.098	554.76	0.569	N/A
S4	74518.7	345.98	3.56	26.18	1.269	1.969	0.214	0.663	0.118	548.06	0.538	N/A
S5	73292.4	335.26	3.56	24.72	1.206	1.879	0.191	0.623	0.085	546.8	0.631	N/A
S6	73368.3	334.76	3.59	24.73	1.155	1.925	0.180	0.721	0.073	545.8	0.542	N/A
S7	74697.9	344.65	3.72	25.21	1.193	2.02	0.174	0.684	0.051	549.14	0.577	N/A
S8	74068.3	340.68	3.6	25.1	1.192	1.969	0.209	0.681	0.107	550.49	0.59	N/A
S9	72667.9	337.66	3.74	23.92	1.21	1.905	0.201	0.769	0.103	543.98	0.604	N/A

Sample	Ca	Ti	V	Mn	La	Ce	Pr	Nd	Sm	Sr	Eu	Distance
180198, Depth (125.63m), Upper ore layer												
S1	71101.6	333.23	3.66	24.27	1.114	1.9	0.193	0.58	0.077	536.28	0.579	N/A
S2	73767.0	330.37	3.84	24.89	1.181	1.943	0.202	0.656	0.057	537.45	0.601	N/A
S3	73749.5	337.24	3.79	23.74	1.126	1.892	0.176	0.614	0.091	542.53	0.574	N/A
S4	71529.0	331.3	3.62	23.45	1.122	1.792	0.163	0.703	0.027	536.18	0.559	N/A
S5	72333.7	340.94	3.8	24.29	1.101	1.822	0.167	0.589	0.102	538.48	0.533	N/A
S6	77299.2	347.49	3.69	22.01	1.236	2.063	0.215	0.705	0.140	574.6	0.611	N/A
S7	77274.2	347.16	3.73	24.41	1.211	2	0.202	0.577	0.058	566.53	0.571	N/A
S8	78382.5	346.21	3.73	24.16	1.342	2.105	0.211	0.722	0.111	573.94	0.593	N/A
S9	78036.8	354.78	3.66	24.99	1.223	2.012	0.196	0.714	0.090	577.62	0.67	N/A
S10	76902.7	343.2	3.68	24.3	1.257	1.947	0.219	0.596	0.157	573.95	0.621	N/A
180200, Depth (135.35m), Middle ore layer												
S1	74096.5	335.81	3.83	25.47	1.102	1.819	0.171	0.557	0.065	561.06	0.737	N/A
S2	72777.4	328.41	3.7	23.45	1.127	1.907	0.201	0.517	0.108	556.75	0.794	N/A
S3	71390.2	327.09	3.77	22.87	1.133	1.831	0.171	0.607	0.082	552.67	0.74	N/A
S4	73720.1	327.82	3.68	21.61	1.295	2.312	0.251	0.66	0.170	547.57	0.794	N/A
S5	71281.6	332.44	3.47	20.44	1.54	2.8	0.281	0.985	0.090	549.67	0.754	N/A
S6	72847.5	332.09	3.82	23.62	1.146	1.958	0.186	0.731	0.093	558.28	0.771	N/A
S7	72783.2	328.23	3.75	25.23	1.091	1.761	0.172	0.579	0.076	552.48	0.747	N/A
S8	74688.2	339.12	3.81	24.24	1.143	2.027	0.193	0.66	0.121	556.8	0.807	N/A
S9	71485.4	337.52	3.8	22.36	1.194	1.917	0.204	0.677	0.115	551.05	0.718	N/A
S10	69789.1	330.61	3.66	18.11	1.176	1.922	0.196	0.673	0.114	545.25	0.722	N/A
S11	74867.4	319.04	3.41	25.79	1.563	2.93	0.283	0.965	0.127	557.91	0.752	N/A
180202, Depth (144.40m), Middle ore layer												
S1	75851.9	335.67	3.54	25.9	1.29	2.132	0.221	0.822	0.074	585.24	0.875	N/A
S2	77102.1	339.32	3.92	26.87	1.246	2.073	0.203	0.766	0.083	585.12	0.875	N/A
S3	78575.1	343.25	4.08	27.68	1.214	2.05	0.192	0.72	0.129	587.14	0.858	N/A
S4	75763.2	338.76	4.12	24.72	1.279	2.114	0.234	0.708	0.103	574.14	0.89	N/A
S5	76702.5	342.78	4.26	26.49	1.207	1.985	0.195	0.621	0.092	581.6	0.772	N/A
S6	76870.0	332.92	4.05	25.86	1.257	2.223	0.206	0.809	0.114	580.55	0.842	N/A
S7	75856.1	339.01	4.2	27.85	1.111	1.852	0.188	0.677	0.104	547.88	0.719	N/A
S8	75396.8	338.53	4.28	27.93	1.078	1.839	0.194	0.656	0.111	551.85	0.761	N/A
S9	75560.3	344.97	4.25	26.58	1.102	1.957	0.201	0.669	0.094	566.13	0.783	N/A
S10	75023.7	338.46	4.2	25.21	1.174	1.91	0.211	0.638	0.081	543.13	0.852	N/A
S11	73589.3	331.79	4.17	26.04	1.148	1.935	0.186	0.665	0.072	551.07	0.824	N/A
S12	75135.0	316.72	3.96	26.82	1.409	2.35	0.235	0.879	0.113	557.51	0.753	N/A
180204, Depth (156.18m), Middle ore layer												
S1	76639.9	336.87	4.42	25.4	1.168	1.88	0.196	0.711	0.130	569.72	0.847	N/A
S2	75113.6	336.01	4.36	27.41	1.047	1.834	0.179	0.684	0.067	572.88	0.769	N/A
S3	74860.8	341.96	4.45	25.78	1.083	1.782	0.186	0.706	0.123	582.83	0.8	N/A

Sample	Ca	Ti	V	Mn	La	Ce	Pr	Nd	Sm	Sr	Eu	Distance
180204, Depth (156.18m), Middle ore layer (continued)												
S4	74341.8	346.64	4.47	24.88	1.254	2.19	0.208	0.695	0.088	563.87	0.804	N/A
S5	74208.2	335.23	4.43	24.1	1.398	2.49	0.236	0.847	0.129	569.53	0.808	N/A
S6	75197.5	330.33	4.21	26.2	1.405	2.28	0.221	0.809	0.104	556.83	0.791	N/A
S7	76416.4	345.78	4.81	25.31	1.195	2.11	0.226	0.735	0.118	562.62	0.842	N/A
S8	75615.5	341.28	4.71	27.16	1.119	1.89	0.190	0.643	0.108	571.05	0.765	N/A
S9	75325.9	332.66	4.67	27.1	1.113	1.91	0.187	0.664	0.100	549.91	0.723	N/A
S10	76701.8	327.25	4.39	27.32	1.359	2.31	0.231	0.838	0.113	557.19	0.786	N/A
S11	75676.8	339.43	4.61	27.39	1.102	1.83	0.192	0.751	0.129	558.39	0.68	N/A
S12	72800.2	461.07	9.22	22.34	1.741	3.21	0.318	1.164	0.123	554.25	0.747	N/A
180205, Depth (158.90m), Middle ore layer												
S1-1	76180.0	324.67	3.52	14.12	1.235	2.242	0.219	0.772	0.146	571.12	0.836	133.7
S1-2	77536.8	332.86	4.04	15.53	1.136	1.914	0.172	0.659	0.091	572.92	0.788	257.7
S1-3	74718.8	332.8	4.18	15.63	1.093	1.758	0.171	0.591	0.079	571.44	0.823	563.6
S1-4	78417.0	346.43	4.22	16.84	1.23	2.116	0.181	0.759	0.067	583.03	0.808	705.2
S1-5	75700.9	329.99	4.15	16.28	1.152	1.844	0.178	0.601	0.075	573.72	0.838	875.8
S1-6	74008.5	332.27	3.9	15.88	1.044	1.758	0.182	0.76	0.092	575.52	0.778	1065.7
S1-7	76987.1	329.56	3.78	15.38	1.244	2.097	0.232	0.758	0.067	579.97	0.771	1297
S2-1	67674.7	233.85	2.47	13.25	4.33	6.43	0.527	1.49	0.193	554.31	0.831	96.2
S2-2	75486.7	321.51	3.75	16.07	1.151	2.186	0.219	0.689	0.139	572.01	0.88	304.3
S2-3	72864.6	315.82	3.71	15.71	1.048	1.69	0.175	0.513	0.082	559.35	0.825	485.4
S2-4	73292.5	313.87	3.82	15.68	1.027	1.707	0.175	0.543	0.052	559.4	0.822	608.5
S2-5	74429.5	318.17	3.95	16.55	1.05	1.786	0.156	0.621	0.019	571.92	0.843	773.4
S2-6	72847.3	319.05	3.87	15.98	1.045	1.755	0.169	0.585	0.062	559.35	0.802	937.6
S2-7	73098.9	322.33	3.84	15.31	1.113	1.683	0.160	0.619	0.095	568.52	0.787	1145
S2-8	75027.3	318.97	4.04	16.1	1.036	1.88	0.181	0.645	0.039	569.67	0.759	1231.1
S2-9	75544.2	321.92	3.44	16.46	1.561	3.06	0.324	1.111	0.122	574.13	0.82	1481
S3	75539.5	331.8	3.93	25.17	1.144	2.076	0.207	0.717	0.094	564.53	0.803	N/A
S4	76668.2	343.28	4.01	26.43	1.271	2.141	0.196	0.654	0.096	587.49	0.791	N/A
S5	76221.9	334.87	4.02	23.93	1.149	2.071	0.205	0.775	0.065	574.81	0.755	N/A
S6	75998.2	338.64	4.07	26.37	1.099	1.891	0.187	0.627	0.127	583.27	0.773	N/A
S7	75990.4	329.78	3.97	25.7	1.227	2.213	0.206	0.865	0.128	578.35	0.822	N/A
S8	78330.1	340.09	4.15	25.65	1.349	2.385	0.222	0.994	0.165	587.2	0.858	N/A
S9	78648.1	342.77	4.18	26.03	1.292	2.216	0.227	0.719	0.074	591.96	0.912	N/A
S10	76748.3	362.63	4.38	28.02	1.124	1.798	0.174	0.596	0.062	593.01	0.787	N/A
S11	78456.0	352.26	4.37	29.04	1.145	1.851	0.189	0.727	0.096	589.66	0.808	N/A
S12	76705.0	353.48	4.3	27.29	1.064	1.772	0.173	0.55	0.104	596.93	0.798	N/A
S13	76210.5	354.52	4.67	27.32	1.152	2.066	0.194	0.764	0.059	593.26	0.763	N/A
S14	76860.7	349.27	4.07	25.96	1.178	2.015	0.192	0.799	0.092	592.3	0.877	N/A

Sample	Ca	Ti	V	Mn	La	Ce	Pr	Nd	Sm	Sr	Eu	Distance
180205, Depth (158.90m), Middle ore layer (continued)												
S15	76810.3	344.61	4.27	26.53	1.184	2.088	0.208	0.735	0.099	579.49	0.871	N/A
S16	75665.3	340.28	3.71	25.79	1.367	2.45	0.244	0.845	0.142	570.08	0.879	N/A
180206, Depth (160.08m), Lower ore layer												
S1	75973.0	330.98	4.06	28.45	1.207	2.087	0.214	0.757	0.115	556.71	0.583	N/A
S2	75398.0	335.32	4.01	28.86	1.142	1.853	0.190	0.634	0.101	554.41	0.576	N/A
S3	76255.8	340.52	4.27	29.47	1.019	1.805	0.198	0.674	0.073	564.55	0.656	N/A
S4	77168.0	335.34	4.15	30.45	1.064	1.853	0.176	0.734	0.111	563.01	0.598	N/A
S5	74923.0	332.24	4.29	29.33	1.007	1.738	0.168	0.605	0.081	572.21	0.618	N/A
S6	75822.8	336.94	4	27.4	1.16	1.98	0.228	0.695	0.111	557.85	0.591	N/A
S7	76117.0	331.96	4.19	29.16	1.104	1.892	0.175	0.693	0.087	568.02	0.637	N/A
S8	75016.6	327.7	3.92	28.8	1.147	1.99	0.205	0.691	0.121	556.55	0.61	N/A
S9	78139.5	336.38	4.12	29.28	1.483	2.503	0.254	0.687	0.060	556.34	0.661	N/A
S10	72934.3	316.51	4.08	29.19	1.118	1.963	0.193	0.694	0.077	540.82	0.618	N/A
S11	75213.8	324.16	4.31	29.23	1.063	1.739	0.168	0.628	0.121	552.5	0.638	N/A
S12	73566.0	323.57	4.12	27.98	1.024	1.795	0.188	0.577	0.105	543.3	0.619	N/A
S13	73998.0	323.44	4.07	28.97	1.148	1.914	0.198	0.702	0.114	543.63	0.569	N/A
S14	75525.4	327.72	4.12	27.93	1.114	2	0.189	0.677	0.064	560.18	0.618	N/A
S15	74514.0	316.04	4.19	29.43	1.095	1.979	0.213	0.673	0.116	551.95	0.659	N/A
180210, Depth (171.73m), Footwall												
S1-1	75323.9	336.35	2.76	21.53	2.018	3.72	0.420	1.496	0.217	567.76	1.018	50
S1-2	78284.7	338.55	3.25	22.68	1.418	2.41	0.236	0.841	0.132	578.96	0.985	270
S1-3	84657.0	309.25	3.77	29.12	1.201	2.067	0.209	0.763	0.085	577.85	0.92	500
S1-4	83405.3	303.65	3.97	29.59	1.129	1.924	0.199	0.781	0.110	572.93	0.904	700
S1-5	82425.6	303.2	4	31.11	1.129	1.824	0.208	0.643	0.095	569.99	0.907	940
S1-6	82600.9	316.59	3.91	29.72	1.267	2.056	0.225	0.742	0.075	567.12	0.896	1260
S1-7	78462.6	343.45	3.57	27.31	1.276	2.165	0.194	0.747	0.098	571.03	0.913	1460
S1-8	74988.2	334.95	2.79	21.47	1.936	3.43	0.387	1.345	0.215	566.34	0.995	1510
S2-1	78976.0	286.63	3.37	24.07	1.846	3.5	0.355	1.301	0.174	535.22	0.871	20
S2-2	73883.1	275.48	3.61	23.29	0.979	1.716	0.183	0.594	0.086	529.61	0.86	520
S2-3	75239.7	293.95	3.76	25.37	0.876	1.591	0.175	0.623	0.031	538.65	0.761	720
S2-4	75990.9	287.91	3.7	26.57	0.915	1.606	0.156	0.492	0.092	540.96	0.82	970
S2-5	75135.7	280.23	3.75	27.79	1.007	1.899	0.172	0.678	0.070	526.12	0.825	1470
S2-6	70157.6	267.84	2.03	21.58	4.42	7.23	0.636	2.09	0.269	529.07	0.901	1910
S3-1	79463.9	315.9	3.21	22.22	1.929	3.39	0.348	1.337	0.183	567.51	0.953	100
S3-2	80022.6	317.59	3.69	25.28	1.425	2.39	0.251	1.024	0.154	567.69	1.016	200
S3-3	81373.6	326.6	4.03	25.52	1.305	2.3	0.232	0.896	0.129	577.06	1.066	400
S3-4	80083.3	321.6	3.68	22.27	1.368	2.32	0.247	0.922	0.151	569.21	1.001	650
S3-5	80836.6	316.44	3.13	22.83	2.14	4.02	0.428	1.426	0.259	575.51	1.039	750

Sample	Ca	Ti	V	Mn	La	Ce	Pr	Nd	Sm	Sr	Eu	Distance
180210, Depth (171.73m), Footwall (continued)												
S3-6	64502.0	273.99	1.42	20.19	6.75	9.85	0.850	2.65	0.291	539.35	0.977	830
S4	78215.0	342.31	3.92	28.46	1.22	2.061	0.228	0.661	0.103	555.07	0.797	N/A
S5	75749.8	284.57	3.84	22.61	0.943	1.666	0.161	0.62	0.087	528.87	0.712	N/A
S6	76414.2	288.35	3.78	27.95	0.896	1.58	0.157	0.57	0.092	527.98	0.611	N/A
S7	79967.4	291.58	3.48	29.15	1.278	2.427	0.219	1.071	0.118	534.34	0.652	N/A
S8	80513.3	303.31	3.69	29.17	1.15	2.011	0.214	0.761	0.122	537.43	0.667	N/A
S9	79379.2	304.82	3.37	28.22	1.323	2.394	0.241	0.894	0.108	531.3	0.67	N/A
S10	75087.7	329.33	3.6	28.55	1.291	2.064	0.219	0.723	0.128	538.63	0.814	N/A
S11	77337.2	286.44	3.84	30.52	0.988	1.627	0.195	0.572	0.074	542.64	0.872	N/A
S12	76780.6	279.71	3.76	30.58	0.917	1.591	0.165	0.531	0.090	531.95	0.764	N/A
S13	75509.7	276.71	3.73	30.62	0.962	1.616	0.135	0.509	0.056	531.86	0.809	N/A
S14	73614.6	292.98	2.89	20.13	2.272	4.67	0.464	1.51	0.235	526.75	0.813	N/A
S15	75914.0	284.17	3.41	28.56	1.618	2.84	0.293	0.986	0.198	532.87	0.955	N/A
S16	78017.6	287.88	3.73	31.98	0.999	1.647	0.160	0.583	0.069	537.47	0.802	N/A
S17	77207.1	292.34	3.76	30.54	0.91	1.732	0.180	0.571	0.081	534.06	0.778	N/A
180211, Depth (177.70m), Footwall												
S1-1	71665.7	318.62	3.14	29.03	1.394	2.29	0.231	0.818	0.111	503.82	0.741	0
S1-2	76979.6	336.4	3.8	37.76	1.13	1.94	0.204	0.667	0.161	515.37	0.662	300
S1-3	80794.2	280.63	3.91	40.29	0.886	1.71	0.192	0.616	0.102	524.37	0.627	600
S1-4	78448.8	276.38	3.69	37.65	0.975	1.804	0.162	0.662	0.060	513.08	0.633	670
S1-5	80376.8	277.87	3.77	40.36	1.009	1.632	0.164	0.556	0.124	516.23	0.632	820
S2-1	77422.4	282.37	3.78	27.46	0.962	1.607	0.166	0.559	0.072	507.14	0.707	70
S2-2	78145.4	281.38	3.79	25.31	0.994	1.736	0.202	0.672	0.067	505.51	0.701	150
S2-3	74853.7	280.76	3.64	28.04	0.908	1.541	0.151	0.612	0.093	500.06	0.581	300
S2-4	76648.9	273.44	3.66	29.87	0.905	1.56	0.144	0.48	0.073	504.37	0.499	700
S2-5	79822.7	275.71	3.8	30.64	0.91	1.623	0.159	0.51	0.097	502.57	0.519	750
S2-6	70258.2	378.22	6.81	20.19	1.03	1.82	0.192	0.613	0.093	499.81	0.559	900
S3-1	74468.4	262.19	3.27	22.24	1.033	1.838	0.177	0.738	0.073	534.44	0.939	278.9
S3-2	76383.1	264.37	3.6	24.98	0.93	1.749	0.153	0.683	0.085	522.77	0.747	477.9
S3-3	77635.3	267.64	3.71	26.43	0.885	1.624	0.153	0.631	0.094	536.92	0.647	715.7
S3-4	78989.6	270.84	3.68	27.06	0.896	1.662	0.154	0.481	0.081	541.1	0.673	844.5
S3-5	78952.7	272.39	3.71	26.96	0.949	1.627	0.159	0.55	0.143	553.87	0.693	1071
S3-6	83574.1	264.02	3.77	26.9	1.085	1.969	0.188	0.801	0.087	537.33	0.86	1421.9
S3-7	74738.3	277.24	3.61	28.31	1.25	2.072	0.193	0.78	0.108	538.55	0.874	1629.8
S4-1	79727.4	279.09	3.26	24.11	1.125	2.048	0.197	0.687	0.083	555.89	0.812	1496.2
S4-2	77426.7	256.33	3.57	24.01	0.903	1.579	0.153	0.548	0.068	539.93	0.662	1284.7
S4-3	77908.5	261.17	3.47	26.06	0.919	1.573	0.125	0.633	0.075	535.17	0.695	889.9

Sample	Ca	Ti	V	Mn	La	Ce	Pr	Nd	Sm	Sr	Eu	Distance
180211, Depth (177.70m), Footwall (continued)												
S4-4	76515.2	255.85	3.65	25.82	0.856	1.531	0.146	0.57	0.066	525.47	0.64	676.7
S4-5	79245.0	262.16	3.6	25.57	0.9	1.664	0.162	0.573	0.034	539.16	0.682	586.9
S4-6	80695.4	265.9	3.62	24.54	0.963	1.693	0.165	0.589	0.056	551.36	0.747	384
S4-7	77534.6	259.71	3.5	22.75	0.891	1.645	0.152	0.579	0.065	537.49	0.82	255.7
S5	78688.6	279.69	3.64	44.14	0.97	1.615	0.144	0.554	0.075	523.97	0.647	N/A
S6	77728.3	277.2	3.69	45.97	0.911	1.528	0.157	0.469	0.086	531.11	0.698	N/A
S7	77232.6	269.31	3.51	46.81	0.871	1.565	0.156	0.489	0.069	515.94	0.723	N/A
S8	78934.7	275.29	3.61	43.76	0.928	1.517	0.149	0.542	0.079	519.53	0.597	N/A
S9	70190.4	315.26	3.23	31.66	1.225	2.09	0.224	0.63	0.113	509.55	0.638	N/A
S10	73011.0	326.85	3.12	38.42	1.236	2.15	0.205	0.718	0.117	512.94	0.712	N/A

5.2 Rb-Sr isotope composition of plagioclase

Rb-Sr isotope composition of plagioclase is analyzed in-situ using LA-MC-ICP-MS at GTK. The initial $^{87}Sr/^{86}Sr$ is calculated back to 2.44 Ga ago. The initial $^{87}Sr/^{86}Sr$ of spot analyses, average initial $^{87}Sr/^{86}Sr$ of each sample, and $^{87}Rb/^{87}Sr$ ratios against depth are plotted below. In addition, the data from each line analysis is given in Table 2. The data from each standard measurement is given in tables 5 and 6 in the appendices.

There is some variation of initial $^{87}Sr/^{86}Sr$ within sample scale, due to analytical uncertainty (Figure 29). The average values are relatively uniform at about 0.7030 throughout the stratigraphy (Figure 30). It can be noted that there is a particular increase in the $^{87}Rb/^{87}Sr$ ratio from UOL to the MOL, and from the footwall to the MOL.

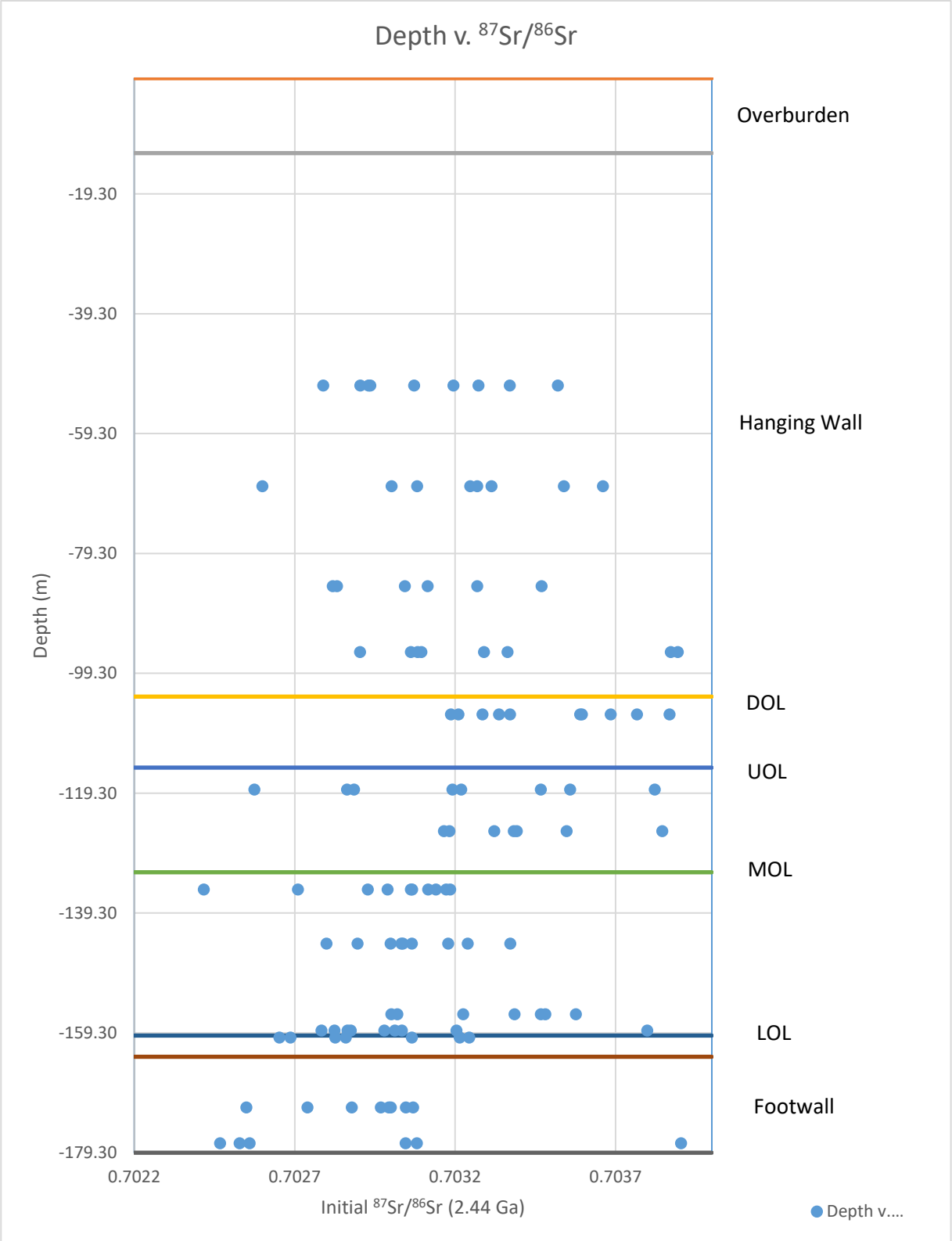

Figure 29: Depth vs. initial $^{87}Sr/^{86}Sr$ (2.44 Ga)

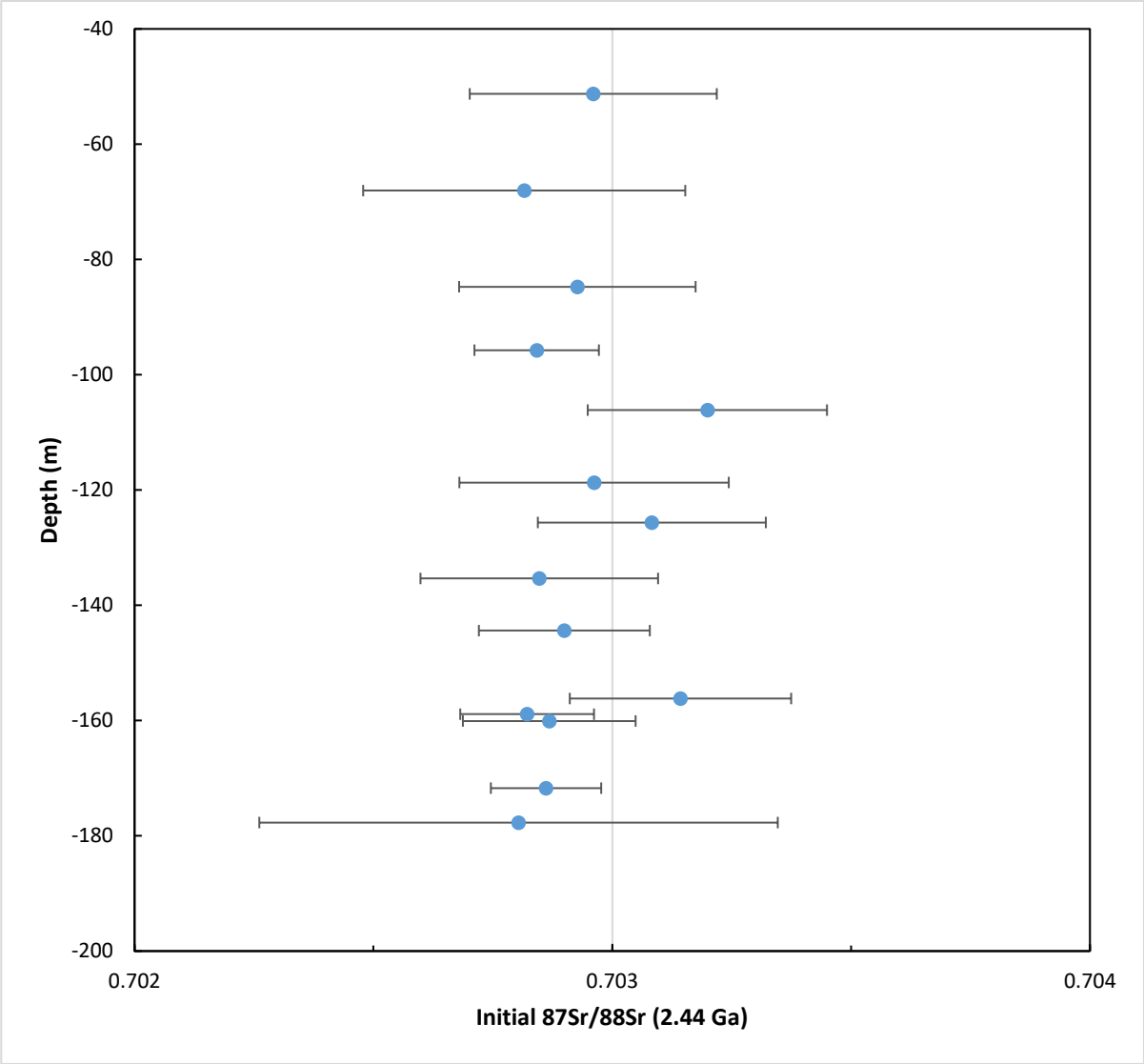

Figure 30: Depth vs. Average initial $^{87}Sr/^{86}Sr$ (2.44 Ga)

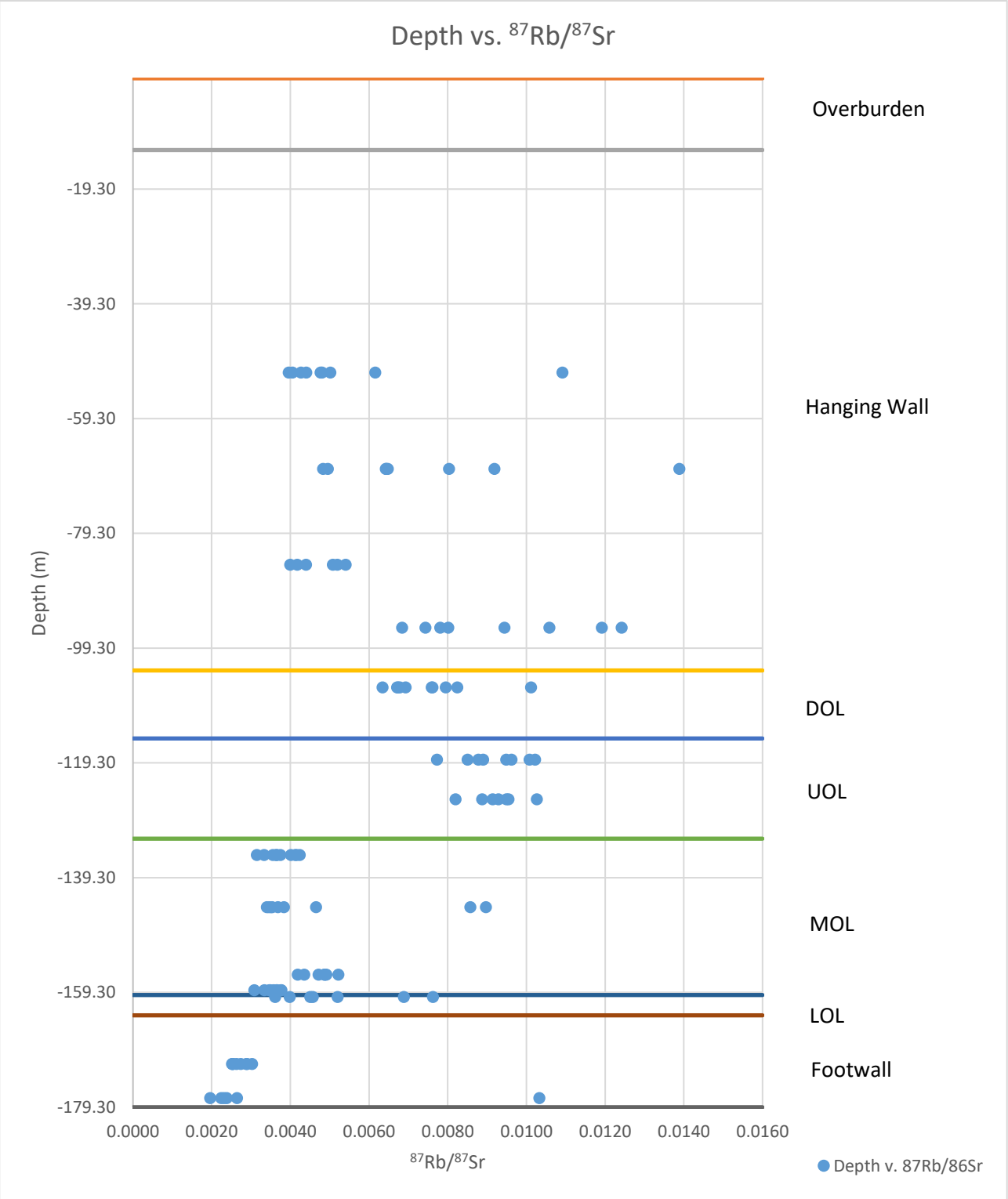

Figure 31: Depth vs. $^{87}Rb/^{87}Sr$

Table 2. In-situ Rb-Sr isotope composition of plagioclase

Sample	Rb (V)	Sr (V)	87Rb/86Sr	87Sr/86Sr	1σ	87Sr/86Sr I (2.44 Ga)
180185, depth (51.28m), Hanging wall						
L1	0.0005	0.3794	0.0040	0.7028	6.91E-05	0.7026
L2	0.0007	0.3890	0.0048	0.7029	5.84E-05	0.7028
L3	0.0008	0.4082	0.0050	0.7031	5.73E-05	0.7029
L4	0.0007	0.3778	0.0048	0.7035	6.53E-05	0.7034
L5	0.0013	0.3745	0.0109	0.7029	6.65E-05	0.7025
L6	0.0006	0.3771	0.0043	0.7029	5.96E-05	0.7028
L7	0.0006	0.3455	0.0044	0.7032	7.13E-05	0.7030
L8	0.0005	0.3253	0.0041	0.7034	8.92E-05	0.7032
180188, depth (68.06m), Hanging wall						
L1	0.0008	0.3340	0.0064	0.7035	0.0001	0.7033
L2	0.0009	0.3774	0.0065	0.7037	0.0001	0.7034
L3	0.0007	0.3879	0.0048	0.7031	0.0001	0.7029
L4	0.0008	0.4201	0.0049	0.7033	0.0001	0.7031
L5	0.0016	0.3572	0.0139	0.7033	0.0001	0.7028
L6	0.0011	0.3674	0.0080	0.7030	0.0001	0.7027
L7	0.0010	0.3347	0.0092	0.7026	0.0001	0.7023
L8	0.0009	0.3738	0.0064	0.7032	0.0001	0.7030
180190, depth (84.73m), Hanging wall						
L1	0.0006	0.3846	0.0044	0.7030	0.0000	0.7029
L2	0.0006	0.4121	0.0042	0.7028	0.0001	0.7027
L3	0.0008	0.4058	0.0051	0.7033	0.0001	0.7031
L4	0.0007	0.3414	0.0054	0.7028	0.0001	0.7026
L5	0.0006	0.3904	0.0040	0.7031	0.0001	0.7030
L6	0.0007	0.3580	0.0052	0.7035	0.0001	0.7033
180192, depth (95.74m), Hanging wall						
L1	0.0012	0.3201	0.0124	0.7039	0.0001	0.7035
L2	0.0014	0.3236	0.0119	0.7039	0.0001	0.7035
L3	0.0010	0.3318	0.0080	0.7031	0.0001	0.7028
L4	0.0013	0.3268	0.0106	0.7034	0.0001	0.7030
L5	0.0007	0.2777	0.0068	0.7031	0.0001	0.7029
L6	0.0009	0.3206	0.0074	0.7031	0.0001	0.7028
L7	0.0011	0.3150	0.0094	0.7033	0.0001	0.7030
L8	0.0009	0.3131	0.0078	0.7029	0.0001	0.7026
180193, depth (106.14m), DOL						
L1	0.0012	0.3207	0.0101	0.7033	0.0001	0.7029
L2	0.0008	0.2721	0.0082	0.7034	0.0001	0.7031
L3	0.0006	0.2466	0.0067	0.7036	0.0001	0.7034
L4	0.0007	0.2443	0.0076	0.7032	0.0002	0.7029
L5	0.0006	0.2280	0.0076	0.7039	0.0001	0.7036
L6	0.0006	0.2430	0.0063	0.7037	0.0001	0.7035
L7	0.0006	0.2343	0.0067	0.7032	0.0001	0.7030
L8	0.0007	0.2428	0.0079	0.7038	0.0001	0.7035
L9	0.0007	0.2864	0.0068	0.7033	0.0001	0.7031
L10	0.0007	0.2760	0.0069	0.7036	0.0001	0.7034

Sample	Rb (V)	Sr (V)	87Rb/86Sr	87Sr/86Sr	1σ	87Sr/86Sr I (2.44 Ga)
180196, depth (118.70m), UOL						
L1	0.0007	0.2281	0.0085	0.7032	0.0001	0.7029
L2	0.0008	0.2387	0.0089	0.7035	0.0001	0.7032
L3	0.0008	0.2420	0.0095	0.7029	0.0001	0.7026
L4	0.0008	0.2192	0.0096	0.7038	0.0001	0.7035
L5	0.0009	0.2332	0.0102	0.7029	0.0001	0.7025
L6	0.0009	0.2381	0.0101	0.7026	0.0001	0.7022
L7	0.0008	0.2556	0.0088	0.7032	0.0001	0.7029
L8	0.0008	0.2667	0.0077	0.7036	0.0001	0.7033
180198, depth (125.63m), UOL						
L1	0.0010	0.2553	0.0103	0.7032	0.0001	0.7028
L2	0.0008	0.2499	0.0089	0.7035	0.0001	0.7032
L3	0.0008	0.2690	0.0082	0.7032	0.0001	0.7029
L4	0.0008	0.2379	0.0091	0.7038	0.0001	0.7035
L5	0.0009	0.2555	0.0095	0.7034	0.0001	0.7031
L5 (modified)	0.0009	0.2551	0.0093	0.7034	0.0001	0.7031
L6	0.0008	0.2342	0.0095	0.7033	0.0001	0.7030
180200, depth (135.35m), MOL						
L1	0.0004	0.2698	0.0036	0.7031	0.0001	0.7029
L2	0.0003	0.2296	0.0041	0.7027	0.0001	0.7026
L3	0.0004	0.2387	0.0041	0.7024	0.0001	0.7023
L4	0.0005	0.3096	0.0040	0.7031	0.0001	0.7029
L5	0.0004	0.2793	0.0042	0.7031	0.0001	0.7030
L6	0.0004	0.2988	0.0036	0.7032	0.0001	0.7030
L7	0.0003	0.2688	0.0031	0.7030	0.0001	0.7029
L8	0.0004	0.2773	0.0037	0.7031	0.0001	0.7030
L9	0.0004	0.3132	0.0037	0.7029	0.0001	0.7028
L10	0.0003	0.2891	0.0033	0.7032	0.0001	0.7031
180202, depth (144.40m), MOL						
L1	0.0004	0.2813	0.0034	0.7030	0.0001	0.7029
L2	0.0003	0.2590	0.0035	0.7034	0.0001	0.7032
L3	0.0004	0.2702	0.0046	0.7028	0.0001	0.7026
L4	0.0008	0.2487	0.0090	0.7031	0.0001	0.7027
L5	0.0007	0.2467	0.0086	0.7032	0.0001	0.7029
L6	0.0003	0.2689	0.0035	0.7032	0.0001	0.7031
L7	0.0004	0.2697	0.0037	0.7030	0.0001	0.7029
L8	0.0004	0.3022	0.0035	0.7029	0.0001	0.7028
L9	0.0004	0.2699	0.0038	0.7030	0.0001	0.7029
180204, depth (156.18m), MOL						
L1	0.0004	0.2380	0.0049	0.7030	0.0001	0.7028
L2	0.0004	0.2445	0.0042	0.7035	0.0001	0.7033
L3	0.0005	0.2477	0.0052	0.7034	0.0001	0.7032
L4	0.0004	0.2530	0.0044	0.7032	0.0001	0.7031
L5	0.0005	0.2724	0.0049	0.7036	0.0001	0.7034
L6	0.0004	0.2328	0.0047	0.7035	0.0001	0.7033
L7	0.0005	0.2589	0.0049	0.7030	0.0001	0.7028
180205, depth (158.90m), MOL						
L1	0.0003	0.2319	0.0038	0.7030	0.0001	0.7029
L2	0.0004	0.2816	0.0036	0.7028	0.0001	0.7027
L3	0.0004	0.2626	0.0037	0.7029	0.0001	0.7027
L4	0.0003	0.2351	0.0035	0.7030	0.0001	0.7029
L5	0.0003	0.2061	0.0035	0.7028	0.0001	0.7027
L6	0.0003	0.2246	0.0038	0.7029	0.0001	0.7027
L7	0.0003	0.2201	0.0036	0.7030	0.0001	0.7029

Sample	Rb (V)	Sr (V)	87Rb/86Sr	87Sr/86Sr	1σ	87Sr/86Sr I (2.44 Ga)
180205, depth (158.90m), MOL (continued)						
L8	0.0003	0.2366	0.0033	0.7032	0.0001	0.7031
L9	0.0002	0.1964	0.0031	0.7038	0.0001	0.7037
180206, depth (160.08m), LOL						
L1	0.0004	0.2367	0.0045	0.7032	0.0001	0.7031
L2	0.0003	0.2366	0.0036	0.7031	0.0001	0.7029
L3	0.0004	0.2495	0.0040	0.7029	0.0001	0.7027
L4	0.0006	0.2404	0.0069	0.7027	0.0001	0.7024
L5	0.0006	0.2112	0.0076	0.7032	0.0001	0.7029
L6	0.0004	0.2366	0.0046	0.7027	0.0001	0.7025
L7	0.0005	0.2767	0.0052	0.7028	0.0001	0.7026
180210, depth (171.73m), Footwall						
L1	0.0003	0.2795	0.0026	0.7027	0.0001	0.7026
L2	0.0003	0.2946	0.0030	0.7029	0.0001	0.7028
L3	0.0002	0.2415	0.0025	0.7031	0.0001	0.7030
L4	0.0002	0.2588	0.0025	0.7030	0.0001	0.7030
L5	0.0003	0.2754	0.0027	0.7025	0.0001	0.7025
L6	0.0003	0.2607	0.0025	0.7030	0.0001	0.7029
L7	0.0003	0.2591	0.0029	0.7030	0.0001	0.7029
L8	0.0003	0.2792	0.0029	0.7030	0.0001	0.7029
180211, depth (177.70m), Footwall						
L1	0.0002	0.1953	0.0023	0.7025	0.0001	0.7024
L2	0.0002	0.2001	0.0026	0.7026	0.0001	0.7025
L3	0.0002	0.2435	0.0024	0.7039	0.0001	0.7038
L4	0.0009	0.2331	0.0103	0.7031	0.0001	0.7027
L5	0.0002	0.2590	0.0020	0.7025	0.0001	0.7025
L6	0.0002	0.2657	0.0022	0.7030	0.0001	0.7030

6.0 Discussion

6.1 Strontium isotopes and magma type(s)

Plagioclase grains from the Mustavaara deposit show constant initial $^{87}Sr/^{86}Sr$ throughout the stratigraphy of the deposit. The average initial $^{87}Sr/^{86}Sr$ is approximately 0.7030 ± 0.0005. This is similar to the average initial $^{87}Sr/^{86}Sr$ ratio in the Kemi intrusion (Yang et al., 2016), and to the average initial $^{87}Sr/^{86}Sr$ ratio of the 2.44-2.5 Ga siliceous high-magnesium basalt (SHMB) series dykes, which range from 0.7028 to 0.7036 (Guo et al., 2013). As such, it can be inferred that the Mustavaara deposit formed from a parental magma similar to the 2.44-2.5 Ga SHMB series dykes in the Fennoscandian shield. On the other hand, this is in contrast to the 2.44-2.5 Ga low-Ti tholeiitic dykes, which yield lower average initial $^{87}Sr/^{86}Sr$ ratios of 0.7022, as noted by Guo et al. (2013). In addition, Yang et al. (2016) notes that other 2.44-2.5 Ga PGE and Cr-bearing layered intrusions in the Fennoscandian shield, associated with the same plume magmatism, also yield similar initial $^{87}Sr/^{86}Sr$ ratios to the SHBM dykes. A number of these layered intrusions, such as the Penikat intrusion in the Tornio-Näränkävaara belt, are believed to

have formed from parental magmas similar to the 2.44-2.5 Ga SHMB series dykes in the Fennoscandian shield, as shown by chemical and isotopic data (Maier et al., 2018). A graph of the $^{87}Sr/^{86}Sr$ isotopic composition of select 2.44-2.50 Ga Fennoscandian intrusions, compiled by Yang et al. (2016), is given in Figure 32.

It can be further noted that the Kemi and Penikat intrusions show isotopic and chemical evidence of crustal contamination (Yang et al., 2016; Maier et al., 2018). Whether or not crustal contamination influenced the formation of the magnetite gabbro of the Mustavaara deposit may be a topic for further study. Regardless, the isotopic data from the Mustavaara deposit shows that SHMB series magma is capable of producing an economic vanadium deposit, in addition to PGE and Cr deposits.

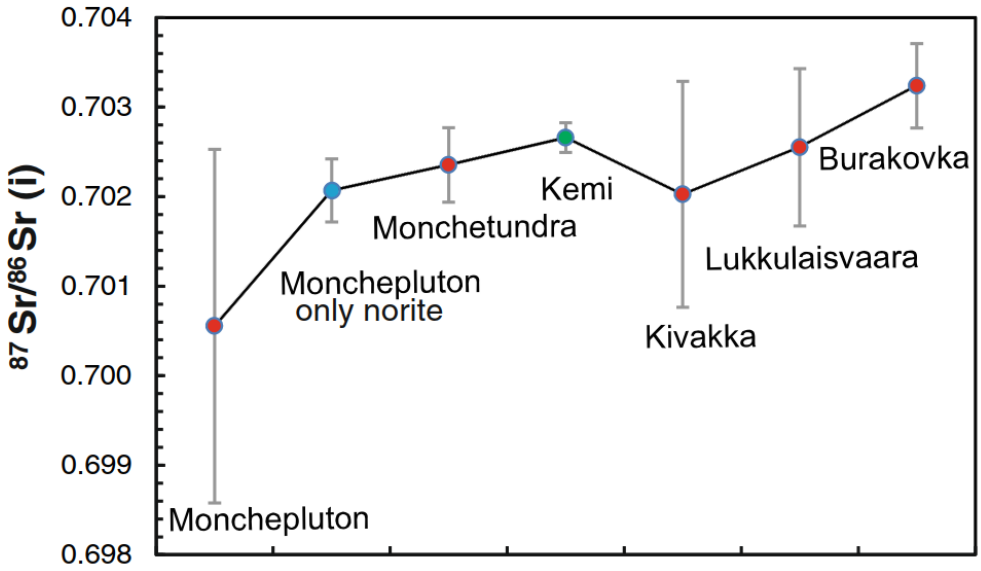

Figure 32: Initial 87Sr/86Sr isotope composition of 2.44-2.50 Ga layered intrusions in northern Fennoscandia. Reprinted by permission of Springer Nature Customer Service Centre GmbH: Springer, Mineralium Deposita, Mantle source of the 2.44–2.50-Ga mantle plume-related magmatism in the Fennoscandian Shield: evidence from Os, Nd, and Sr isotope compositions of the Monchepluton and Kemi intrusions. Yang et al. Copyright 2016

The uniformity in the $^{87}Sr/^{86}Sr$ data implies that the deposit formed from a single magma pulse in a closed system; the magma chamber was not replenished during the formation of the magnetite gabbro host of the Mustavaara deposit, in contrast to the Panzhihua intrusion as described by Pang et al. (2009). In order for the Mustavaara deposit to have formed due to multiple magma pulses, the new magma would need to have had a similar isotopic composition to the existing magma.

6.2 Trace element constraints on the ore forming processes

Based on mineralogy and geochemistry, Karinen (2010) proposed that the magnetite gabbro host of the Mustavaara deposit is a sandwich horizon, due to decreasing An content from the hanging wall downward, and from the footwall upward. LREEs such as La and Ce are highly incompatible in plagioclase, clinopyroxene, and oxides (Bédard, 2001). Thus, these elements should behave incompatibly during magma fractionation, with a bulk partition coefficient of significantly less than 1. The spot traverse analyses show increasing Ce concentration from the cores of the plagioclase grains to the rims (Figures 20, 22, 24, 26), reflecting the incompatible behavior of LREEs and the crystallization of trapped liquid. This is in contrast to large intrusions such as the Bushveld intrusion, in which LREE-enriched rims have not been preserved due to diffusion and slower cooling (Yang et al., 2019). There is an increasing trend in the Ce concentrations in the cores of grains in the UOL relative to the hanging wall and footwall. The UOL also exhibits the lowest An at a depth of about 119 m. As such, the REE data, showing the opposite trend of the An content, confirms the suggestion by Karinen (2010) that the magnetite gabbro is a sandwich horizon, and further identifies the UOL around the depth of 119 m as the most evolved portion of the sandwich horizon. It can also be noted that the MOL may also be highly evolved around the 135 m depth, as evidenced by low An similar to the UOL.

It is observed that the highest Ti and V concentrations of each plagioclase sample display similar variation patterns to An, indicating that Ti and V behave compatibly with their bulk partition coefficient being greater than 1. Additionally, the isotope data indicates that the Mustavaara deposit formed from a single magma pulse; magma replenishment did not occur. As such, one possible interpretation may be that the plagioclase, clinopyroxene, and oxides crystallized together in a manner similar to their co-crystallization in the Skaergaard intrusion (Humphreys, 2009). This is supported by the similar V^{4+}/V^{3+} ratio of the magnetite from Mustavaara to the Skaergaard magnetite (Balan et al., 2006).

7.0 Conclusions

The Mustavaara Fe-Ti-V deposit formed from a SHMB parent magma in the Western intrusion of the Koillismaa intrusive complex, in association with the 2.44-2.5 Ga plume magmatism that formed the Tornio-Näränkävaara intrusive belt. The host rock of the deposit, a magnetite gabbro, is the sandwich horizon of the intrusive body (Karinen, 2010). Isotopic data

suggests that the magnetite gabbro formed in a closed system from a single pulse of magma; magma mixing would not have had a role in the formation of the ore minerals, unless a new magma with a similar initial isotopic composition was injected into the magma chamber. As such, it is likely that the oxide minerals either co-crystallized with the silicate minerals, or were the last minerals to crystallize.

Along the stratigraphy of the deposit, the Upper ore layer is observed to contain elevated LREE (i.e. Ce) concentrations, lower Ti and V concentrations, and the lowest An content. As such, the UOL, around the depth of 119 m along borehole MV-64-2011, is identified by trace element and anorthite data as the most evolved portion of the magnetite gabbro.

8.0 Acknowledgements

First and foremost, I would like to thank my thesis supervisors, Dr. Tuomo Karinen of GTK, Dr. Shenghong Yang and Marko Moilanen of the University of Oulu.

K.H. Renlund Foundation is thanked for funding this research project.

Dr. Hugh O'Brien, Dr. Yann Lahaye, and Dr. Matti Kurhila of GTK are thanked for their generous help in the trace element and isotope analyses. Marko Moilanen is thanked for his assistance in electron microprobe analyses.

9.0 References

Alapieti, T. (1982). *The Koillismaa layered igneous complex, Finland - its structure, mineralogy and geochemistry, with emphasis on the distribution of chromium*. Geological Survey of Finland, Bulletin 319, 1-116.

Alapieti, T., Hugg, R., & Piirainen, T. (1979). *Structure, mineralogy and chemistry of the Syöte section in the Early Proterozoic Koillismaa layered intrusion, northeastern Finland*. Geological Survey of Finland, Bulletin 299, 1-43.

Balan, E., De Villiers, J. P. R., Eeckhout, S. G., Glatzel, P., Toplis, M. J., Fritsch, E., Allard, T., Galoisy, L., Calas, G. (2006). The oxidation state of vanadium in titanomagnetite from layered basic intrusions. *American Mineralogist*, 91, 953-956.

Bauer, G., Güther, V., Hess, H., Otto, A., Roidl, O., Roller, H., & Sattelberger, S. (1996). Vanadium and Vanadium Compounds. In: Laird, T. (ed), *Ullmann's Encyclopedia of Industrial Chemistry*, Vol. A27, 367-387.

Bédard, J. H. (2001). Parental magmas of the Nain Plutonic Suite anorthosites and mafic cumulates: a trace element modelling approach. *Contributions to Mineralogy and Petrology*, 141, 747-771.

Bowen, N. L. (1915). Crystallization-differentiation in silicate liquids. *American Journal of Science*, 230, 175-191.

Cawthorn, R. G., Barnes, S. J., Ballhaus, C., & Malitch, K. N. (2005). Platinum-group element, chromium, and vanadium deposits in mafic and ultramafic rocks. *Economic Geology*, 100, 215-249.

Conn, H. K. (1979). The Johns-Manville Platinum-Palladium Prospect, Stillwater Complex, Montana, U.S.A. *Canadian Mineralogist*, 17, 463-468.

Daly, J. S., Balagansky, V. V., Timmerman, M. J., & Whitehouse, M. J. (2006). The Lapland-Kola orogen: Palaeoproterozoic collision and accretion of the northern Fennoscandian lithosphere. *Geological Society London Memoirs*, 32, 579-598.

Dupuis, C., & Beaudoin, G. (2011). Discriminant diagrams for iron oxide trace element fingerprinting of mineral deposit types. *Mineralium Deposita*, 46, 319-335.

Emslie, R. F., & Ermanovics, I. F. (1975). Major rock units of the Morin Complex, southwestern Quebec. *Geological Survey of Canada*, Paper 74-48, 1-37.

Force, E. R. (1991). Geology of Titanium-Mineral Deposits. *Geological Society of America Special Papers*, 259, 1-112.

Gross, G. A. (1996). Mafic Intrusion-Hosted Titanium-Iron. In: Eckstrand, O. R., Sinclair, W. D., & Thorpe, R. I. (eds), *Geology of Canadian Mineral Deposit Types*, Geological Society of America, 573-582.

Guo, F., Maier, W. D., Vuollo, J., Lahaye, Y., Huhma, H., O'Brien, H., Junttila, H. (2013). Geochemistry of ~2.45 Ga mafic dykes in Northern Finland: constraints on the origin of PGE mineralization in coeval layered intrusions. 12th SGA biennial meeting, Uppsala, Sweden.

Haapala, I., & Papunen, H. (2015). A History of Exploration for and Discovery of Finland's Ore Deposits. In: Maier, W. D., Lahtinen, R., & O'Brien, H. (eds), *Mineral Deposits of Finland*. Elsevier B.V., 1-38.

Hanski, E. (2015). Synthesis of the Geological Evolution and Metallogeny of Finland. In: Maier, W. D., Lahtinen, R., & O'Brien, H. (eds), *Mineral Deposits of Finland*. Elsevier B.V., 39-71.

Herrington, R. (2011). Geological Features and Genetic Models of Mineral Deposits. In: Darling, P. (ed), *SME Mining Engineering Handbook Society for Mining, Metallurgy, and Exploration* (3rd edition.), 83-104.

Humphreys, M. C. S. (2009). Chemical Evolution of Intercumulus Liquid, as Recorded in Plagioclase Overgrowth Rims from the Skaergaard Intrusion. *Journal of Petrology*, 50, 127-145.

Iljina, M., & Hanski, E. (2005). Layered mafic intrusions of the Tornio—Näränkävaara belt. In: Lehtinen, M., Nurmi, P. A., Rämö, O. T. (eds), *Precambrian Geology of Finland – Key to the Evolution of the Fennoscandian Shield*. *Developments in Precambrian Geology*, 14, Elsevier B.V., 101-137.

Iljina, M. J., Karinen, T. T., & Räsänen, J. E. (2001). *The Koillismaa Layered Igneous Complex, general geology, structural development and related sulphide and platinum-group element mineralization*. In *Proceedings of the Sixth Biennial SGA–SEG meeting.* Balkema Publishers, Lisse, 649-652.

Iljina, M., Maier, W. D., Karinen, T. (2015). PGE-(Cu-Ni) Deposits of the Tornio-Näränkävaara Belt of Intrusions (Portimo, Penikat, and Koillismaa). In: Maier, W. D., Lahtinen, R., & O'Brien, H. (eds), *Mineral Deposits of Finland*. Elsevier B.V., 133-164.

Irvine, T. N. (1982). Terminology for Layered Intrusions. *Journal of Petrology*, 23, 127-162.

Irvine, T. N., Andersen, J. C. Ø., & Brooks, C. K. (1998). Included blocks (and blocks within blocks) in the Skaergaard intrusion: Geologic relations and the origins of rhythmic modally graded layers. *Geological Society of America Bulletin*, 11, 1398-1447.

Juopperi, A. (1977). *The magnetite gabbro and related Mustavaara vanadium ore deposit in the Porttivaara layered intrusion, north-eastern Finland*, Geological Survey of Finland, Bulletin 288, 1-68.

Karinen, T. (2010). The Koillismaa Intrusion, northeastern Finland – evidence for PGE reef forming processes in the layered series. Geological Survey of Finland, Bulletin 404, 1-176.

Karinen, T., Hanski, E., & Taipale, A. (2015). The Mustavaara Fe-Ti-V Oxide Deposit. In: Maier, W. D., Lahtinen, R., & O'Brien H (eds), *Mineral Deposits of Finland*, Elsevier B.C., 179-194.

Latypov, R., & Egorova, V. (2012). Plagioclase compositions give evidence for in situ crystallization under horizontal flow conditions in mafic sills. *Geology*, 40, 883-886.

Lister, G. F. (1966). The composition and origin of selected iron-titanium deposits. *Economic Geology*, 61, 275-310.

Luukas, J., Kousa, J., Nironen, M., & Voullo, J. (2017). *Major stratigraphic units in the bedrock of Finland, and an approach to tectonostratigraphic division*. Geological Survey of Finland, Special Paper 60, 9-40.

Maier, W. D., Barnes, S.-J., & Groves, D. I. (2013). The Bushveld Complex, South Africa: formation of platinum–palladium, chrome- and vanadium-rich layers via hydrodynamic sorting of a mobilized cumulate slurry in a large, relatively slowly cooling, subsiding magma chamber. *Mineralium Deposita*, 48, 1-56.

Maier, W. D., Halkoaho, T., Huhma, H., Hanski, E., & Barnes, S.-J. (2018). The Penikat Intrusion, Finland: Geochemistry, Geochronology, and Origin of Platinum–Palladium Reefs. *Journal of Petrology*, 59, 967-1006.

McCallum, I. S. (1996). The Stillwater Complex. In: Cawthorn, R. G. (ed), *Layered Intrusions*, Elsevier Science, 441-483.

Müller, W., Shelley, M., Miller, P., Broude, S. (2009). Initial performance metrics of a new custom-designed ArF excimer LA-ICPMS system coupled to a two-volume laser-ablation cell. *Journal of Analytical Atomic Spectrometry*, 24, 209-214

Namur, O., Abily, B., Boudreau, A. E., Blanchette, F., Bush, J. W. M., Ceuleneer, G., Charlier, B., Donaldson, C. H., Duchesne, J., Higgins, M. D., Morata, D., Nielsen, T. F. D., O'Driscoll, B., Pang, K. N., Peacock, T., Spandler, C. J., Toramaru, A., Veksler, I. V. (2015). Igneous Layering in Basaltic Magma Chambers. In: Charlier, B., Namur, O., Latypov, R., & Tegner, C. (eds). *Layered Intrusions*, Springer, 75-152.

Naslund, H. R., & McBirney, A. R. (1996). Mechanisms of Formation of Igneous Layering. In: Cawthorn, R. G. (ed), *Layered Intrusions*, Elsevier Science, 1-43.

O'Driscoll, B., & VanTongeren, J. A. (2017). Layered Intrusions: From Petrological Paradigms to Precious Metal Repositories. *Elements*, 13, 383-389.

Pang, K.-N., Zhou, M.-F., Lindsley, D., Zhao, D., & Malpas, J. (2007). Origin of Fe-Ti Oxide Ores in Mafic Intrusions: Evidence from the Panzhihua Intrusion, SW China. *Journal of Petrology*, 49, 295-313.

Pang, K.-N., Li, C., Zhou, M.-F., & Ripley, E. M. (2009). Mineral compositional constraints on petrogenesis and oxide ore genesis of the late Permian Panzhihua layered gabbroic intrusion, SW China. *Lithos*, 110, 199-214.

Rankenburg, K., Lassiter, J.C., Brey, G., 2004, Origin of megacrysts in volcanic rocks of the Cameroon volcanic chain - constraints on magma genesis and crustal contamination, Contribution to Mineralogy and Petrology, 147, 129-144.

Reguir, E. P., Chakhmouradian, A. R., Halden, N. M., Yang, P., & Zaitsev, A. N. (2008). Early Magmatic And Reaction-Induced Trends In Magnetite From The Carbonatites Of Kerimasi, Tanzania. *The Canadian Mineralogist*, 46, 879-900.

Scoates, J. S., & Wall, C. J. (2015). Geochronology of Layered Intrusions. In: Charlier, B., Namur, O., Latypov, R., & Tegner, C. (eds). *Layered Intrusions*, Springer, 3-74.

Stewart, B. W., & Depaolo, D. J. (1990). Isotopic studies of processes in mafic magma chambers: II. The Skaergaard Intrusion, East Greenland. *Contributions to Mineralogy and Petrology*, 104, 125-141.

Thirlwall, M.F., 1991. Long-term reproducibility of multicollector Sr and Nd isotope ratio analysis. *Chemical Geology*, 94, 85-104.

VanTongeren, J. A., & Mathez, E. A. (2012). Large-scale liquid immiscibility at the top of the Bushveld Complex, South Africa. *Geology*, 40, 491-494.

Wager, L. R., & Brown, G. M. (1968). *Layered Igneous Rocks*. Oliver & Boyd Ltd.

Winter, J. D. (2010). *Principles Of Igneous And Metamorphic Petrology* (2nd edition). Pearson Education, Inc.

Yang, S.-H., Hanski, E., Li, C., Maier, W. D., Huhma, H., Mokrushin, A. V., Latypov, R., Lahaye, Y., O'Brien, H., Qu, W.-J. (2016). Mantle source of the 2.44–2.50-Ga mantle plume-related magmatism in the Fennoscandian Shield: evidence from Os, Nd, and Sr isotope compositions of the Monchepluton and Kemi intrusions. *Mineralium Deposita*, 51, 1055-1073.

Yang, S.-H., Maier, W. D., Godel, B., Barnes, S.-J., Hanski, E., O'Brien, H. (2019). Parental Magma Composition of the Main Zone of the Bushveld Complex: Evidence from *in situ* LA-ICP-MS Trace Element Analysis of Silicate Minerals in the Cumulate Rocks. *Journal of Petrology*, 60, 359-392.

Figure 1

Reprinted from Mineral Deposits of Finland, Vol 1, Maier, W. D., Lahtinen, R., O'Brien, H. (eds.), Haapala, I., Papunen, H. A History of Exploration For and Discovery of Finland's Ore Deposits, 1-38, Copyright (2015), with permission from Elsevier.

Figure 2

Reprinted from Mineral Deposits of Finland, Vol 1, Maier, W. D., Lahtinen, R., O'Brien, H. (eds.), Iljina, M., Maier, W. D., & Karinen, T., PGE-(Cu-Ni) Deposits of the Tornio-Näränkävaara Belt of Intrusions (Portimo, Penikat, and Koillismaa), 133-164, Copyright (2015), with permission from Elsevier (2015).

Figures 3 - 5

Reprinted from Mineral Deposits of Finland, Vol 1, Maier, W. D., Lahtinen, R., O'Brien, H. (eds.), Karinen, T., Hanski, E., & Taipale, A. The Mustavaara Fe-Ti-V Deposit, 179-194, Copyright (2015), with permission from Elsevier.

Figure 32

Reprinted by permission from Springer Nature Customer Service Centre GmbH: Springer, *Mineralium Deposita*, Mantle source of the 2.44–2.50-Ga mantle plume-related magmatism in the Fennoscandian Shield: evidence from Os, Nd, and Sr isotope compositions of the Monchepluton and Kemi intrusions, Yang, S.-H., Hanski, E., Li, C., Maier, W. D., Huhma, H., Mokrushin, A. V., Latypov, R., Lahaye, Y., O'Brien, H., Qu, W.-J., Copyright 2016

10.0 Appendices

10.1 Appendix 1: Thin Section Descriptions

At 68.06 m, the hanging wall contains 44.8 vol% plagioclase, 11.8 vol% oxides, and 43.4 vol% amphibole (altered clinopyroxene). The plagioclase can be described as euhedral, with grain sizes generally varying from 0.5 to 0.8 mm on the long axis (Figure 33); the plagioclase is equigranular. Twinning planes have variable sharpness (Figure 33). The plagioclase shows mild igneous lamination. The clinopyroxene grains have altered to a green-colored amphibole with anhedral texture. These altered clinopyroxene grains are interstitial to the plagioclase grains. The oxide grains are generally euhedral, with larger grains showing annealing texture. The oxide grain sizes vary from less than 0.1 mm to over 0.5 mm in diameter.

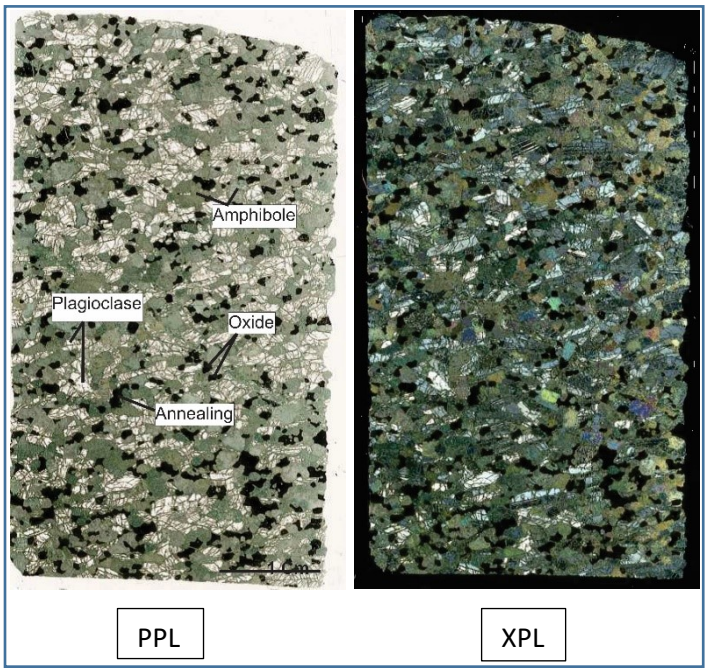

Figure 33: Microscope photo of thin section from depth 68.06 m (Hanging wall). The width of each view is about 3 cm.

At 84.73 m, the hanging wall contains 55.7 vol% plagioclase, 7.9 vol% oxides, and 36.3 vol% amphibole (altered clinopyroxene). The plagioclase can be described as euhedral, with grain sizes generally varying from 0.4 to 1 mm on the long axis (Figure 34). Twinning planes have variable sharpness (Figure 34). The plagioclase shows moderate igneous lamination. The clinopyroxene grains have been altered to a green-colored amphibole with anhedral texture. The altered clinopyroxene grains are interstitial to the plagioclase grains. The oxide grains can

generally be described as euhedral, with several larger grains showing annealing texture. The oxide grain sizes vary from less than 0.1 mm to over 0.5 mm in diameter. There is evidence of deformation in the bottom half of the thin section, with what appears to be a vein filled with the green-colored amphibole.

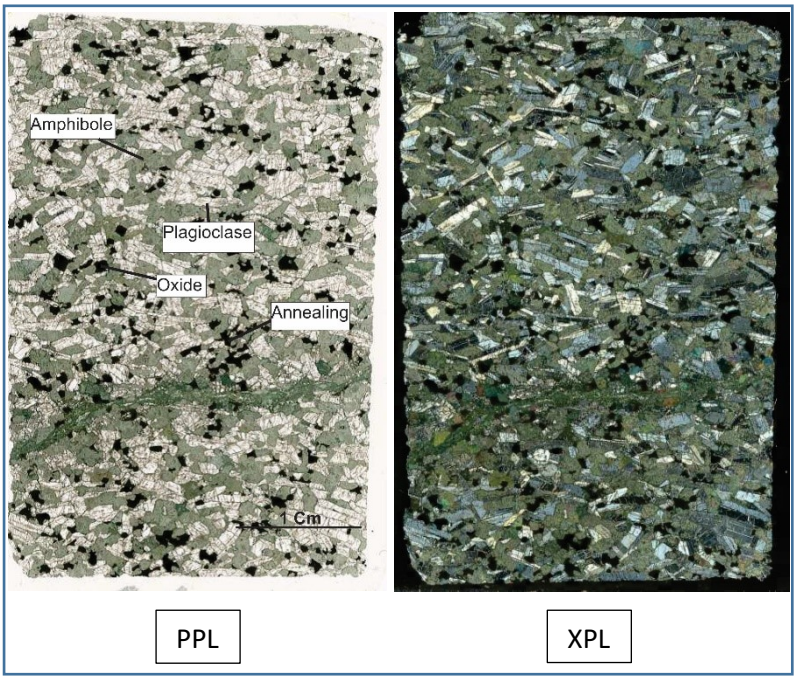

Figure 34: Microscope photo of thin section from depth 84.73 m (Hanging wall). The width of each view is about 3 cm.

At 95.74 m, the hanging wall contains 56.0 vol% plagioclase, 8.1 vol% oxides, and 35.8 vol% amphibole (altered clinopyroxene). The plagioclase can generally be described as euhedral, with grain sizes generally varying from 0.4 to 0.6 mm on the long axis (Figure 35), though many finer grains are present at this depth. Twinning planes have variable sharpness (Figure 35). The plagioclase shows mild to moderate igneous lamination. The clinopyroxene grains have been altered to a green-colored amphibole with anhedral texture. The altered clinopyroxene grains are interstitial to the plagioclase grains. The oxide grains can generally be described as euhedral, with a few larger grains showing annealing texture. The oxide grain sizes vary from less than 0.1 mm to around 0.5 mm in diameter.

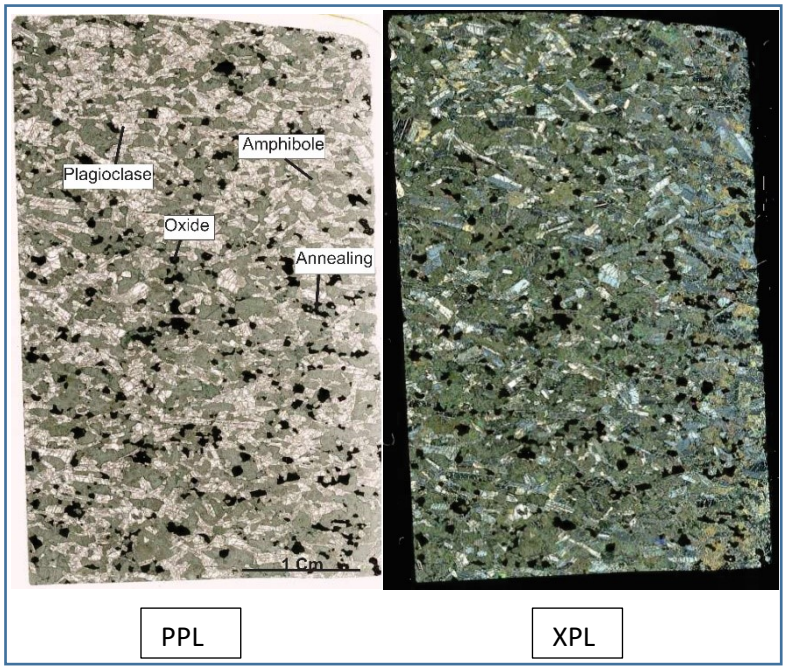

Figure 35: Microscope photo of thin section from depth 95.74 m (Hanging wall). The width of each view is about 3 cm.

At 125.63 m, the UOL contains 51.7 vol% plagioclase, 22.7 vol% oxides, and 25.6 vol% amphibole (altered clinopyroxene). The plagioclase can be described as euhedral, with grain sizes generally varying from 0.8 to 2 mm along the long axis (Figure 36). Simple twinning planes are dull, while lamellar twinning planes have highly variable sharpness (Figure 36). The plagioclase shows weak igneous lamination, which is sometimes difficult to identify due to alteration. The clinopyroxene grains have been altered to a green-colored amphibole. The altered clinopyroxene is anhedral, and interstitial to the plagioclase grains. The oxide grains are euhedral, with several larger grains showing annealing texture. The oxide grains sizes are on the 1 mm scale in diameter.

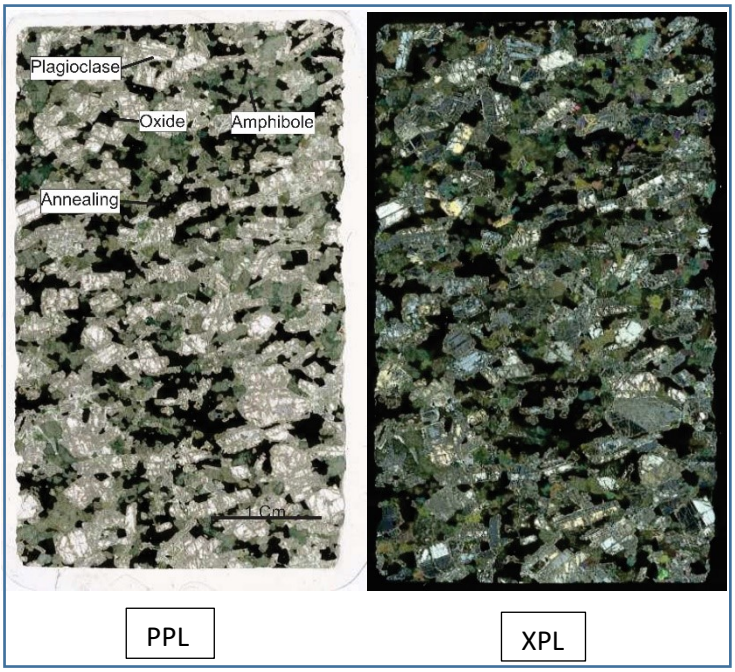

Figure 36: Microscope photo of thin section from depth 125.63 m (Upper ore layer). The width of each view is about 3 cm.

At 144.40 m, the MOL contains 53.5 vol% plagioclase, 10.5 vol% oxides, and 36.0 vol% amphibole (including altered clinopyroxene). The plagioclase can be described as euhedral, with grain sizes generally measuring 0.5 to 0.6 mm along the long axis (Figure 37). Simple twinning planes are altered, and lamellar twinning planes have variable sharpness (Figure 37). The clinopyroxene grains have been altered to a green-colored amphibole. The altered clinopyroxene is anhedral, and interstitial to the plagioclase grains. The oxide grains are euhedral, and some larger grains show annealing texture. The oxide grain sizes vary from roughly 0.1 to over 1 mm in diameter.

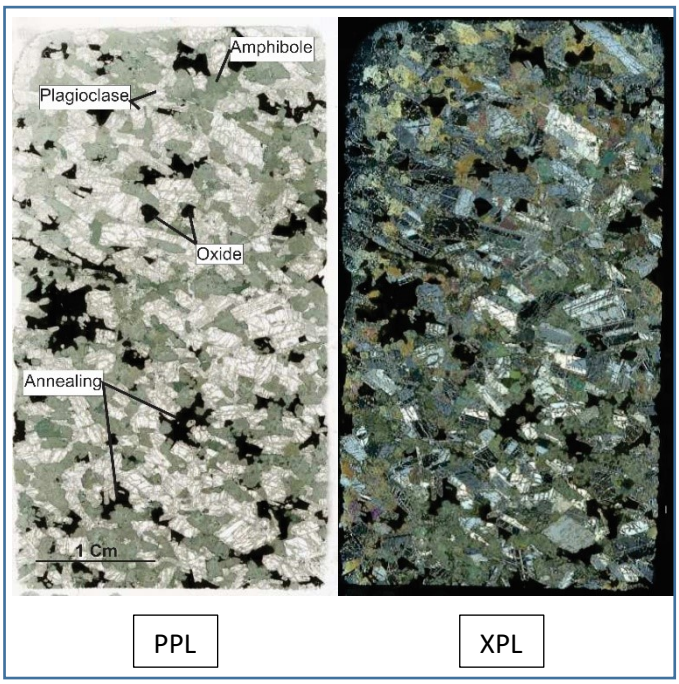

Figure 37: Microscope photo of thin section from depth 144.40 m (Middle ore layer). The width of each thin section is about 3 cm.

At 156.18 m, the MOL contains 56.7 vol% plagioclase, 11.5 vol% oxides, and 31.8 vol% amphibole (altered clinopyroxene). The plagioclase grains are euhedral, with grain sizes generally varying from 0.4 to 1 mm along the long axis (Figure 38), though alteration is abundant and can make a precise measurement difficult. Simple twinning planes are altered or less sharp than the lamellar twinning planes (Figure 38). The clinopyroxene grains have been altered to a green-colored amphibole. The altered clinopyroxene is anhedral, and interstitial to the plagioclase grains. The oxide grains are euhedral, and some large grains show annealing texture. The oxide grain sizes vary, but are generally 0.1 to around 0.5 mm in diameter.

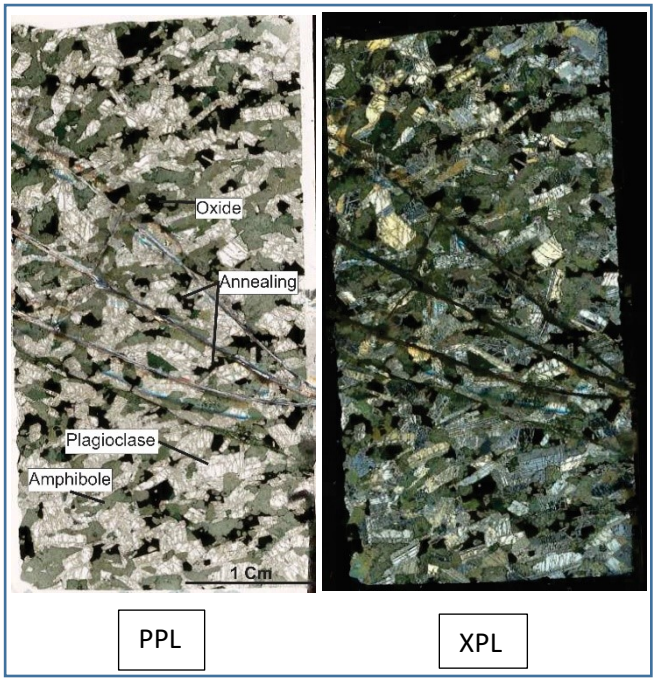

Figure 38: Microscope photo of thin section from depth 156.18 m (Middle ore layer). The width of each view is about 3 cm.

At 158.90 m, the MOL contains 60.5 vol% plagioclase, 11.5 oxides, and 28.0 vol% amphibole (altered clinopyroxene). The plagioclase grains are euhedral, with grain sizes generally measuring between 0.5 to 0.8 mm along the long axis, though grain sizes vary (Figure 39). Alteration is abundant between grains and within fractures in plagioclase. Twinning planes have variable sharpness, and lamellar twinning is more common than simple twinning (Figure 39). The clinopyroxene grains have been altered to a green-colored amphibole. The altered clinopyroxene is anhedral. The oxide grains are euhedral, and some larger grains show annealing texture. The oxide grain sizes are generally 0.1 to 0.4 mm in diameter.

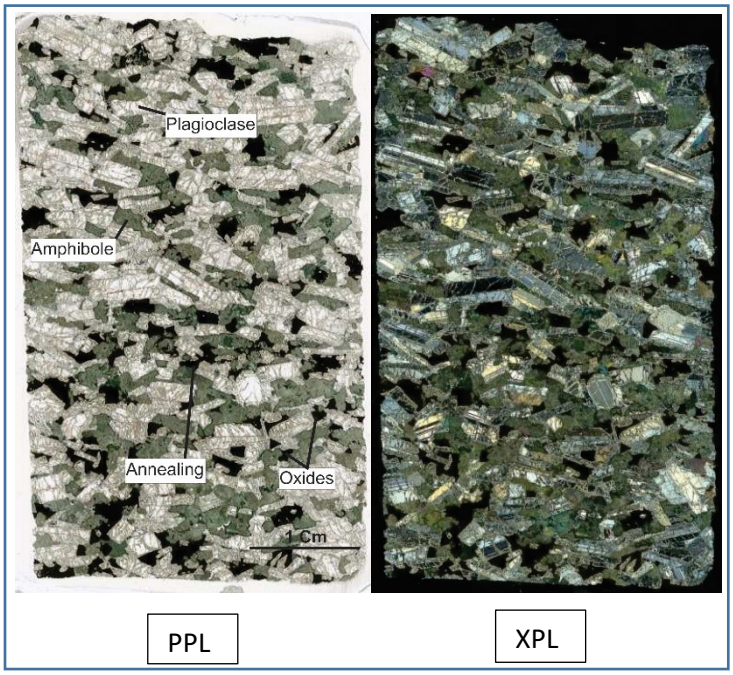

Figure 39: Microscope photo of thin section from depth 158.90 m (Middle ore layer). The width of each view is about 3 cm.

At 177.70 m, the footwall contains 76.5 vol% plagioclase, 3.6 vol% oxides, and 19.8 vol% amphibole (altered clinopyroxene). The plagioclase grains are euhedral, and grain sizes are generally 0.8 to 1 mm, but highly variable (Figure 40). Twinning planes have variable sharpness (Figure 40). The clinopyroxene grains have been altered to a green-colored amphibole. The altered clinopyroxene is anhedral. The oxide grains are anhedral, and mostly on the 1 mm scale in diameter.

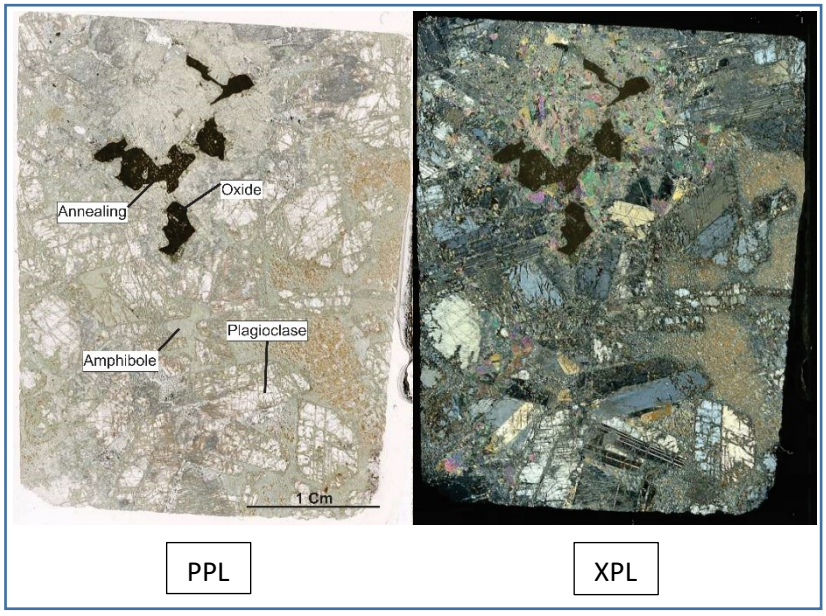

Figure 40: Microscope photo of thin section from depth 177.70 m (Footwall). The width of each view is about 3 cm.

10.2 Appendix 2: Spot Traverse Analyses

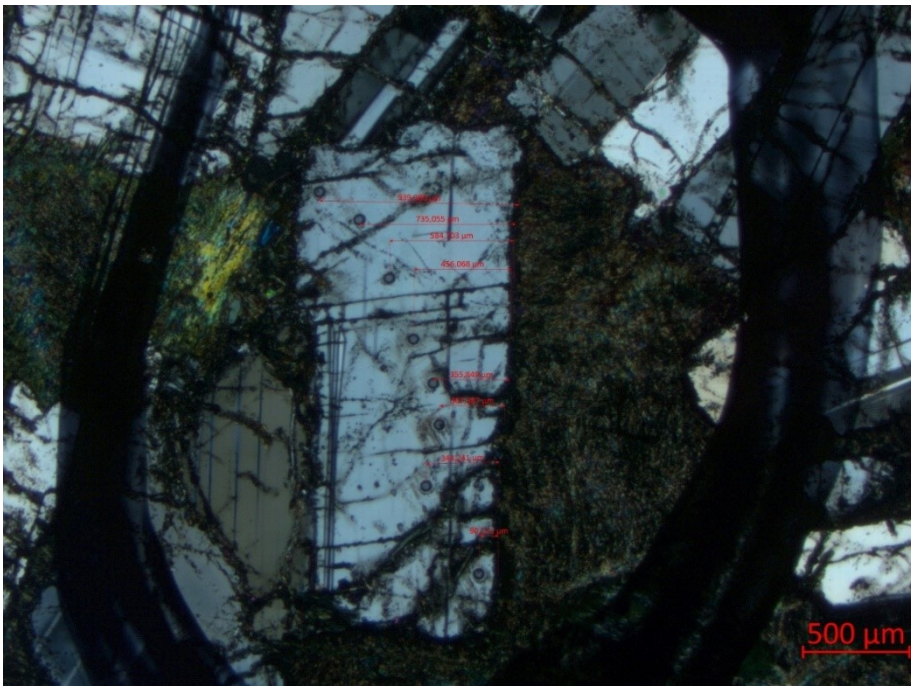

Figure 41: Thin Section 180185 Grain 2

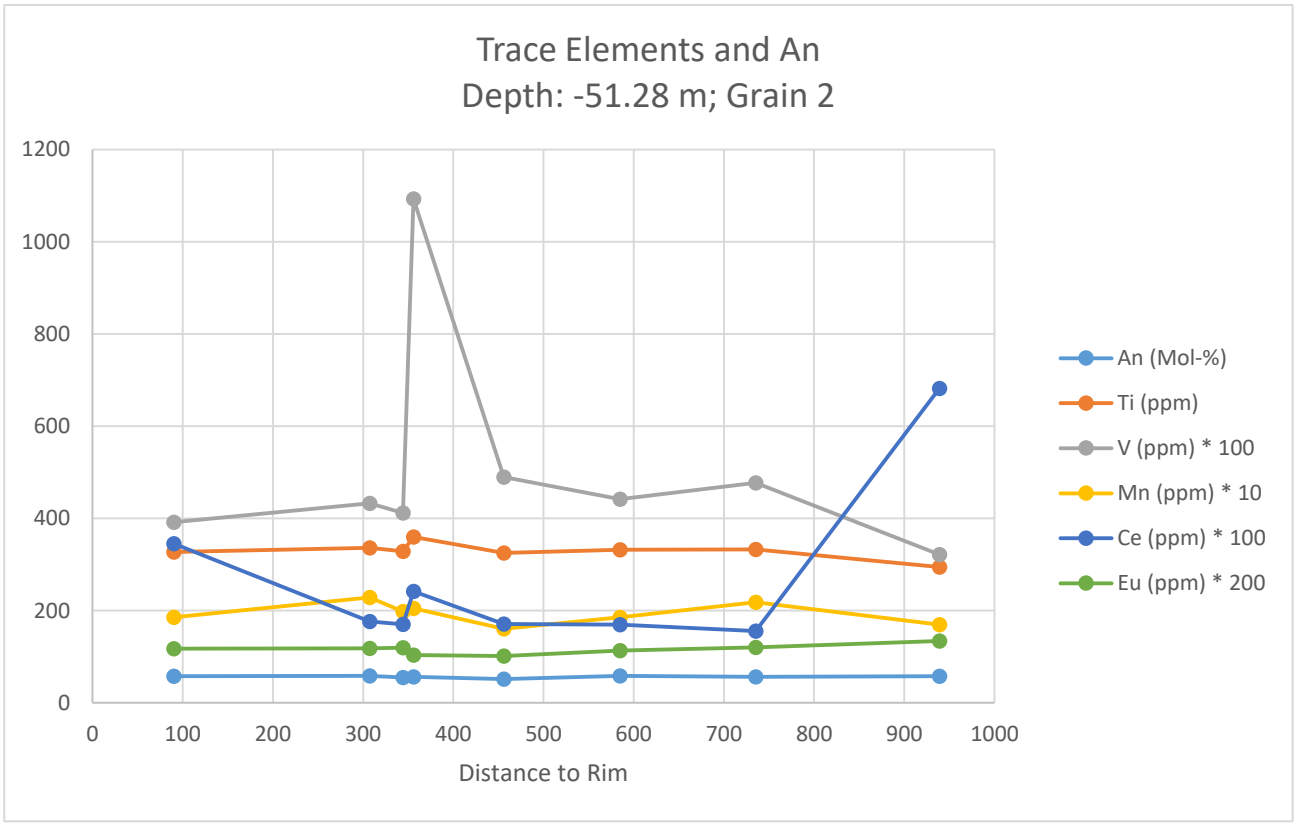

Figure 42: Spot traverse analysis, Depth: -51.28; Grain 2

The plotted data (Figure 42) indicates that the core of the grain is enriched in Ti, and V. The plot indicates fluctuation in the Mn concentration along the traverse of the grain. The plot shows that the rims of the grain are enriched in Ce. The plot indicates a slight increase in the Eu concentration along the traverse of the grain. The plot shows that the An percentage is mostly consistent throughout the grain.

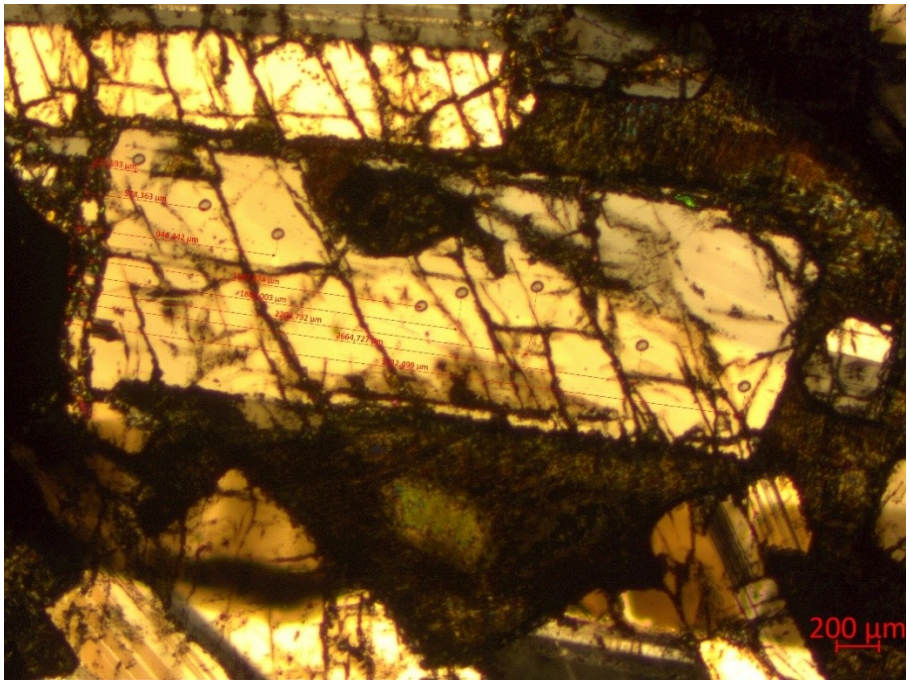

Figure 43: Thin Section 180185 Grain 3

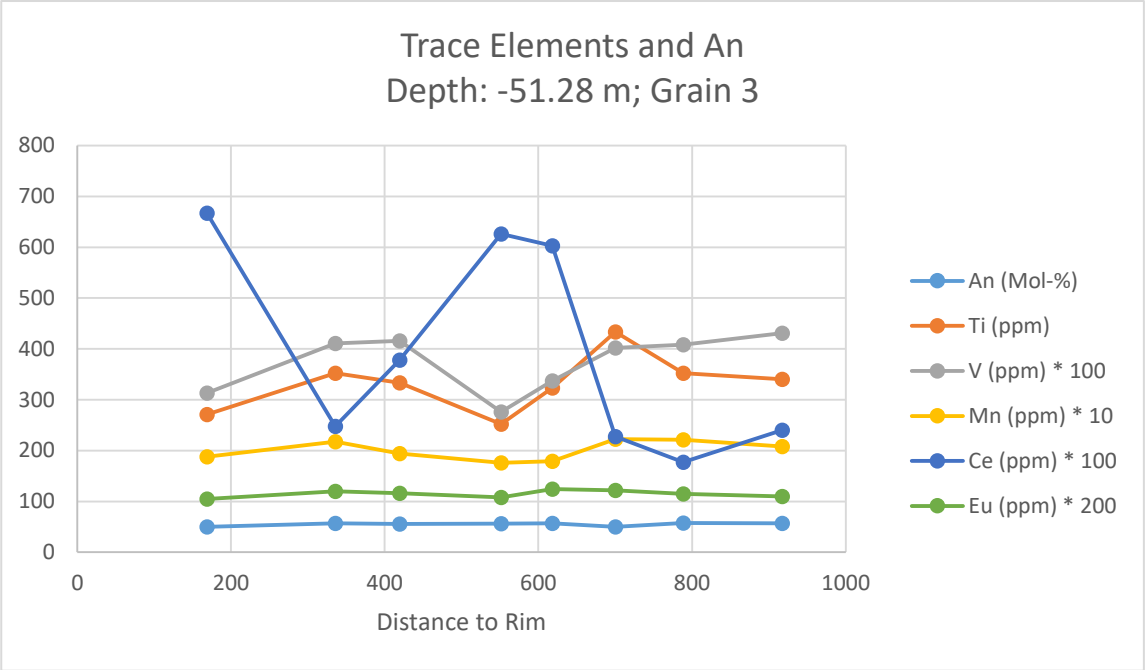

Figure 44: Spot traverse analysis, Depth: -51.28 m; Grain 3

The plot (Figure 44) shows fluctuation in the Ti, V, Mn, and Ce concentrations. The plot shows slight fluctuation but overall consistency in the Eu concentration and the An percentage.

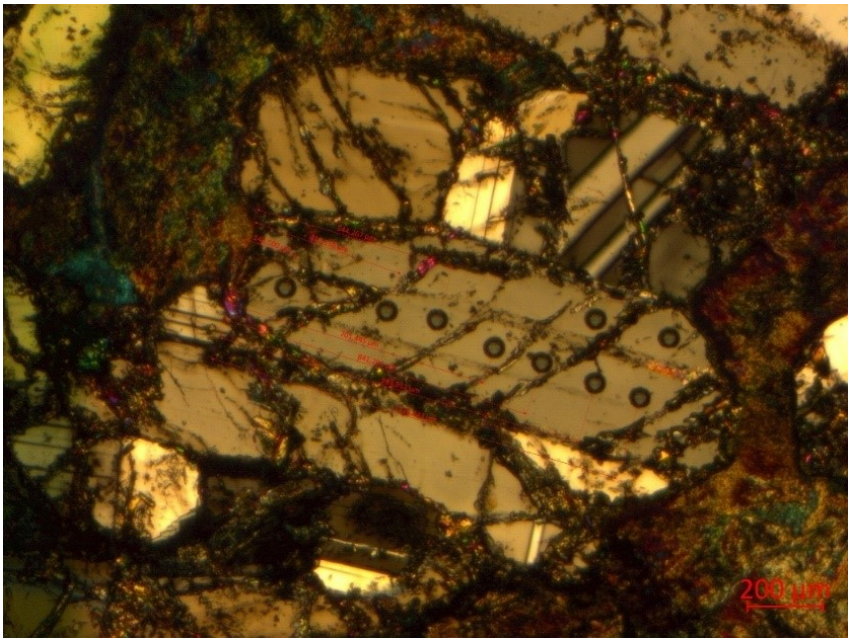

Figure 45: Thin Section 180192 Grain 1

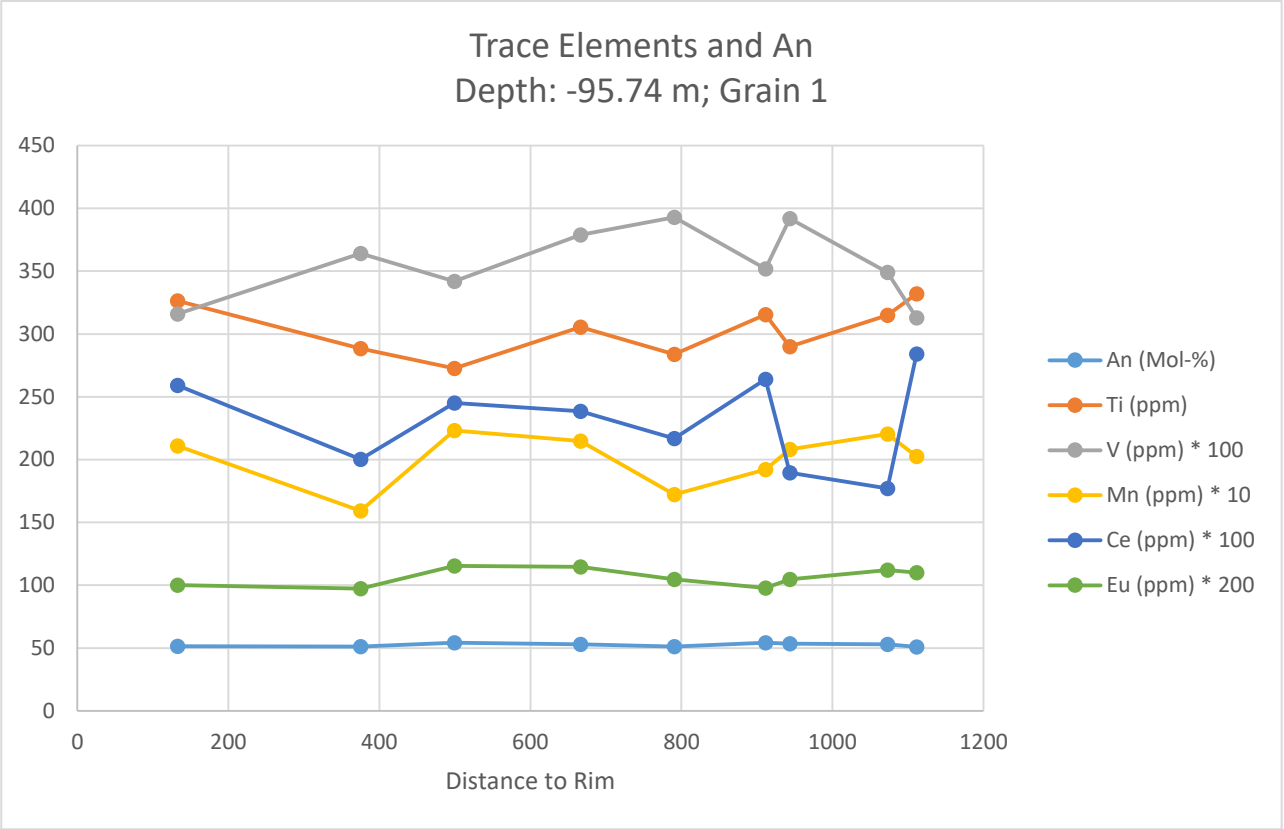

Figure 46: Spot traverse analysis, Depth: -95.74 m; Grain 1

The plot (Figure 46) shows fluctuations in the Ti, V, Mn, and Ce concentrations. The plot also shows some fluctuation in the Eu concentration, and very minor fluctuation (but general consistency) in the An percentage.

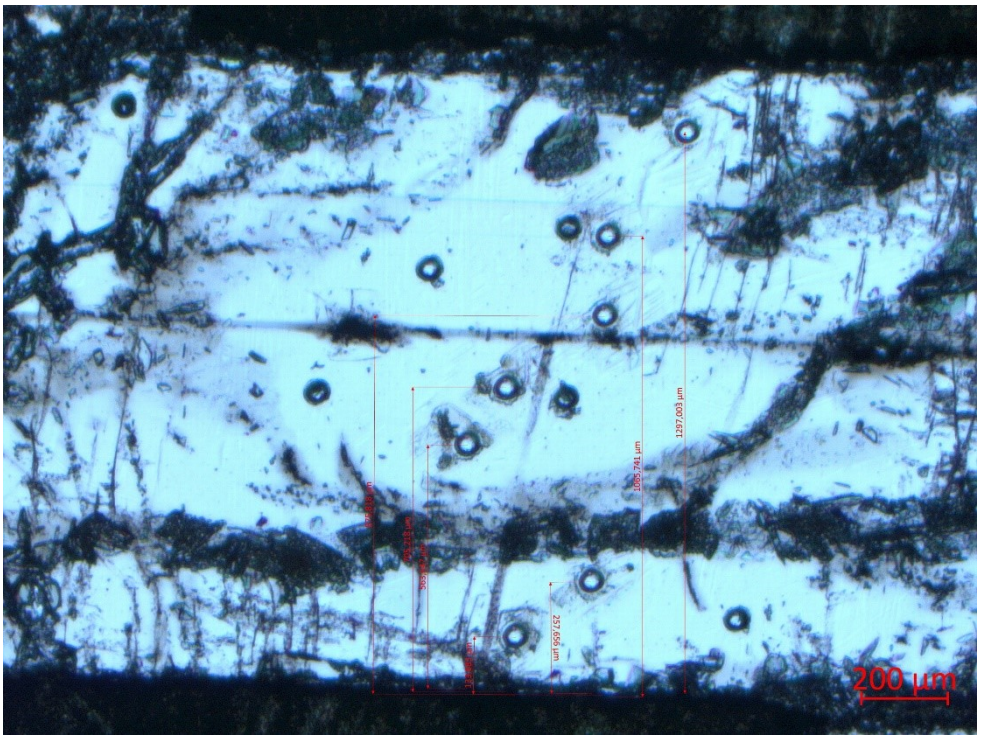

Figure 47: Thin Section 180205 Grain 1

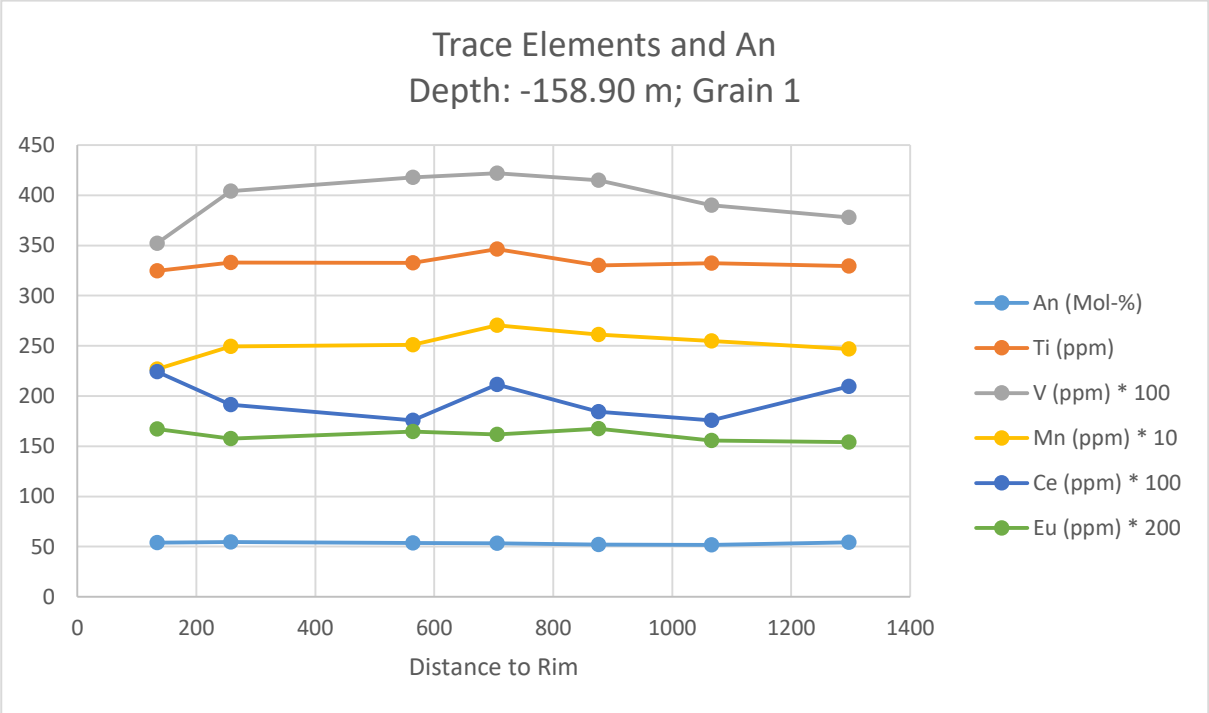

Figure 48: Spot traverse analysis, Depth: -158.90 m; Grain 1

The plot (Figure 48) shows that the core of the grain is enriched in Ti, V, and Mn. The plot also shows that the rims of the grain are enriched in Ce. The Ce concentration is also

increased in the core of the grain relative to the area between the core and the rims. The Eu increases slightly in the core of the grain. The An percentage is consistent throughout the traverse of the grain.

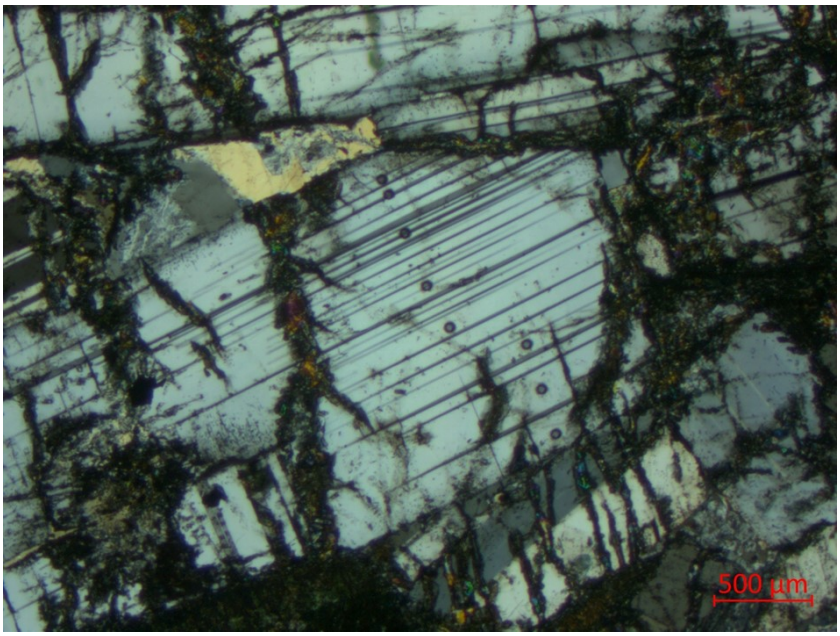

Figure 49: Thin Section 180210 Grain 1

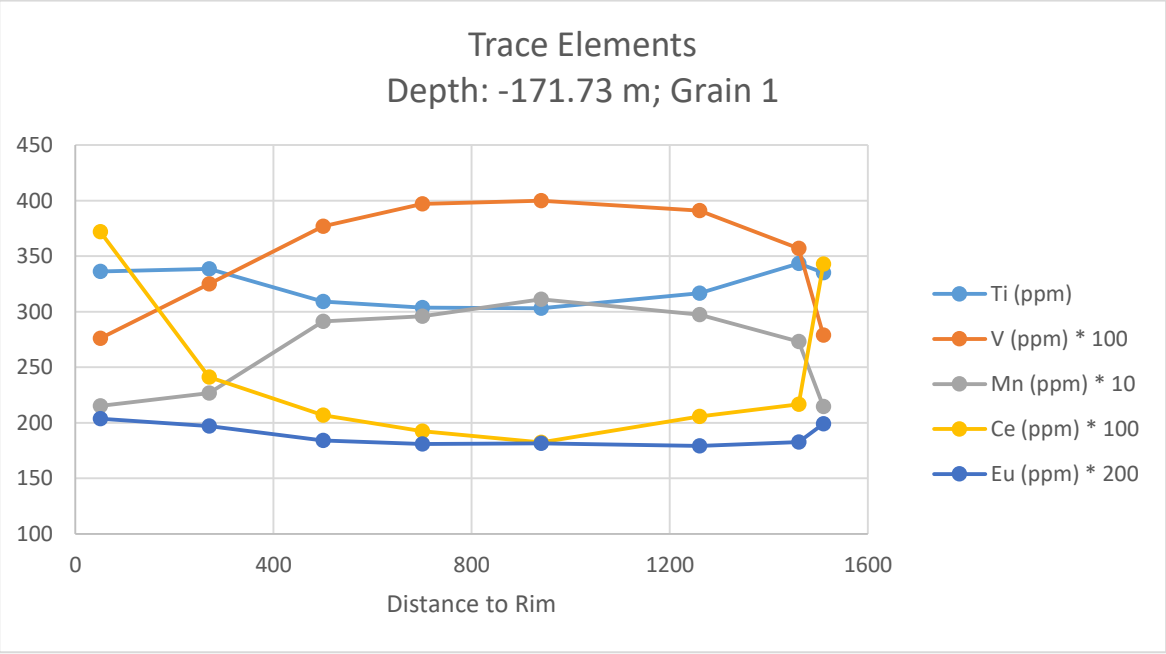

Figure 50: Spot traverse analysis, Depth: -171.73 m; Grain 1

The plot (Figure 50) shows that the Ti concentration is lower in the core of the grain than in the rims. The plot also shows that the core of the grain is enriched in V and Mn. Furthermore, the plot shows that the rims of the grain are particularly enriched in Ce relative to the core. The plot shows a slight increase in the Eu concentration towards the rims of the grain. The An percentage was not determined for this grain.

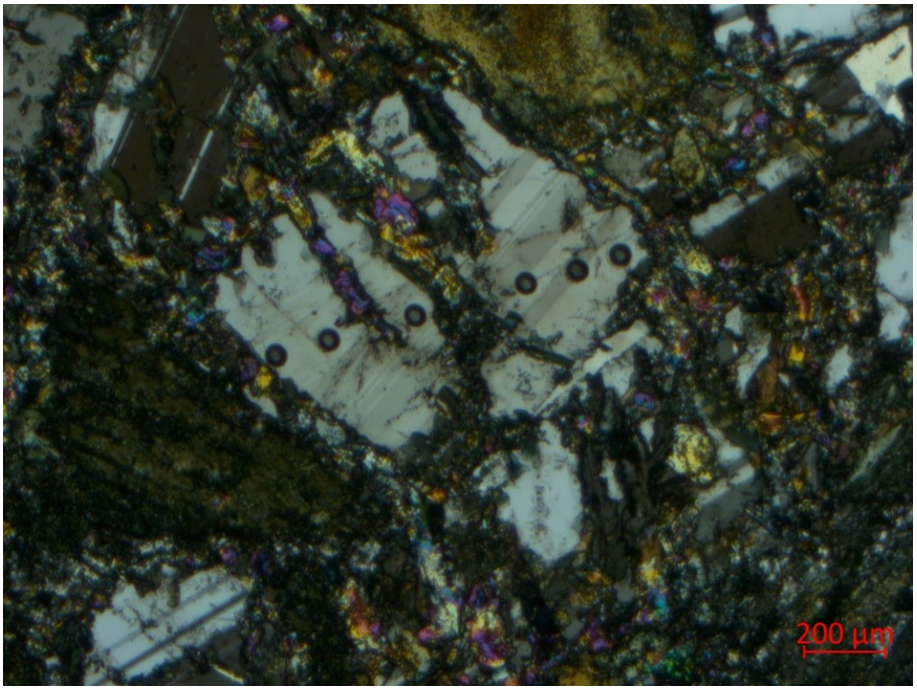

Figure 51: Thin Section 180210 Grain 3

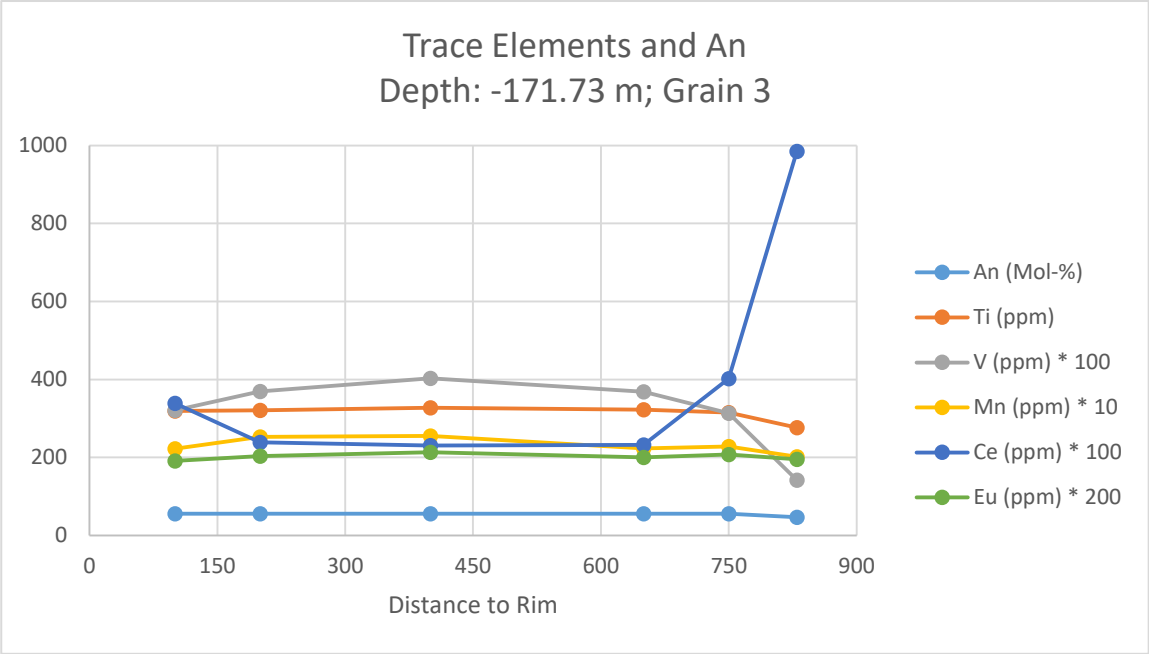

Figure 52: Spot traverse analysis, Depth: -171.73 m; Grain 3

The plot (Figure 52) shows general consistency in the Ti, Mn, and Eu concentrations. The plot also shows thatthe core of the grain is enriched in V. Furthermore, the plot shows that the rims of the grain areenriched in Ce relative to the core. The plot shows consistency in the An percentage along thetraverse of the grain.

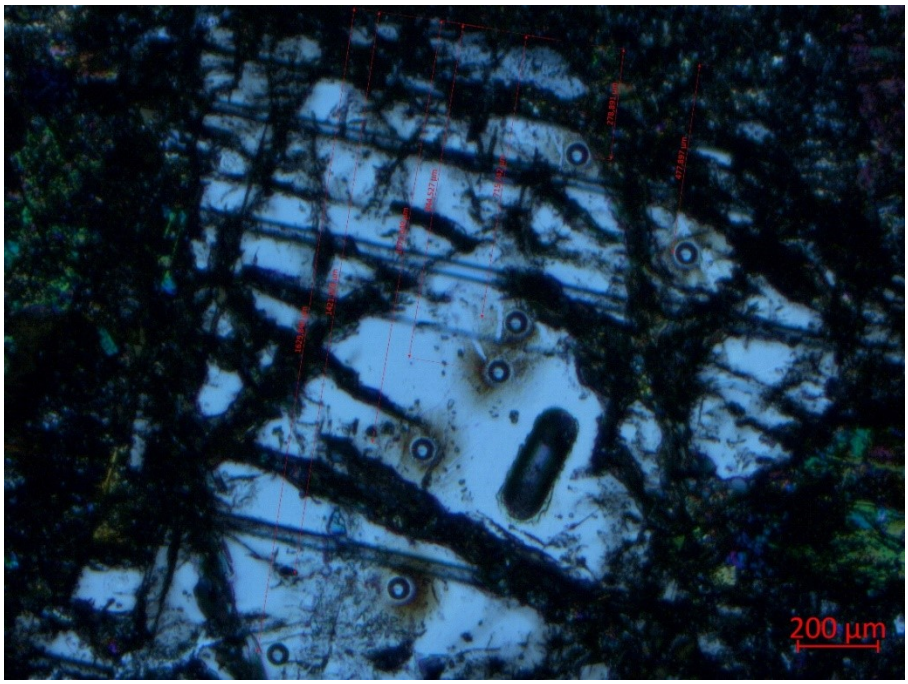

Figure 53: Thin Section 180211 Grain 1

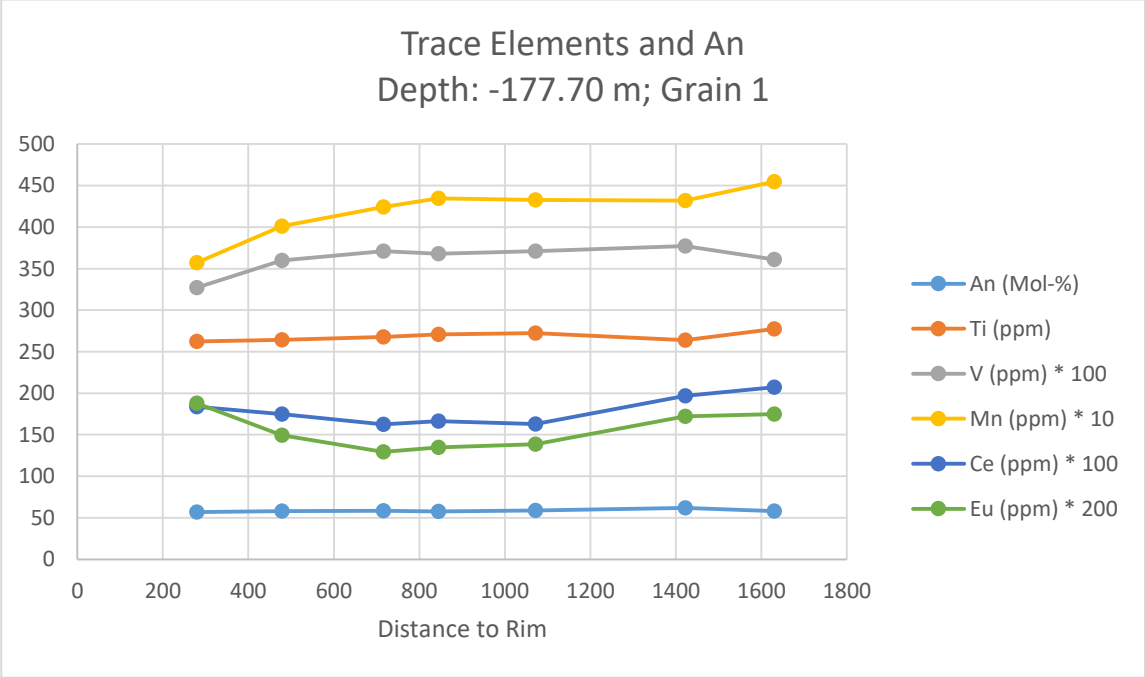

Figure 54: Spot traverse analysis, Depth: -177.70 m; Grain 1

The plot (Figure 54) shows consistency in the Ti concentration. The plot also indicates that the core of the grain is enriched in V and Mn, while the rims of the grain are enriched in Ce and Eu relative to the core. The plot shows consistency in the An percentage.

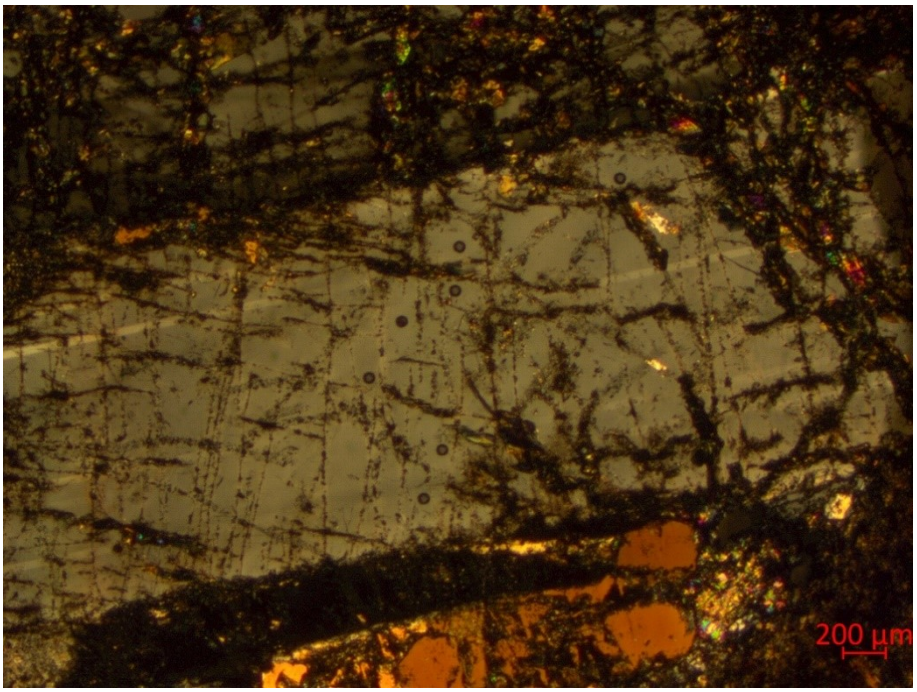

Figure 55: Thin Section 180211 Grain 2

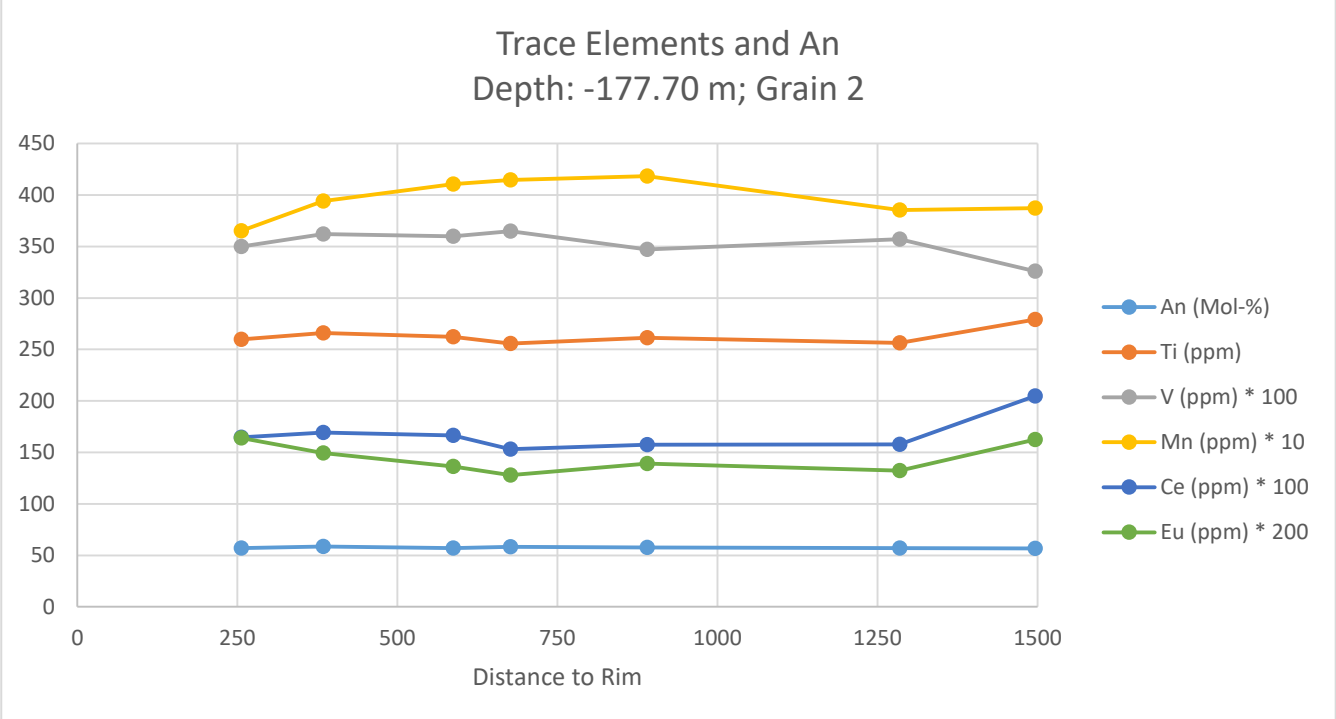

Figure 56: Spot traverse analysis, Depth: -177.70 m; Grain 2

The plot (Figure 56) shows general consistency in the Ti concentration. The plot also shows a slight increase in the V concentration, and a more pronounced increase in the Mn concentration, in the core of the grain. The plot indicates that the rims of the grain are enriched in Ce and Eu relative to the core. The plot shows consistency in the An percentage throughout the traverse of the grain.

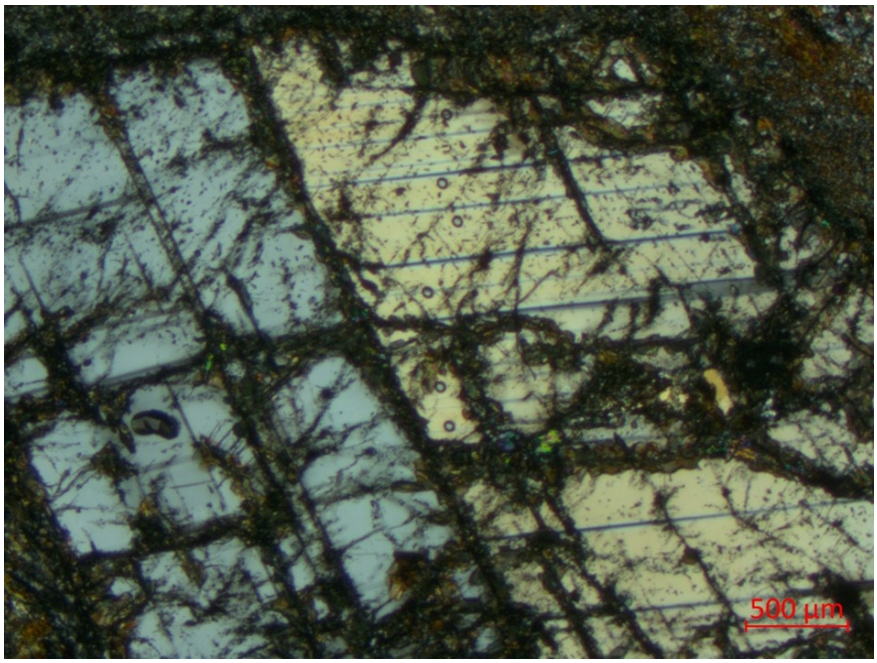

Figure 57: Thin Section 180211 Grain 4

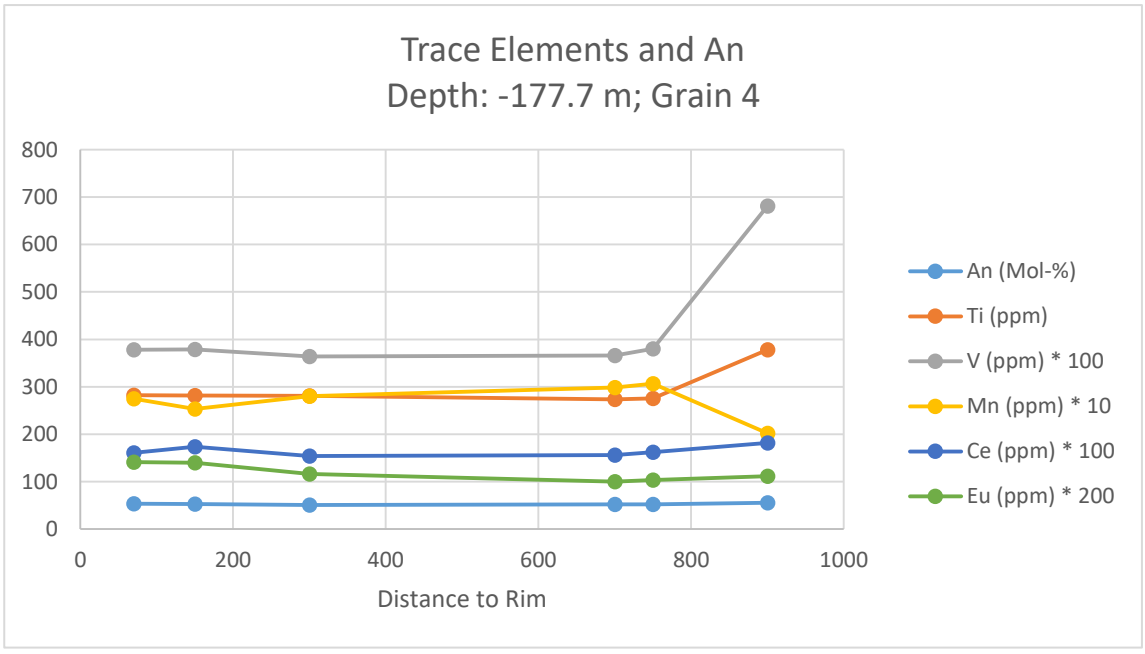

Figure 58: Spot traverse analysis, Depth: -177.70; Grain 4

The plot (Figure 58) shows that one rim of the grain is enriched in Ti and V. The plot also indicates that the core of the grain is enriched in Mn relative to the rims, and that the rims are slightly enriched in Ce relative to the core. The plot shows a general degrease in Eu concentration along the traverse of the grain. The plot shows consistency in the An percentage along the traverse of the grain.

10.3 Appendix 3: EPMA Data and Laser Ablation Standards

The results of the EPMA measurements are given in Table 3.

Sample		An	Ab	Or		Sample	An	Ab	Or
	180185, Depth (51.28m), Hanging wall					180185, Depth (51.28m), Hanging wall (continued)			
		57.85	40.29	1.86			57.17	41.39	1.44
		56.36	41.40	2.24		180188, Depth (68.06m), Hanging wall			
		58.75	39.35	1.90			56.24	41.25	2.51
		51.28	48.24	0.48			54.35	44.85	0.81
		56.49	42.84	0.66		180190, Depth (84.73m), Hanging wall			
		54.88	43.36	1.75			53.99	43.74	2.27
		58.74	39.35	1.91			55.01	43.69	1.30
		57.65	40.33	2.03			56.68	41.33	1.99
		48.33	51.24	0.43			54.12	43.84	2.04
		50.16	47.00	2.84			56.34	41.80	1.86
		52.90	46.12	0.98			53.54	44.32	2.14
		54.12	43.36	2.52		180192, Depth (95.74m), Hanging wall			
		57.70	40.21	2.08			51.51	46.83	1.66
		57.46	40.60	1.94			51.16	48.53	0.31
		55.98	41.68	2.34			54.34	43.55	2.11
		58.16	40.26	1.58			52.95	45.01	2.04
		50.06	47.27	2.67			51.20	48.25	0.55
		57.25	41.44	1.31			54.26	43.67	2.07
		55.67	42.24	2.09			53.54	44.47	1.99
		56.17	42.35	1.48			52.86	46.50	0.64
		57.27	40.99	1.74			50.83	47.94	1.23
		50.15	47.11	2.74			54.22	44.94	0.84
		57.76	40.38	1.86			52.90	45.08	2.02

Sample	An	Ab	Or		Sample	An	Ab	Or
180192, Depth (95.74m), Hanging wall (continued)					180200, Depth (135.35m), Middle ore layer			
	53.68	44.26	2.06			52.43	46.60	0.97
	52.53	45.62	1.85			55.38	42.04	2.59
	52.49	46.81	0.70			53.93	43.65	2.42
	52.94	46.52	0.54			54.84	43.09	2.07
	57.36	40.64	2.00			54.88	42.47	2.65
	55.91	41.83	2.25			50.89	46.82	2.29
	52.93	44.93	2.14		180202, Depth (144.40m), Middle ore layer			
	53.28	44.61	2.11			57.20	40.40	2.39
	55.14	42.96	1.90			56.43	41.01	2.56
	53.74	44.09	2.17			57.20	40.33	2.48
	54.91	43.09	2.00			56.62	40.91	2.47
	54.49	43.78	1.73			54.89	42.89	2.22
	56.67	41.29	2.03		180204, Depth (156.18m), Middle ore layer			
	57.54	40.30	2.16			57.17	40.29	2.54
	53.22	44.84	1.94			56.54	42.00	1.46
180193, Depth (106.14m), Disseminated ore layer					180205, Depth (158.90m), Middle ore layer			
	53.01	44.73	2.27			53.87	43.83	2.29
	55.13	42.14	2.73			54.61	43.07	2.32
	56.00	41.59	2.40			53.62	44.07	2.31
	53.30	45.20	1.51			53.32	44.33	2.35
180196, Depth (118.70m), Upper ore layer						51.98	45.60	2.42
	55.03	42.90	2.07			51.82	45.91	2.28
	55.50	42.25	2.25			54.36	43.51	2.12
	54.97	42.81	2.22			49.82	47.32	2.86
	55.51	42.37	2.12			54.02	43.84	2.14
180198, Depth (125.63m), Upper ore layer						52.77	44.84	2.38
	54.48	43.27	2.25			53.28	44.33	2.38
	54.48	43.27	2.25			53.76	43.85	2.40
	56.04	41.60	2.36			53.01	44.76	2.24
	56.04	41.60	2.36			52.86	44.91	2.24
	56.81	40.99	2.20			53.50	44.29	2.21
	56.81	40.99	2.20			53.22	44.33	2.45
	55.44	42.38	2.18			56.04	41.41	2.55
	55.44	42.38	2.18			57.04	40.54	2.42
	54.51	43.30	2.19			52.54	45.02	2.44
	54.51	43.30	2.19			55.57	42.03	2.40
	54.48	43.27	2.25			54.95	43.06	1.99
						55.72	41.90	2.38

Sample	An	Ab	Or		Sample	An	Ab	Or
180206, Depth (160.08m), Lower ore layer					180211, Depth (177.70m), Footwall (continued)			
	58.70	39.49	1.81			58.12	40.80	1.08
	59.23	38.99	1.78			58.41	39.92	1.67
	55.55	42.37	2.08			57.67	40.73	1.60
	58.62	39.42	1.96			58.65	39.84	1.51
	56.70	41.86	1.44			61.73	36.74	1.53
	54.83	43.46	1.71			58.12	40.08	1.80
180210, Depth (171.73m), Footwall						56.81	41.34	1.85
	56.86	41.21	1.94			56.89	41.32	1.80
	59.23	38.64	2.13			57.65	40.79	1.56
	57.07	40.89	2.04			58.41	40.03	1.56
	55.88	42.31	1.81			56.87	42.64	0.49
	55.46	43.41	1.13			58.50	39.80	1.70
	55.17	44.10	0.74			57.08	41.33	1.59
	55.55	42.44	2.01			53.71	44.87	1.42
	55.86	42.37	1.77			58.00	40.36	1.64
	46.54	52.11	1.36			60.37	38.10	1.53
	56.52	41.74	1.73			58.98	39.98	1.04
	55.46	42.79	1.75			59.41	39.29	1.31
	55.29	42.94	1.76			58.37	39.71	1.92
	55.41	44.11	0.48			57.79	40.39	1.81
	56.59	41.69	1.73			56.41	42.26	1.33
	52.77	44.87	2.37			57.07	41.16	1.77
180211, Depth (177.70m), Footwall						57.83	40.89	1.29
	58.93	39.44	1.63			61.06	38.06	0.87
	56.69	41.72	1.59					

The BCR standard measurements for LA-HR-ICP-MS are given in Table 4.

Standard	Ca	Ti	V	Mn	La	Ce	Pr	Nd	Sm	Ba	Sr	Pb	Eu
1	50356.06	13726.01	424.97	1496.66	24.51	51.96	6.79	28.55	6.67	662.35	332.71	10.27	1.98
2	50567.65	14177.02	422.62	1491.72	25.04	52.52	6.75	29.36	6.71	665.91	333.02	10.34	2.01
3	50244.09	13811.11	421.75	1456.83	24.94	51.8	6.81	28.56	6.75	666.24	339.83	10.36	1.98
4	50258.19	13778.11	432.03	1473.69	25.09	53.56	6.86	28.89	6.69	677.52	338.48	10.61	2
5	50135.59	14194.75	440.21	1459.97	25.32	53.48	6.87	29.22	6.9	679.21	345.53	10.55	1.98
6	51661.7	14409.51	435.31	1496.21	26.16	54.68	6.99	30.25	6.71	694.39	352.59	10.78	2.01
7	50494.46	14240.41	430.5	1495.44	25.64	53.9	6.93	29.4	6.75	685.03	343.68	10.66	2
8	50502.65	13971.93	444.51	1482.67	24.81	51.27	6.81	29.02	6.55	659.36	326.48	10.48	1.94
9	50504	14050.43	437.73	1479.7	25.01	52.16	6.85	28.51	6.74	669.27	330.44	10.68	1.98
10	49270.31	13690.7	433.39	1474.92	24.34	51.42	6.67	28.4	6.22	660.75	329.85	10.44	2.02
11	50434.23	14064.39	414.46	1453.15	24.81	51.19	6.62	28.58	6.66	656.68	334.5	9.24	1.89
12	50381.4	13836.6	424.35	1482.54	24.4	51.36	6.58	28	6.55	657.85	332.9	9.95	1.99
13	49359.23	13668.78	420.13	1439.25	24.03	50.71	6.48	27.55	6.29	651.98	326.05	9.61	1.847
14	51254.21	14113.62	425.68	1524	24.96	52.54	6.82	28.24	6.68	674.1	337.56	10.31	2.06
15	49785.55	13897.17	416.6	1466.39	24.73	51.66	6.66	27.83	6.64	664.77	336.56	9.95	1.96
16	50342.8	13727.64	427.2	1454.51	25.17	52.25	6.87	29.17	6.59	676.24	337.43	9.85	2.01
17	52449.06	13889.12	427.94	1512.63	25.7	52.77	6.72	29.1	6.69	684.88	357.15	10.25	2.01
18	52145.59	13816.16	415.63	1516.59	25.44	52.91	6.79	28.96	7.04	678.46	356.42	10.34	2.06
19	49276.99	13754.02	415.23	1495.38	24.24	50.99	6.56	27.91	6.26	654.41	341.72	9.94	1.81
20	50024.97	13808.47	406.97	1480.52	24.54	51.72	6.68	28.38	6.45	661.36	339.24	9.95	1.96
21	50262.32	14224.73	432.5	1499.31	24.9	52.21	6.88	29.21	6.57	669.92	343.27	9.93	1.96
22	51436.86	14213.99	415.29	1494.46	25.53	53.16	6.92	29.78	6.67	673.18	341.8	10.09	2.05
23	51088.98	14244.23	418.97	1493.85	25.17	53.12	6.93	30.06	6.82	671.29	343.26	10.27	1.996
24	50637.18	13949.54	424.59	1492.2	25.13	53.4	6.84	29.18	6.68	671.18	332.47	10.49	2.068
25	50764.75	14034.2	446.96	1473.64	24.8	51.94	6.74	29.09	6.63	660.91	332.72	10.48	1.975
26	52037.34	14261.44	450.5	1520.17	25.32	52.98	6.93	29.52	6.66	672.48	347.38	10.98	2.02
27	50460.95	14196.75	474.87	1482.25	24.36	51.18	6.64	28.2	6.48	651.47	324.56	10.56	1.952
28	50814.24	14139.75	490.69	1508.84	24.78	52.12	6.68	28.61	6.54	660.39	328.09	10.67	1.911

Standard	Ca	Ti	V	Mn	La	Ce	Pr	Nd	Sm	Ba	Sr	Pb	Eu
29	50557.7	13954.43	425.62	1481.34	25.03	52.64	6.74	28.78	6.63	667.32	341.23	10.22	1.912
30	50951.79	14130.54	415.71	1504.77	25.51	53.44	6.88	29.29	6.84	679.35	339.92	10.16	1.976
31	51840	14335.24	420.79	1494	26.1	53.75	7.02	30.15	6.99	684.4	337.22	10.12	2.06
32	50242.88	14053.4	411.14	1460.06	24.64	52.1	6.74	28.67	6.65	665.21	333.54	9.99	1.92
33	51291.27	14323.83	431.52	1511.33	25.27	53.3	6.78	29.2	7	670.33	339.8	10.45	2.02
34	51747.58	14065.7	424.81	1517.16	25.54	53.99	7.08	29.58	6.53	690.63	347.43	10.48	2.11
35	50955.39	14116.32	437.49	1530.58	24.99	53.14	6.82	28.92	6.9	682.37	339.97	11.36	1.97
36	51767.45	14355.67	429.13	1531.57	25.45	53.3	6.98	29.08	6.84	683.15	357.79	10.55	2.03
37	51751.36	14330.08	414.47	1477.35	25.77	52.72	7.01	29.61	6.61	674.52	354.08	10.69	2.1
38	50763.86	13917.64	411.19	1481.73	25.48	52.74	6.88	29.33	6.65	676.42	349.8	10.49	2.028
39	50774.74	14065.87	417.11	1471.21	25.24	52.29	6.82	29.3	6.83	672.52	347.75	10.55	1.936
40	51736.14	13963.36	404.99	1473.75	25.68	52.46	6.87	29.4	6.65	672.18	352.48	10.67	2.01
41	51454.89	13760.35	408.67	1520.29	25.36	52.96	6.92	29.41	6.8	679.43	352.75	10.84	2.01
42	49078.34	13645.34	396.42	1462.17	24.2	50.72	6.53	27.98	6.59	647.23	333.89	10.11	2.01
43	49927.34	13712.41	401.28	1467.85	24.74	52.04	6.73	28.16	6.66	666.18	343.71	10.32	1.99
44	51722.71	13684.84	401.71	1508.59	24.93	52.01	6.86	28.2	6.58	668.66	350.18	10.59	2.01
45	51448.89	14174.42	403.38	1502.58	24.95	52.26	6.84	28.95	6.69	665.63	349.28	10.6	1.95
46	50356.06	13726.01	424.97	1496.66	24.51	51.96	6.79	28.55	6.67	662.35	332.71	10.27	1.98
47	50567.65	14177.02	422.62	1491.72	25.04	52.52	6.75	29.36	6.71	665.91	333.02	10.34	2.01
48	50244.09	13811.11	421.75	1456.83	24.94	51.8	6.81	28.56	6.75	666.24	339.83	10.36	1.98
49	50258.19	13778.11	432.03	1473.69	25.09	53.56	6.86	28.89	6.69	677.52	338.48	10.61	2
50	50135.59	14194.75	440.21	1459.97	25.32	53.48	6.87	29.22	6.9	679.21	345.53	10.55	1.98
51	51661.7	14409.51	435.31	1496.21	26.16	54.68	6.99	30.25	6.71	694.39	352.59	10.78	2.01
52	50494.46	14240.41	430.5	1495.44	25.64	53.9	6.93	29.4	6.75	685.03	343.68	10.66	2
53	50502.65	13971.93	444.51	1482.67	24.81	51.27	6.81	29.02	6.55	659.36	326.48	10.48	1.94
54	50504	14050.43	437.73	1479.7	25.01	52.16	6.85	28.51	6.74	669.27	330.44	10.68	1.98
55	49270.31	13690.7	433.39	1474.92	24.34	51.42	6.67	28.4	6.22	660.75	329.85	10.44	2.02
56	50434.23	14064.39	414.46	1453.15	24.81	51.19	6.62	28.58	6.66	656.68	334.5	9.24	1.89
57	50381.4	13836.6	424.35	1482.54	24.4	51.36	6.58	28	6.55	657.85	332.9	9.95	1.99
58	49359.23	13668.78	420.13	1439.25	24.03	50.71	6.48	27.55	6.29	651.98	326.05	9.61	1.847

Standard	Ca	Ti	V	Mn	La	Ce	Pr	Nd	Sm	Ba	Sr	Pb	Eu
59	51254.21	14113.62	425.68	1524	24.96	52.54	6.82	28.24	6.68	674.1	337.56	10.31	2.06
60	49785.55	13897.17	416.6	1466.39	24.73	51.66	6.66	27.83	6.64	664.77	336.56	9.95	1.96
61	50342.8	13727.64	427.2	1454.51	25.17	52.25	6.87	29.17	6.59	676.24	337.43	9.85	2.01
62	52449.06	13889.12	427.94	1512.63	25.7	52.77	6.72	29.1	6.69	684.88	357.15	10.25	2.01
63	52145.59	13816.16	415.63	1516.59	25.44	52.91	6.79	28.96	7.04	678.46	356.42	10.34	2.06
64	49276.99	13754.02	415.23	1495.38	24.24	50.99	6.56	27.91	6.26	654.41	341.72	9.94	1.81
65	50024.97	13808.47	406.97	1480.52	24.54	51.72	6.68	28.38	6.45	661.36	339.24	9.95	1.96
66	50262.32	14224.73	432.5	1499.31	24.9	52.21	6.88	29.21	6.57	669.92	343.27	9.93	1.96
67	51436.86	14213.99	415.29	1494.46	25.53	53.16	6.92	29.78	6.67	673.18	341.8	10.09	2.05
68	51088.98	14244.23	418.97	1493.85	25.17	53.12	6.93	30.06	6.82	671.29	343.26	10.27	1.996
69	50637.18	13949.54	424.59	1492.2	25.13	53.4	6.84	29.18	6.68	671.18	332.47	10.49	2.068
70	50764.75	14034.2	446.96	1473.64	24.8	51.94	6.74	29.09	6.63	660.91	332.72	10.48	1.975
71	52037.34	14261.44	450.5	1520.17	25.32	52.98	6.93	29.52	6.66	672.48	347.38	10.98	2.02
72	50460.95	14196.75	474.87	1482.25	24.36	51.18	6.64	28.2	6.48	651.47	324.56	10.56	1.952
73	50814.24	14139.75	490.69	1508.84	24.78	52.12	6.68	28.61	6.54	660.39	328.09	10.67	1.911
74	50557.7	13954.43	425.62	1481.34	25.03	52.64	6.74	28.78	6.63	667.32	341.23	10.22	1.912
75	50951.79	14130.54	415.71	1504.77	25.51	53.44	6.88	29.29	6.84	679.35	339.92	10.16	1.976
76	51840	14335.24	420.79	1494	26.1	53.75	7.02	30.15	6.99	684.4	337.22	10.12	2.06
77	50242.88	14053.4	411.14	1460.06	24.64	52.1	6.74	28.67	6.65	665.21	333.54	9.99	1.92
78	51291.27	14323.83	431.52	1511.33	25.27	53.3	6.78	29.2	7	670.33	339.8	10.45	2.02
79	51747.58	14065.7	424.81	1517.16	25.54	53.99	7.08	29.58	6.53	690.63	347.43	10.48	2.11
80	50955.39	14116.32	437.49	1530.58	24.99	53.14	6.82	28.92	6.9	682.37	339.97	11.36	1.97
81	51767.45	14355.67	429.13	1531.57	25.45	53.3	6.98	29.08	6.84	683.15	357.79	10.55	2.03
82	51751.36	14330.08	414.47	1477.35	25.77	52.72	7.01	29.61	6.61	674.52	354.08	10.69	2.1
83	50763.86	13917.64	411.19	1481.73	25.48	52.74	6.88	29.33	6.65	676.42	349.8	10.49	2.028
84	50774.74	14065.87	417.11	1471.21	25.24	52.29	6.82	29.3	6.83	672.52	347.75	10.55	1.936
85	51736.14	13963.36	404.99	1473.75	25.68	52.46	6.87	29.4	6.65	672.18	352.48	10.67	2.01
86	51454.89	13760.35	408.67	1520.29	25.36	52.96	6.92	29.41	6.8	679.43	352.75	10.84	2.01

Standard	Ca	Ti	V	Mn	La	Ce	Pr	Nd	Sm	Ba	Sr	Pb	Eu
87	49078.34	13645.34	396.42	1462.17	24.2	50.72	6.53	27.98	6.59	647.23	333.89	10.11	2.01
88	49927.34	13712.41	401.28	1467.85	24.74	52.04	6.73	28.16	6.66	666.18	343.71	10.32	1.99
89	51722.71	13684.84	401.71	1508.59	24.93	52.01	6.86	28.2	6.58	668.66	350.18	10.59	2.01
90	51448.89	14174.42	403.38	1502.58	24.95	52.26	6.84	28.95	6.69	665.63	349.28	10.6	1.95

The BHVO standard measurements for LA-MC-ICP-MS are given in Table 5.

	Sr signal (V)	**Rb signal (V)**	**$^{84}Sr/^{86}Sr$**	**1σ**	**$^{87}Sr/^{86}Sr$**	**$^{87}Sr/^{86}Sr$**	**1σ**	**$^{87}Rb/^{86}Sr$**
Standard					**recalculated**	**recalculated**	**recalculated**	
110m-1	0.28741	0.00719	0.05569	0.00006	0.703377	0.703505	0.00008	0.0691
110m-2	0.28511	0.00713	0.05605	0.00006	0.703057	0.703185	0.00007	0.0682
110m-4	0.22990	0.00595	0.05589	0.00007	0.703445	0.703573	0.00009	0.0702
110m-5	0.23198	0.00613	0.05629	0.00006	0.703409	0.703537	0.00009	0.0721
110m-6	0.28218	0.00707	0.05573	0.00006	0.703464	0.703592	0.00007	0.0690
110m-7	0.25190	0.00633	0.05468	0.00006	0.703667	0.703795	0.00010	0.0694
110m-5	0.27097	0.00673	0.05638	0.00006	0.703636	0.703764	0.000090	0.0686
110m-6	0.22850	0.00596	0.05742	0.00008	0.703200	0.703328	0.000087	0.0713
150m-1	0.39811	0.01054	0.05550	0.00004	0.703309	0.703437	0.000053	0.0731
150m-2	0.41764	0.01125	0.05658	0.00004	0.703483	0.703611	0.000052	0.0741
150m-3	0.42328	0.01127	0.05615	0.00004	0.702887	0.703015	0.000062	0.0732
150m-4	0.33393	0.00855	0.05673	0.00005	0.703080	0.703208	0.000054	0.0708

The plagioclase standard measurements for LA-MC-ICP-MS are given in Table 6:

Table 6: Plagioclase standard measurements for LA-MC-ICP-MS

	Sr (V)	Rb (V)	$^{84}Sr/^{86}Sr$	1σ	$^{87}Sr/^{86}Sr$	$^{87}Sr/^{86}Sr$	1σ	$^{87}Rb/^{86}Sr$
Standard						**recalculated**		
Plg Std-1-1	1.8	0.00136	0.05630	0.00001	0.702961	0.703089	0.00002	0.0020
Plg Std-2-1	1.7	0.00132	0.05625	0.00001	0.702873	0.703001	0.00002	0.0020
Plg Std-3-1	1.8	0.00133	0.05637	0.00001	0.702964	0.703092	0.00002	0.0020
Plg Std-4-1	1.7	0.00132	0.05636	0.00001	0.702956	0.703084	0.00002	0.0020
Plg Std-5-1	1.6	0.00121	0.05629	0.00001	0.702900	0.703027	0.00002	0.0021
Plg Std-6-1	1.5	0.00120	0.05640	0.00001	0.702951	0.703079	0.00002	0.0021
Plg Std-7-1	1.5	0.00112	0.05641	0.00001	0.702937	0.703065	0.00002	0.0020
Plg Std-8-1	1.8	0.00147	0.05624	0.00001	0.702886	0.703014	0.00002	0.0021
Plg Std-9-1	1.7	0.00133	0.05628	0.00001	0.703021	0.703149	0.00002	0.0021
Plg Std-10-1	1.5	0.00118	0.05624	0.00001	0.702865	0.702993	0.00002	0.0022
Plg Std-11-1	1.6	0.00123	0.05612	0.00001	0.702906	0.703034	0.00002	0.0021
Plg Std-1-2	1.9	0.00152	0.05627	0.00001	0.703074	0.703202	0.000017	0.0021
Plg Std-2-2	1.9	0.00145	0.05586	0.00001	0.702959	0.703087	0.000019	0.0021
Plg Std-3-2	1.7	0.00134	0.05641	0.00001	0.702861	0.702989	0.000018	0.0022
Plg Std-4-2	1.7	0.00139	0.05641	0.00001	0.702945	0.703073	0.000018	0.0022
Plg Std-5-2	1.6	0.00124	0.05649	0.00001	0.702862	0.702990	0.000020	0.0021
Plg Std-6-2	1.5	0.00123	0.05640	0.00001	0.702868	0.702996	0.000020	0.0022
Plg Std-7-2	2.6	0.00213	0.05644	0.00001	0.702956	0.703084	0.000012	0.0022
Plg Std-8-2	2.5	0.00211	0.05634	0.00001	0.702922	0.703050	0.000013	0.0024
Plg Std-9-2	2.4	0.00204	0.05635	0.00001	0.703062	0.703190	0.000013	0.0023
Plg Std-10-2	2.2	0.00184	0.05652	0.00001	0.702960	0.703088	0.000014	0.0023
Plg Std-11-2	2.0	0.00163	0.05645	0.00001	0.702921	0.703049	0.000015	0.0022
Plg Std-12-2	1.9	0.00162	0.05652	0.00001	0.702876	0.703004	0.000015	0.0023